博士論文

光可逆的タンパク質ラベル化技術の開発

Development of a photo-reversible protein labeling system

間下　貴斗

令和３年

CONTENTS

CHAPTER 1

General Introduction

1-1. Artificial regulation of protein dynamics in live cells

Cellular events are spatiotemporally regulated by the dynamics of various biomolecules, such as protein-protein interaction or protein translocation. For example, most posttranslational modifications such as phosphorylation, methylation, and acetylation promote the proximity of molecules to play deterministic roles in cellular processes. In the MAPK cascade, a receptor kinase activates Ras, and Raf translocates to the plasma membrane to form a dimer (Figure 1-1).[1] The recruitment of Raf to the plasma membrane and its dimerization are important for the activation of Raf. It has also been reported that the artificial anchoring of Raf to the plasma membrane can trigger signal transduction.[2] Thus, protein function in the cell is strictly controlled by protein localization and dimerization.

Many scientists studying a biological process have gained access to powerful approaches for artificial control over protein functions. One approach, inducible dimerization, utilizes proteins that can be triggered to associate, bringing attached target proteins into proximity. Inducible dimerization systems were initially implemented with chemical ligands.[3-5] With chemically induced dimerization (CID) systems, two identical proteins (homodimerization) or two different proteins (heterodimerization) are induced to associate or dimerize upon addition of a chemical ligand.[6-8] Furthermore, photo-activatable or photo-cleavable CID systems have been reported and attracted attention as a new chemical tool for the precise regulation of protein dynamics.[9-12] Using these photo-responsive CID systems as a chemical-biology tool, the molecular mechanisms of various cellular events have been revealed.[13, 14]

The other inducible dimerization systems employ photo-responsive proteins whose conformations are changed upon illumination.[15-18] This approach termed optogenetics has allowed reversible induction of protein association or dimerization dependent on light. Several biological questions that have been difficult or impossible to be addressed with other tools have been solved with optogenetic tools that dynamically manipulate protein localization with high precision in space and time.[19-21]

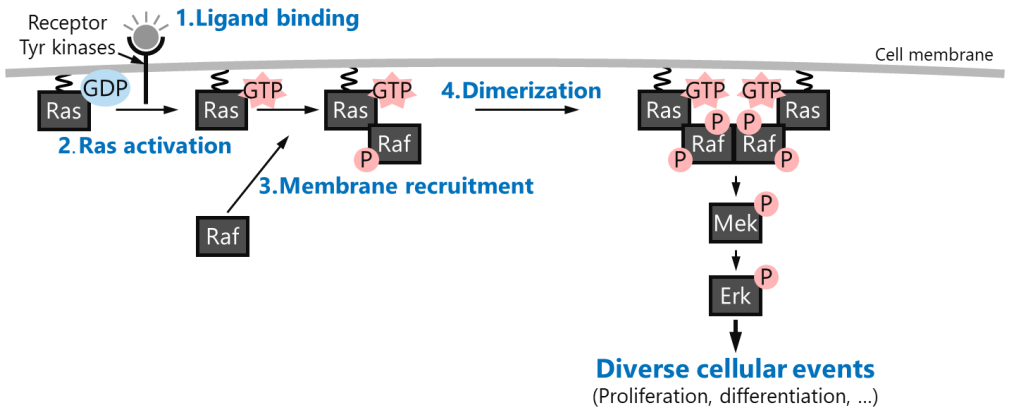

Figure 1-1. Schematic illustration of Ras/Erk signal pathway.

1-2. Optogenetic regulation of protein localization

There have been reports of studies aimed at elucidating signaling pathways by optically regulating the subcellular localization of proteins. A. Lim et al. reported an optogenetic control of Ras/ERk signal pathway (Figure 1-2).[20] In their study, a light-responsive protein, PhyB-PIF, is used to control the localization of SOS, which is responsible for the activation of Ras. When SOS is localized by red light, Ras is activated, and the signal is transmitted downstream. It has been reported that controlling the localization of SOS results in different cellular responses. In other words, it has been reported that activation for 4 minutes or less does not trigger signaling, while activation for 10 minutes or several hours triggers signaling. It has also been reported that the transduction pathway differs depending on the duration of activation. Thus, the use of light-responsive proteins will enable to elucidate detailed signaling pathways.

Representatives of optogenetic tool kits are summarized in Table 1-1. CRY2/CIBN,[17] iLID,[16] Magnets,[15] and eMagnets[22] employ flavin derivatives as a cofactor. They dimerize upon blue light and diffuse under dark conditions. Therefore, reversible light control is possible, but there are still some issues to be solved, such as the need for continuous exposure to blue light to maintain dimerization. PhyB-PIF adopts phycocyanobilin as a cofactor required to be externally added.[18] This system allows both controls of dimerization and diffusion by light illumination. However, there is a problem that the simultaneous use of fluorescent proteins is limited by the wide absorption band derived from phycocyanobilin.

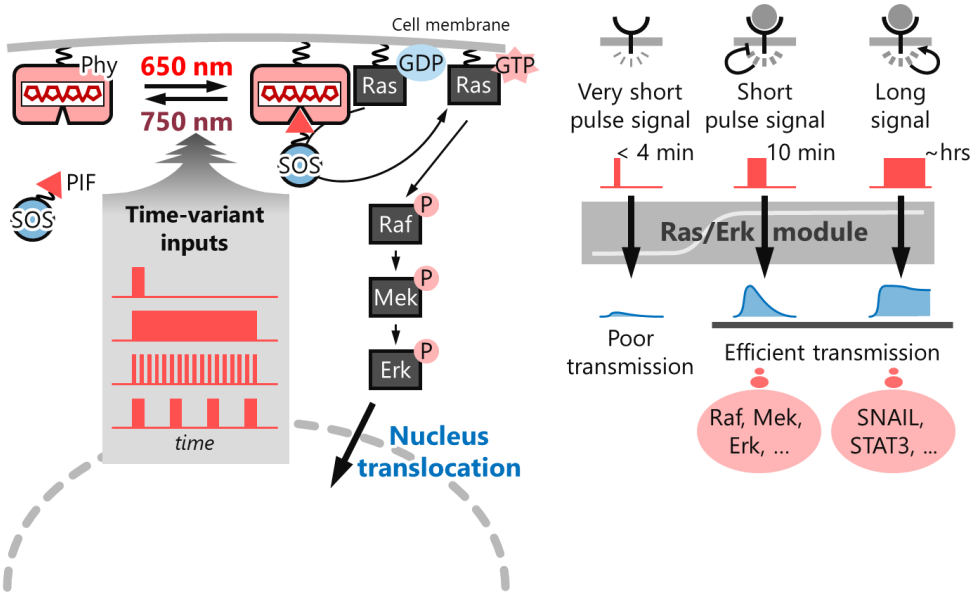

Figure 1-2. Optogenetic control of Ras/Erk signal pathway.

Table 1-1. Optogenetic tools for localization control

Name		CRY2/ CIBN	iLID	Magnet	eMags	PhyB/ PIF
Size (kDa)		55/19	17	34/51	17/17	99/11
Cofactor		FAD	FMN	FAD	FAD	Phycocyanobilin
Wavelength (nm) (ON/OFF)		488/Dark	488/Dark	488/Dark	488/Dark	650/750
ON/OFF rate	$t_{1/2,on}$ (s)	3.7 ± 0.9	1.2 ± 0.3	1.4 ± 0.1	3.6 ± 0.3	1.3 ± 0.5
	$t_{1/2,off}$ (s)	290 ± 30	4 ± 1	15 ±3	23.1 ± 0.6	4 ± 1
Note		Spread of activated protein		Preincubation at 28 ºC		Addition of phycocyanobilin Limitation of fluorescent protein

1-3. Protein labeling system

Another approach for the induction of protein dimerization is the use of protein labeling systems, which utilizes the specific binding between a tag protein and a labeling ligand.[6, 7] Using the protein labeling system, target proteins can be genetically fused with a tag protein and subsequently labeled with a ligand-modified functional molecule to be provided with various functions (Figure 1-3).[23] Several CID systems inherently employ protein labeling systems such as eDHFR-TMP,[24] HaloTag,[25] and SNAP-tag[26] for specific binding between a protein and a chemical ligand.

Over a couple of decades, photo-responsive CID systems have been reported and attracted attention as a new chemical tool for the precise regulation of protein dynamics.[27] Among several photo-responsive CID systems, non-diffusible systems through a covalent bond to one protein are superior to diffusible ones because of high spatial precision.[28-31] In these non-diffusible systems, one tag ligand forms a covalent bond with the corresponding tag protein to suppress diffusion of a chemical dimerizer, and the photolabile group is attached on the other ligand or between ligands (Figure 1-4). Furthermore, using two different photolabile groups in a chemical dimerizer, both-directional control of protein localization and diffusion was also achieved for one-time use.[32, 33] Using these photo-responsive CID systems as a chemical-biology tool, the molecular mechanisms of various cellular events have been revealed.[13, 14] Although photo-responsive CID systems have provided exquisite control in time and space, they yet cannot be switched on and off repetitively upon light, unlike optogenetic tools.

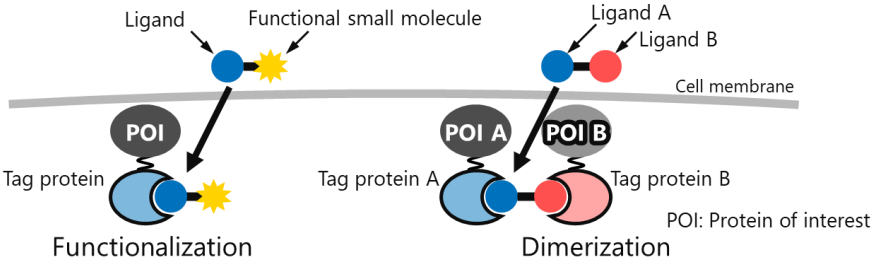

Figure 1-3. Schematic illustration of protein labeling system.

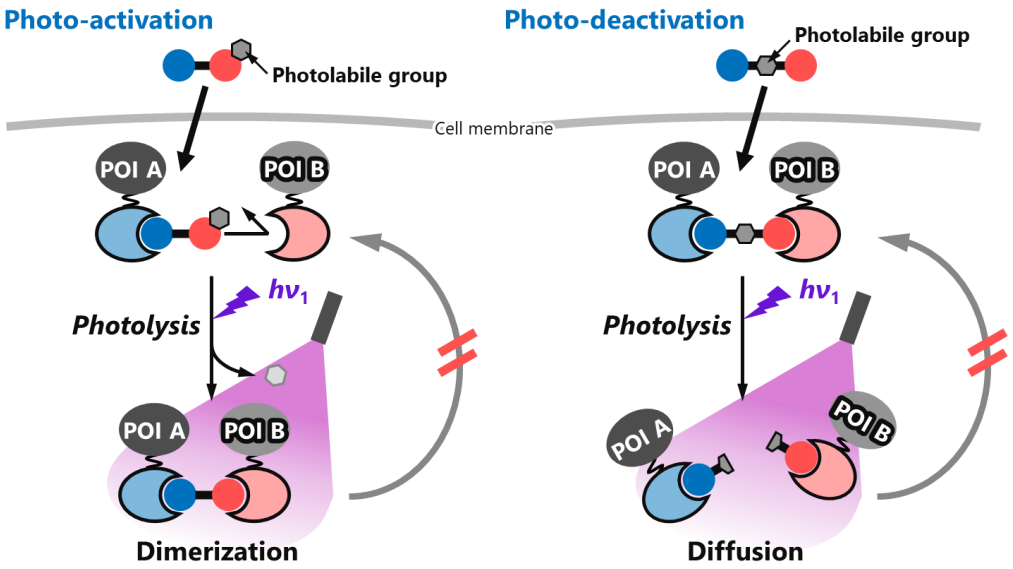

Figure 1-4. Schematic illustration of photo-responsive CID system based on photocleavage of the photolabile group.

1-4. Outline of the research

An ideal system for artificial regulation of protein dynamics features high specificity and binding affinity, bioorthogonality, reversibility, simple operation, and high spatiotemporal resolution. CID systems are facile to operate by adding compounds and are tunable by controlling the dosage of compounds. On the other hand, light-induced dimerization systems confer a spatiotemporal resolution that is unmatched by chemical approaches, and photo-activation can be performed in a spatially defined manner at a subcellular level. In terms of these points, photo-responsive CID systems are likely to be an ideal tool; however, it is difficult to apply photo-responsive CID systems for repetitive control of biomolecular functions because of their irreversibility of photolysis. To overcome this limitation, the author has addressed the development of a photo-reversible protein labeling system to allow reversible photo-regulation of protein dimerization.

In chapter 2, the author designed and developed an efficient photochromic ligand, azoMTX, for *Escherichia coli* dihydrofolate reductase (eDHFR) by replacing some atoms of the original ligand, methotrexate, to obtain the photoisomerization property. This fine molecular design allowed the quick structural conversion between the active 'bent' *Z*-isomer and the inactive 'extended' *E*-isomer of azoMTX, and this property afforded quantitative control of the enzyme activity, depending on the wavelength of irradiated light. The real-time photo-reversible control of enzyme activity was also achieved.

In chapter 3, the author has implemented a novel photochromic CID system capable of repetitive switching on and off upon light. AzoMTX derivative was employed for a photo-responsive group, and photoisomerization of the azoMTX altered the affinity to the corresponding protein. Repetition of dimerization was evaluated in cells by induction of protein translocation to various organelles, and quick and reversible control of protein translocation was feasible. Finally, the photochromic CID

system was applied to optical regulation of autophagy-mediated degradation of mitochondria.

In chapters 4 and 5, the author has improved the photochromic CID system implemented in chapter 3. One room for improvement found in chapter 3 is the small difference between the dissociation constants of the *E*/*Z* isomers with eDHFR. That is likely due to removal or conversion to an amide of carboxylate groups in the parent molecule, azoMTX, while this suggests that proper derivatization of the photochromic ligand may enhance the affinity difference between the isomers. In addition to the derivatization of photochromic ligand, the author has addressed an alternative approach by introducing a mutation into the substrate-binding site of eDHFR to establish a system with better *E*/*Z* selectivity. In chapter 4, the author addressed mutation into eDHFR to enhance the affinity difference between the two isomers. Some mutant enhanced the *E*/*Z* selectivity on the dissociation constant.

The other room for improvement is the absorption spectral overlap between azoMTX derivatives and a commonly used red fluorescent protein. In chapter 5, the author has addressed the derivatization of azobenzene analog to resolve the spectral overlap. Incorporation of a five-membered aromatic heterocycle into an azobenzene analog shifted absorption for *Z*-to-*E* photoisomerization. Moreover, the derivatized ligand was also associated with and dissociated from eDHFR repetitively by alternating irradiation with two wavelengths of light.

Overall, the author has achieved photo-repetitive regulation of protein labeling based on photochromism and applied it to a photo-reversible CID system. The photo-reversible CID allowed a sophisticated spatiotemporal regulation of protein dynamics in a live cell. The author envisions that a photochromism-based strategy for optical control will expand the toolkit for precise control of intracellular protein dynamics and contribute to the study of diverse cellular processes.

1-5. References (chapter 1)

1. Lavoie, H.; Therrien, M., Regulation of RAF protein kinases in ERK signalling. *Nat. Rev. Mol. Cell Biol.* **2015,** *16* (5), 281-298.

2. Stokoe, D.; Macdonald, S. G.; Cadwallader, K.; Symons, M.; Hancock, J. F., Activation of Raf as a Result of Recruitment to the Plasma Membrane. *Science* **1994,** *264* (5164), 1463–1467.

3. Spencer, D.; Wandless, T.; Schreiber, S.; Crabtree, G., Controlling signal transduction with synthetic ligands. *Science* **1993,** *262* (5136), 1019–1024.

4. Belshaw, P. J.; Ho, S. N.; Crabtree, G. R.; Schreiber, S. L., Controlling protein association and subcellular localization with a synthetic ligand that induces heterodimerization of proteins. *Proc. Natl. Acad. Sci. USA* **1996,** *93* (10), 4604–4607.

5. Bayle, J. H.; Grimley, J. S.; Stankunas, K.; Gestwicki, J. E.; Wandless, T. J.; Crabtree, G. R., Rapamycin Analogs with Differential Binding Specificity Permit Orthogonal Control of Protein Activity. *Chem. Biol.* **2006,** *13* (1), 99–107.

6. Czlapinski, J. L.; Schelle, M. W.; Miller, L. W.; Laughlin, S. T.; Kohler, J. J.; Cornish, V. W.; Bertozzi, C. R., Conditional Glycosylation in Eukaryotic Cells Using a Biocompatible Chemical Inducer of Dimerization. *J. Am. Chem. Soc.* **2008,** *130* (40), 13186–13187.

7. Lin, H.; Abida, W. M.; Sauer, R. T.; Cornish, V. W., Dexamethasone−Methotrexate: An Efficient Chemical Inducer of Protein Dimerization In Vivo. *J. Am. Chem. Soc.* **2000,** *122* (17), 4247–4248.

8. Liu, P.; Calderon, A.; Konstantinidis, G.; Hou, J.; Voss, S.; Chen, X.; Li, F.; Banerjee, S.; Hoffmann, J. E.; Theiss, C.; Dehmelt, L.; Wu, Y. W., A bioorthogonal small-molecule-switch system for controlling protein function in live cells. *Angew. Chem. Int. Ed.* **2014,** *53* (38), 10049–55.

9. Karginov, A. V.; Zou, Y.; Shirvanyants, D.; Kota, P.; Dokholyan, N. V.; Young, D. D.; Hahn, K. M.; Deiters, A., Light Regulation of Protein Dimerization and Kinase Activity in Living Cells Using Photocaged Rapamycin and Engineered FKBP. *J. Am. Chem. Soc.* **2011,** *133* (3), 420–423.

10. Miyamoto, T.; DeRose, R.; Suarez, A.; Ueno, T.; Chen, M.; Sun, T.-p.; Wolfgang, M. J.; Mukherjee, C.; Meyers, D. J.; Inoue, T., Rapid and orthogonal logic gating with a gibberellin-induced dimerization system. *Nat. Chem. Biol.* **2012,** *8* (5), 465–470.

11. Umeda, N.; Ueno, T.; Pohlmeyer, C.; Nagano, T.; Inoue, T., A Photocleavable Rapamycin Conjugate for Spatiotemporal Control of Small GTPase Activity. *J. Am. Chem. Soc.* **2011,** *133* (1), 12–14.

12. Brown, K. A.; Zou, Y.; Shirvanyants, D.; Zhang, J.; Samanta, S.; Mantravadi, P. K.; Dokholyan, N. V.; Deiters, A., Light-cleavable rapamycin dimer as an optical trigger for protein dimerization. *Chem. Commun.* **2015,** *51* (26), 5702–5705.

13. Zhang, H.; Aonbangkhen, C.; Tarasovetc, E. V.; Ballister, E. R.; Chenoweth, D. M.; Lampson, M. A., Optogenetic control of kinetochore function. *Nat. Chem. Biol.* **2017,** *13* (10), 1096–1101.

14. Akera, T.; Chmátal, L.; Trimm, E.; Yang, K.; Aonbangkhen, C.; Chenoweth, D. M.; Janke, C.; Schultz, R. M.; Lampson, M. A., Spindle asymmetry drives non-Mendelian chromosome segregation. *Science* **2017,** *358* (6363), 668–672.

15. Kawano, F.; Suzuki, H.; Furuya, A.; Sato, M., Engineered pairs of distinct photoswitches for

optogenetic control of cellular proteins. *Nat. Commun.* **2015,** *6* (1), 6256.
16. Guntas, G.; Hallett, R. A.; Zimmerman, S. P.; Williams, T.; Yumerefendi, H.; Bear, J. E.; Kuhlman, B., Engineering an improved light-induced dimer (iLID) for controlling the localization and activity of signaling proteins. *Proc. Natl. Acad. Sci. USA* **2015,** *112* (1), 112–117.
17. Kennedy, M. J.; Hughes, R. M.; Peteya, L. A.; Schwartz, J. W.; Ehlers, M. D.; Tucker, C. L., Rapid blue-light–mediated induction of protein interactions in living cells. *Nat. Methods* **2010,** *7* (12), 973-975.
18. Levskaya, A.; Weiner, O. D.; Lim, W. A.; Voigt, C. A., Spatiotemporal control of cell signalling using a light-switchable protein interaction. *Nature* **2009,** *461* (7266), 997–1001.
19. Bugaj, L. J.; Sabnis, A. J.; Mitchell, A.; Garbarino, J. E.; Toettcher, J. E.; Bivona, T. G.; Lim, W. A., Cancer mutations and targeted drugs can disrupt dynamic signal encoding by the Ras-Erk pathway. *Science* **2018,** *361* (6405), eaao3048.
20. Toettcher, Jared E.; Weiner, Orion D.; Lim, Wendell A., Using Optogenetics to Interrogate the Dynamic Control of Signal Transmission by the Ras/Erk Module. *Cell* **2013,** *155* (6), 1422–1434.
21. Toettcher, J. E.; Gong, D.; Lim, W. A.; Weiner, O. D., Light-based feedback for controlling intracellular signaling dynamics. *Nat. Methods* **2011,** *8* (10), 837–839.
22. Benedetti, L.; Marvin, J. S.; Falahati, H.; Guillén-Samander, A.; Looger, L. L.; De Camilli, P., Optimized Vivid-derived Magnets photodimerizers for subcellular optogenetics in mammalian cells. *eLife* **2020,** *9*, e63230.
23. Hoelzel, C. A.; Zhang, X., Visualizing and Manipulating Biological Processes by Using HaloTag and SNAP-Tag Technologies. *ChemBioChem* **2020,** *21* (14), 1935–1946.
24. Miller, L. W.; Cai, Y.; Sheetz, M. P.; Cornish, V. W., In vivo protein labeling with trimethoprim conjugates: a flexible chemical tag. *Nat. Methods* **2005,** *2* (4), 255–257.
25. Los, G. V.; Encell, L. P.; McDougall, M. G.; Hartzell, D. D.; Karassina, N.; Zimprich, C.; Wood, M. G.; Learish, R.; Ohana, R. F.; Urh, M.; Simpson, D.; Mendez, J.; Zimmerman, K.; Otto, P.; Vidugiris, G.; Zhu, J.; Darzins, A.; Klaubert, D. H.; Bulleit, R. F.; Wood, K. V., HaloTag: A Novel Protein Labeling Technology for Cell Imaging and Protein Analysis. *ACS Chem. Biol.* **2008,** *3* (6), 373–382.
26. Keppler, A.; Gendreizig, S.; Gronemeyer, T.; Pick, H.; Vogel, H.; Johnsson, K., A general method for the covalent labeling of fusion proteins with small molecules in vivo. *Nat. Biotechnol.* **2003,** *21* (1), 86–89.
27. Voß, S.; Klewer, L.; Wu, Y.-W., Chemically induced dimerization: reversible and spatiotemporal control of protein function in cells. *Curr. Opin. Chem. Biol.* **2015,** *28*, 194–201.
28. Kowada, T.; Arai, K.; Yoshimura, A.; Matsui, T.; Kikuchi, K.; Mizukami, S., Optical Manipulation of Subcellular Protein Translocation Using a Photoactivatable Covalent Labeling System. *Angew. Chem. Int. Ed.* **2021,** *60* (20), 11378–11383.
29. Chen, X.; Venkatachalapathy, M.; Kamps, D.; Weigel, S.; Kumar, R.; Orlich, M.; Garrecht, R.; Hirtz, M.; Niemeyer, C. M.; Wu, Y.-W.; Dehmelt, L., "Molecular Activity Painting": Switch-like, Light-Controlled Perturbations inside Living Cells. *Angew. Chem. Int. Ed.* **2017,** *56* (21), 5916–5920.
30. Zimmermann, M.; Cal, R.; Janett, E.; Hoffmann, V.; Bochet, C. G.; Constable, E.; Beaufils, F.;

Wymann, M. P., Cell-Permeant and Photocleavable Chemical Inducer of Dimerization. *Angew. Chem. Int. Ed.* **2014,** *53* (18), 4717–4720.

31. Ballister, E. R.; Aonbangkhen, C.; Mayo, A. M.; Lampson, M. A.; Chenoweth, D. M., Localized light-induced protein dimerization in living cells using a photocaged dimerizer. *Nat. Commun.* **2014,** *5* (1), 5475.

32. Aonbangkhen, C.; Zhang, H.; Wu, D. Z.; Lampson, M. A.; Chenoweth, D. M., Reversible Control of Protein Localization in Living Cells Using a Photocaged-Photocleavable Chemical Dimerizer. *J. Am. Chem. Soc.* **2018,** *140* (38), 11926–11930.

33. Chen, X.; Wu, Y.-W., Tunable and Photoswitchable Chemically Induced Dimerization for Chemo-optogenetic Control of Protein and Organelle Positioning. *Angew. Chem. Int. Ed.* **2018,** *57* (23), 6796–6799.

CHAPTER 2

Protein Labeling Ligand Capable of Binding to the Protein in a Photo-reversible Manner

2-1. Introduction

Light is a useful tool for controlling nanosystems in biology. Recently, the optical regulation of biomolecules has attracted attention as a new research technology in life science.[1-4] Optogenetics, which exploits photo-responsive proteins such as channelrhodopsin-2,[5] has brought innovation in neuroscience.[2] Although this molecular-biology-based technology has rapidly expanded among biologists, the reported biomolecules are limited. Another approach for operating biomolecules with light is the use of organic-chemistry-based caged compounds.[3, 4] Various biomolecules, such as glutamate and ATP, have been inactivated by the modification of a photolabile group, and subsequently activated by light irradiation. Although caged compounds enabled the optical control of diverse biomolecules, one of their limitations is their irreversibility. Thus, a new technology for the reversible optical control of various biomolecules is desired.

One promising approach to photo-reversible control is the use of photochromism. Photochromic compounds undergo photo-reversible isomerization, usually causing changes in their absorption properties and structures.[6] Azobenzene and spiropyran derivatives are well-known photochromic compounds, and various compounds with excellent reversibility, such as the diarylethene derivatives, have also been developed.[7] Recently, a new research field called photopharmacology, in which protein functions are optically controlled with photochromic compounds, has attracted increasing interest. [8-10] In most cases of photopharmacological compound design, azobenzene derivatives have been exploited as a photochromic group, and there have been two strategies to design photopharmacological compounds.[11] One is the “azo-extension” strategy. In this strategy, a photochromic phenylazo group is appended to the original ligands,[12-15] where the steric interaction between the appended photochromic group and the target protein surface is expected to be changed by photoisomerization. This strategy is quite effective and can be applied to various compounds; however, it is more challenging to regulate protein functions efficiently using photopharmacological compounds than caged compounds because the structural differences between both isomers of photochromic compounds are much smaller than those in the case of caged compounds. The other strategy is the “azologization” strategy, where some chemical structures, such as styrenes or *N*-phenyl benzamides, are replaced by azobenzenes.[16-20] The conformation changes in azo-analog compounds upon exposure to light are likely to critically affect their affinity to proteins because proteins specifically recognize the three-dimensional conformations of their ligands by various interactions, such as hydrogen bonds and π-π stacking interactions. It is desirable that only one photoisomer of azo-analogs can work as an isostere of the original bioactive compound whereas the other cannot work due to the quite different conformation from the original ligands.

According to the latter strategy, the author aimed at developing a system for the quantitative control

of enzymatic activity via the reversible binding of the inhibitor to the target protein, *Escherichia coli* dihydrofolate reductase (eDHFR). Since eDHFR is related to folate metabolisms and is an important enzyme for bacteria growth,[21] its inhibitors are known as antibacterial agents. Furthermore, eDHFR has also been exploited as a new tool in chemical biology, where eDHFR and its inhibitors, such as methotrexate (MTX) or trimethoprim (TMP), are used for specific protein labeling.[22, 23] Hence, the optical control of ligand binding to eDHFR would lead to various applications in fields from photopharmacology to chemical biology. In order to achieve the optical control of the eDHFR activity, the author selected MTX as an inhibitor to be derivatized.

2-2. Design of photochromic isostere of MTX

In the crystal structure of the eDHFR–MTX complex (Figure 2-1A), the conformation of MTX bound to eDHFR is bent at the *N*-methylaminomethylene group that links two aromatic groups in MTX. This bent form of MTX seems to be essential for its specific binding to eDHFR, because only the bent form can interact with eDHFR via several hydrogen bonds, especially between D27 and the pteridine ring and between R57 and the carboxylate group (Figure 2-1A). The author has designed azoMTX, an azo-analog of MTX (Figure 2-1B), where the methylaminomethylene group was replaced with an azo group. Generally, azobenzene derivatives show photoisomerization from *E* to *Z* and *Z* to *E*, depending on light irradiation.[6] The extended *E* isomers are induced by visible-light irradiation or heat, whereas the bent *Z* isomers are induced by UV light irradiation; hence, azoMTX is also expected to alter its conformation under light irradiation. The superimposition of azoMTX and MTX indicated that only *Z*-azoMTX mimics the bent conformation of MTX bound to eDHFR, and that the extended conformation, *E*-azoMTX, is very different from the conformation of the bound MTX (Figure 2-2A). Another structural difference between azoMTX and MTX is that pteridine was replaced with quinazoline (Figure 2-2B). This modification was performed to facilitate the synthetic process without changing the compound shape, and it did not critically affect the affinity between eDHFR and the MTX derivatives.[24]

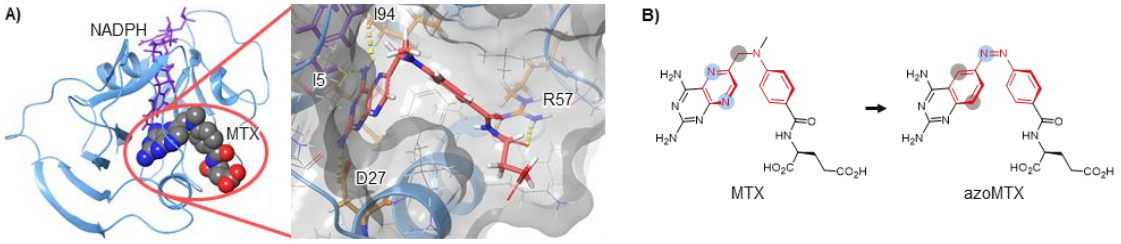

Figure 2-1. (A) A crystal structure of the eDHFR–MTX–NADPH ternary complex (PDB: 4P66). MTX (red stick) interacts with eDHFR with several hydrogen bonds (yellow lines). (B) Structures of MTX and azoMTX (*Z* isomer). The replaced atoms are highlighted.

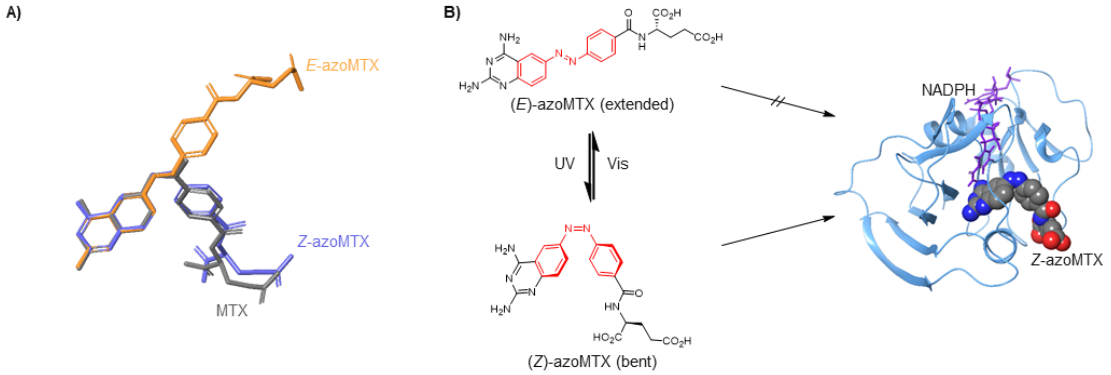

Figure 2-2. (A) The Superimposition of MTX (gray), (*E*)-azoMTX (orange), and Z-azoMTX (blue). (*Z*)-azoMTX mimics the bent conformation of MTX bound to eDHFR though E-azoMTX is very different from the conformation of the bound MTX. (B) Photoisomerization of azoMTX (left) and schematic illustration of the photo-switchable binding of azoMTX to eDHFR (right).

2-3. Photo-isomerization property of azoMTX

AzoMTX was synthesized in seven steps (Scheme 2-1), and its structure was verified by ^{1}H and ^{13}C NMR and by ESI-MS. ^{1}H NMR analysis showed that azoMTX in the thermal equilibrium (dark) state in an aqueous solution existed as only a single isomer (Figure 2-3). The photoisomerization of azoMTX was monitored through the changes in the UV/Vis absorption spectrum (Figure 2-4). UV light irradiation at 394 nm induced *E*-to-*Z* isomerization, whereas irradiation at 560 nm induced *Z*-to-

Scheme 2-1. Synthetic route to azoMTX

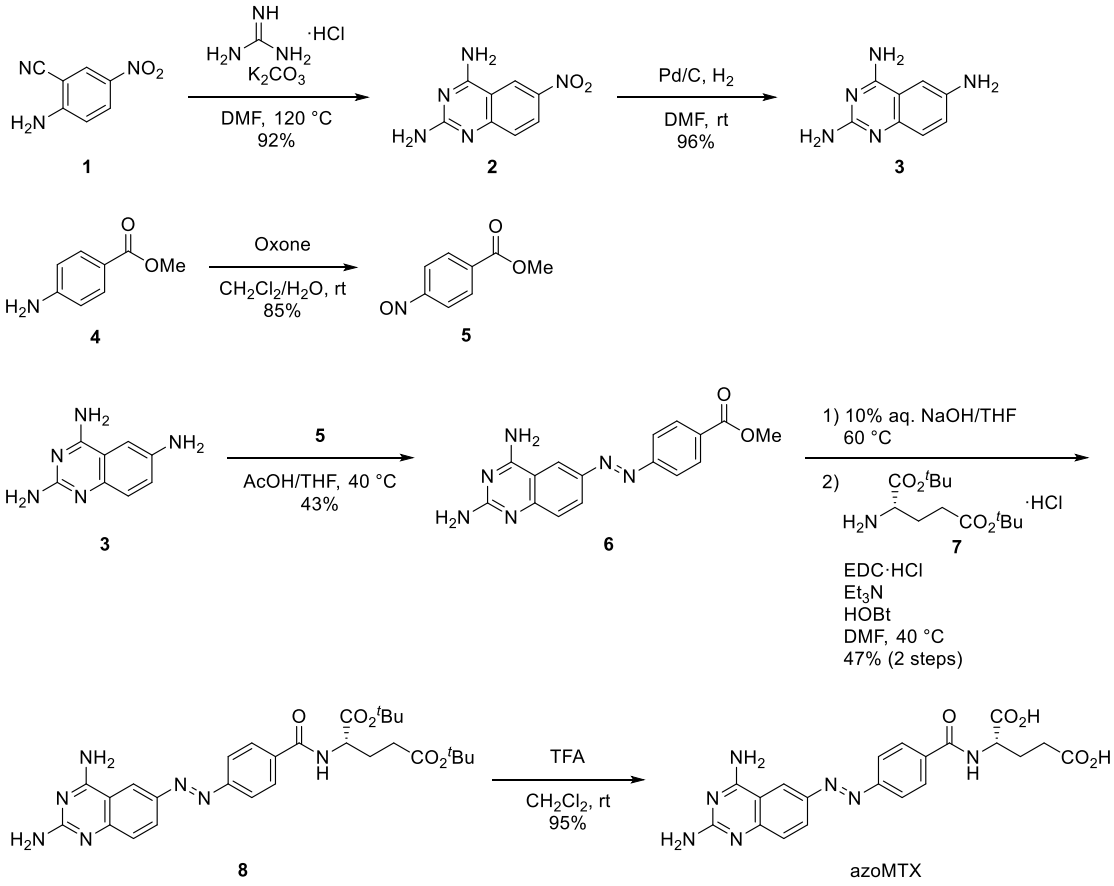

E isomerization. Moreover, it was confirmed that azoMTX could be repeatedly isomerized by alternating use of light of wavelengths 394 and 560 nm (Figure 2-5).

The percentages of the *Z* isomer of azoMTX at the photostationary states (PSSs) for various light irradiation wavelengths were determined by HPLC analyses (Figure 2-6) and are summarized in Table 2-1. The UV/Vis absorption spectra at various PSSs were also obtained (Figure 2-4). The absorption spectrum of (*Z*)-azoMTX (Figures 2-4) was estimated from the spectra of azoMTX in the "dark state" (100 % *E*) and at PSS_{394} (75 % *Z*). The percentages of (*Z*)-azoMTX at the various PSSs were also calculated from the absorption spectra (Table 2-2); the calculated values showed good agreement with those determined by HPLC (Table 2-1). Therefore, light irradiation at various wavelengths enabled the modulation of the molar fraction of (*Z*)-azoMTX from 0 % (dark) to 75 % (PSS_{394}). Thermal relaxation half-life was measured at 25 °C, and $T_{1/2}$ was determined as 5.5 h. (Figure 2-7).

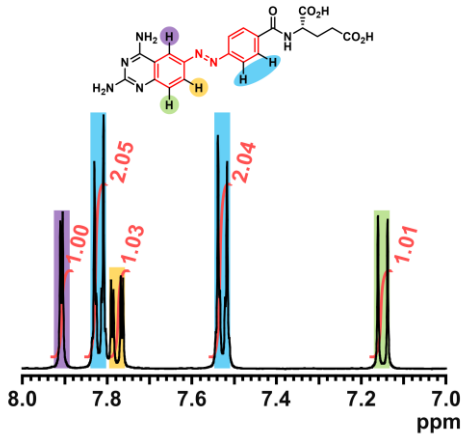

Figure 2-3. ^{1}H NMR spectrum (400 MHz, 25 °C) of azoMTX (10 mM), at the thermal equilibrium state, in D_2O containing 20 mM NaOD. The sample was incubated at 25 °C for 27 h under dark condition before the measurement.

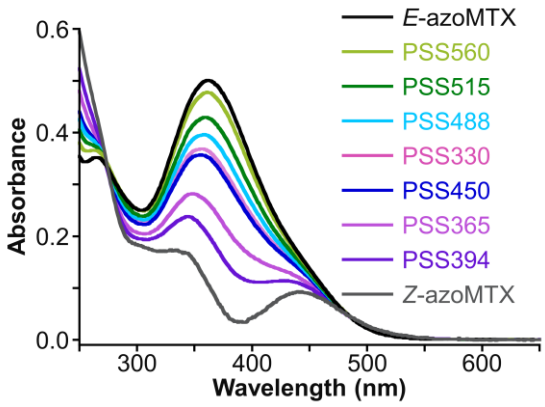

Figure 2-4. UV/vis spectra of azoMTX at the thermal equilibrium state and PSSs. AzoMTX (30 μM) was dissolved in 100 mM HEPES-NaOH buffer (pH 7.4) containing 100 mM NaCl and 1% DMSO at 25 °C and irradiated at various light wavelengths (5.0 mW cm^{-2}) before measurement.

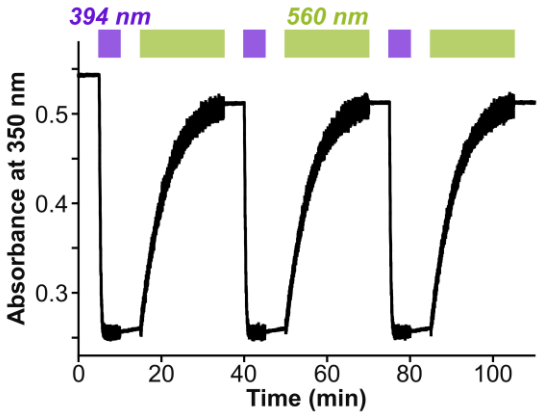

Figure 2-5. Time-dependent absorption changes of azoMTX at 350 nm under alternate light irradiation (6.0 mW cm−2). AzoMTX (30 μM) was dissolved in 100 mM HEPES-NaOH buffer (pH 7.4) containing 100 mM NaCl and 1% DMSO at 25 °C.

Table 2-1. *Z* percentages of azoMTX at various photostationary states (PSSs) determined by HPLC (Figure **2-6**)

Dark	PSS_{330}	PSS_{365}	PSS_{394}	PSS_{450}	PSS_{488}	PSS_{515}	PSS_{560}
< 2%	33%	61%	75%	37%	28%	19%	9%

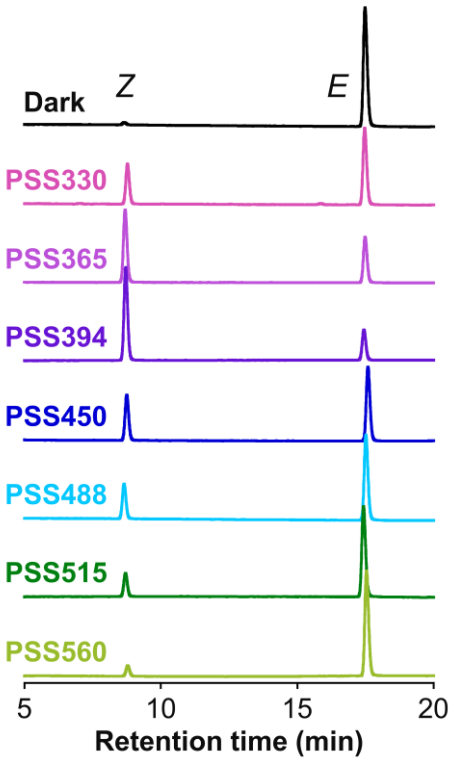

Figure 2-6. HPLC diagrams of azoMTX at the thermal equilibrium state and various photostationary states (PSSs). Detection wavelength was set to 265 nm. Elution was performed with a 20-min linear gradient from 10% acetonitrile/water containing 0.1% formic acid to 20% acetonitrile/water containing 0.1% formic acid.

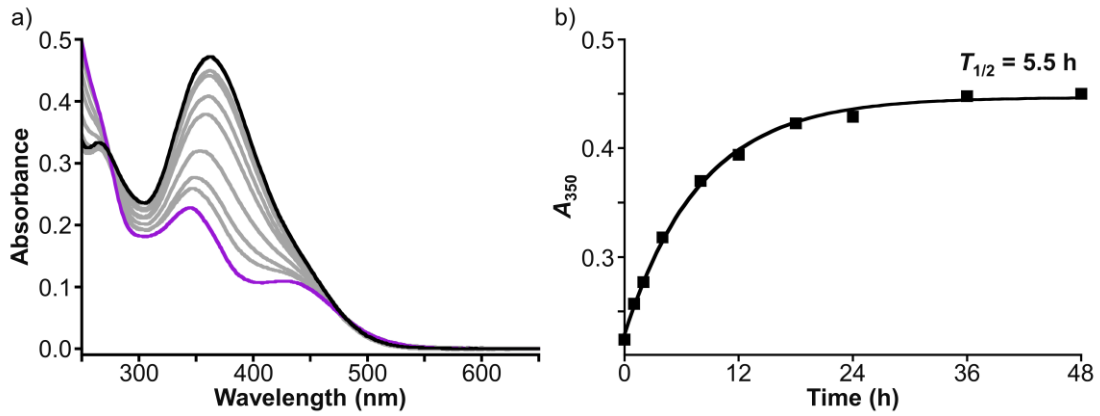

Figure 2-7. Thermal relaxation of azoMTX (30 μM) at 25 °C in 100 mM HEPES-NaOH buffer (pH 7.4) containing 100 mM NaCl and 1% DMSO. The exponential curve fit gave the thermal relaxation half-life, $T_{1/2}$ = 5.5 h, R^2 > 0.99.

Table 2-2. Z percentages of azoMTX at various PSSs determined by UV/vis spectroscopy

PSS_{330}	PSS_{365}	PSS_{394}	PSS_{450}	PSS_{488}	PSS_{515}	PSS_{560}
35%	60%	76%	38%	27%	18%	6%

2-4. Optical regulation of eDHFR enzymatic activity using azoMTX

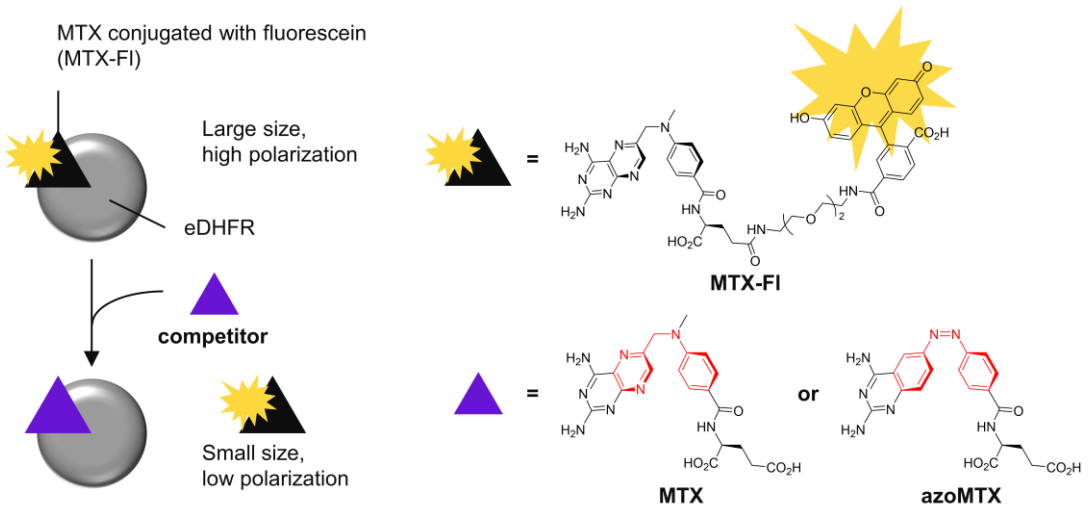

Figure 2-8. Schematic illustration of the competitive fluorescence depolarization assay. Initially, MTX-Fl is bound to eDHFR, and the polarization is high due to the large molecular weight of the fluorescent ligand-protein complex. When the competitor is added to the cuvette, MTX-Fl is expelled, and the polarization decreases.

The affinity between eDHFR and azoMTX was investigated using a competitive fluorescence depolarization assay with a fluorophore-modified MTX (MTX-Fl, Scheme 2-2 and Figure 2-8). As the concentration of the competitor increased, the fluorescence polarization of MTX-Fl decreased (Figure 2-8). The IC_{50} value determined for MTX was (3.2 ± 0.4) nM, whereas those determined for azoMTX were (45 ± 4) nM in the dark state, which contained 100 % (*E*)-azoMTX, and (3.4 ± 0.6) nM after UV irradiation (PSS_{394}). (*E*)-AzoMTX had a higher IC_{50} value than MTX, thus supporting the supposition that the conformation of (*E*)-azoMTX was very different from that of the bound MTX. In contrast, UV irradiation made the IC_{50} value of azoMTX for eDHFR about ten times lower. If azoMTX at the PSS_{394} is assumed to consist of 75 % Z isomer, the IC_{50} value of (*Z*)-azoMTX should be lower than that of azoMTX at the PSS_{394} and is roughly estimated to be around 2.6 nM (= 3.4 nM × 0.75) because 0.8 nM (=3.4 nM × 0.25) of (*E*)-azoMTX shows almost no binding to eDHFR (Figure 2-9). This result suggests that (*Z*)-azoMTX has the almost same affinity towards eDHFR as MTX.

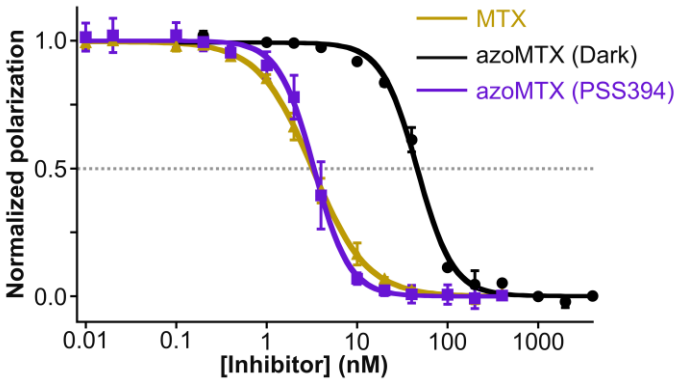

Figure 2-9. Competitive binding assay of azoMTX with eDHFR based on fluorescence depolarization. [MTX-Fl] = 2 nM, [eDHFR] = 2 nM in 100 mM HEPES-NaOH buffer (pH 7.4) containing 100 mM NaCl at 25 °C. Fluorescence polarization measurement: λ_{ex} = 497 nm, λ_{em} = 520 nm. AzoMTX at PSS394 was irradiated with 394/10 nm light at 5.0 mW cm^{-2} for 5 min just before the assay. Error bars show standard deviations (n = 3).

Scheme 2-2. Synthetic route to MTX-Fl

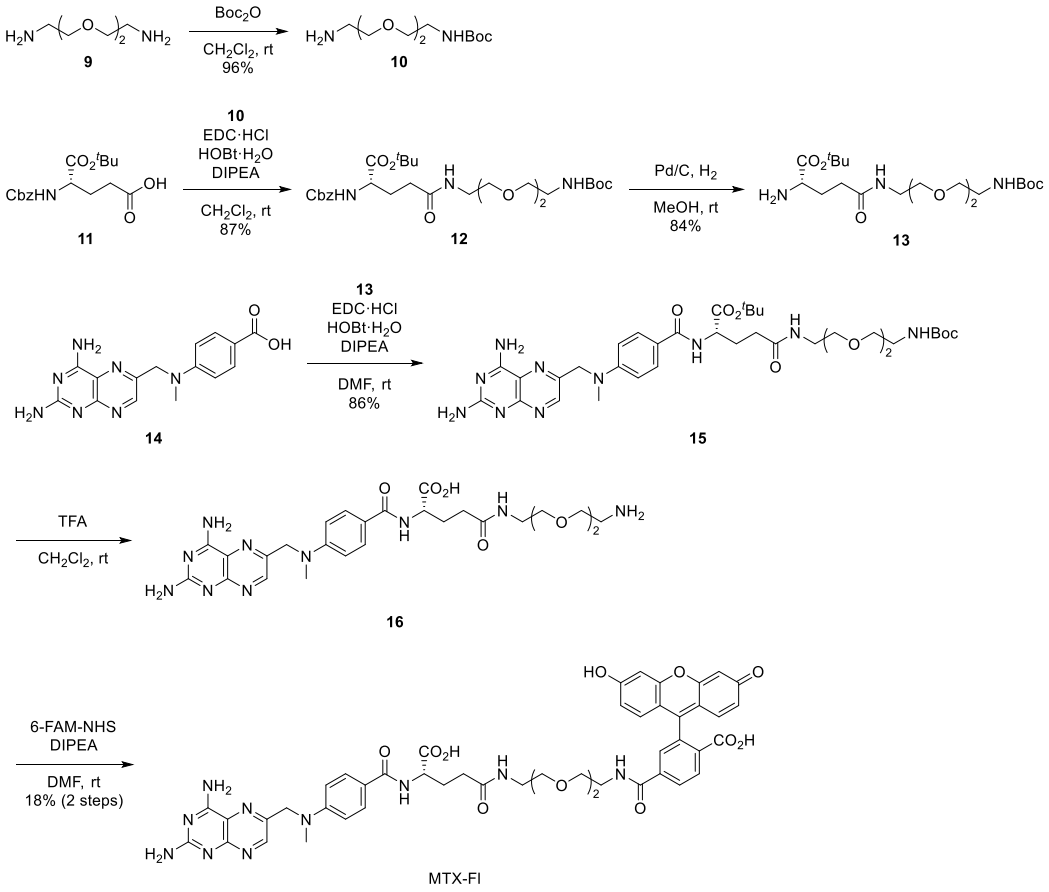

Having demonstrated that the affinity of azoMTX towards eDHFR could be modulated by light irradiation, the author examined optical control over eDHFR activity with azoMTX. eDHFR converts dihydrofolate to tetrahydrofolate by using NADPH as coenzyme. This enzymatic reaction can be followed by the absorption decrease at 340 nm, which indicates the consumption of NADPH. In the

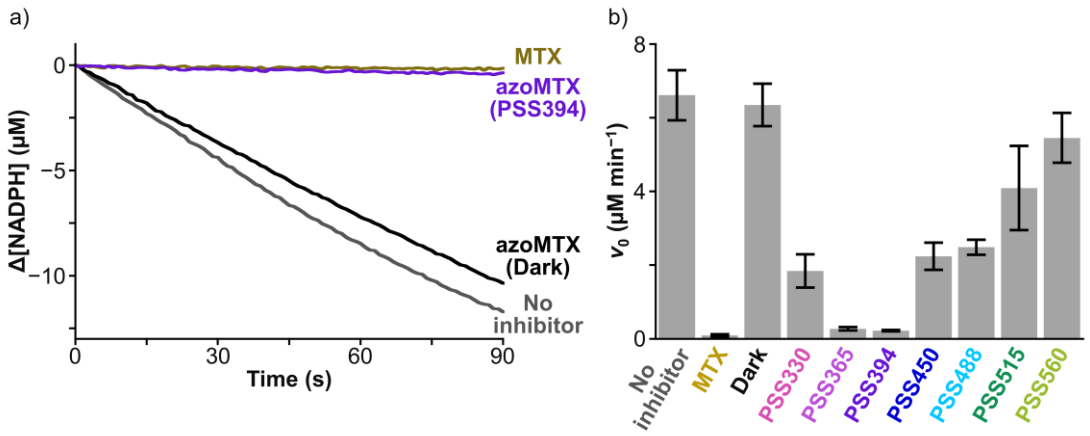

Figure 2-10. (a) NADPH consumption by eDHFR enzyme with and without inhibitors. (b) Initial rate of enzyme reaction (v_0) with and without inhibitors. [eDHFR] = 10 nM, [NADPH] = 60 μM, [dihydrofolate] = 50 μM, and [inhibitor] = 50 nM in 100 mM HEPES-NaOH buffer (pH 7.4) containing 100 mM NaCl at 25 °C. AzoMTX at various PSSs was irradiated with various light wavelengths (5.0 mW cm^{-2}) just before the measurement. Enzyme reaction was initiated by the addition of dihydrofolate.

presence of 50 nM azoMTX, only a slight inhibition of the enzyme reaction was observed under dark conditions, whereas the reaction was almost completely inhibited at the PSS_{394} (Figure 2-10 a,b). This result indicates that only (*Z*)-azoMTX can function as an isostere of MTX. The inhibition activities were then examined under light irradiation at various wavelengths. As expected, the inhibition efficiency could be regulated by changing the irradiation wavelength (Figure 2-10b). Because the proportions of (*E*)- and (*Z*)-azoMTX at the various PSSs were clearly regulated (Table 2-1), the concentration of (*Z*)-azoMTX, behaving as an isostere of MTX, was also regulated; hence, the inhibition efficiency was modulated in a manner that was dependent on the irradiation wavelength.

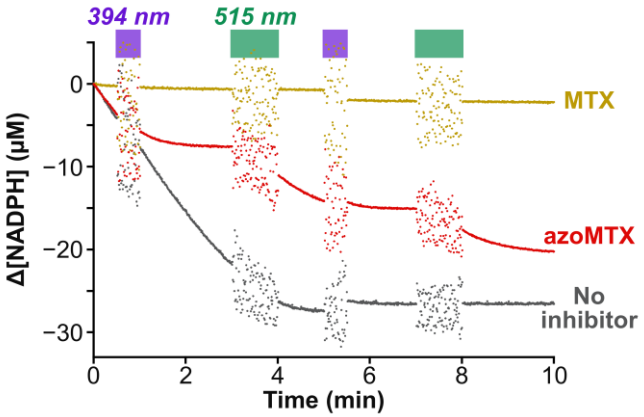

Figure 2-11. Reversible photoregulation of enzyme reaction with azoMTX. [eDHFR] = 5 nM, [NADPH] = 90 μM, [dihydrofolate] = 75 μM, and [inhibitor] = 100 nM in 100 mM HEPES-NaOH buffer (pH 7.4) containing 100 mM NaCl at 25 °C. Light intensity was set to 7.6 mW cm^{-2} for 394 nm and 8.9 mW cm^{-2} for 515 nm.

Finally, the author tried real-time optical control of the enzymatic reaction. The reaction was monitored under alternating irradiation with 394 and 515 nm light in the presence of 100 nM azoMTX (Figure 2-11). Initially, the reaction proceeded under dark conditions, whereas the application of 394 nm light irradiation made the reaction slower and almost completely inhibited it within a few minutes. Under these inhibition conditions, the use of 515 nm light irradiation restarted the enzyme reaction, and this inhibition/restart cycle was repeatable. This result shows that azoMTX can associate with and dissociate from eDHFR repeatedly as a result of changes in irradiation wavelength, and hence that azoMTX can dynamically control the eDHFR activity.

2-5. Conclusion

In conclusion, the author has developed a photo-switchable inhibitor, azoMTX, which can efficiently switch affinity with eDHFR and enzyme activity depending on light wavelength. The structure of azoMTX was rationally designed on the basis of the eDHFR–MTX complex structure, such that only the *Z*-isomer could form a conformation almost identical to that of the MTX bound to eDHFR. The *E*-to-*Z* and *Z*-to-*E* photoisomerizations of azoMTX were regulated using light of wavelengths 394 and 560 nm, respectively. Under 394-nm light irradiation, azoMTX showed ~10-fold increase in the affinity to eDHFR. This photochromic property also led to light-wavelength-based quantitative control and real-time reversible OFF/ON switching of the eDHFR activity. Importantly, this system could be used for photo-reversible protein labeling, because eDHFR has been widely used as a tag protein with MTX or TMP in life science.[22, 23] Exploiting eDHFR and caged TMP, irreversible photo-activatable protein labeling systems have been developed and applied to photo-induced protein dimerization.[25-28] Therefore, the author envisions that azoMTX will be applied to not only optical control of the enzyme activity but also a photo-reversible protein labeling system, leading to the development of new chemical biology tools for the optical manipulation of biomolecular functions.

Gorostiza et al. reported the identical molecular design for optical control of human DHFR activity.[29] Their result in which the *Z*-isomer also inhibits the activity of human DHFR is reasonable because the parent compound, MTX, is known as the inhibitor of both eDHFR and human DHFR.[30] This indicates that *Z*-azoMTX binds to endogenous DHFR in mammalian cells and affects the cellular functions. Therefore, the development of eDHFR-specific azoMTX derivatives for photo-reversible protein labeling systems will be a significant research topic.

2-6. Experimental section (chapter 2)

Materials and instruments

Unless otherwise specified, all reagents were purchased from the chemical suppliers Fujifilm Wako Pure Chemical Corporation (Osaka, Japan), Tokyo Chemical Industry Co. (Tokyo, Japan), Kanto Chemical Co. (Tokyo, Japan), Nacalai Tesque (Kyoto, Japan), Watanabe Chemical Industries (Hiroshima, Japan), and Sigma-Aldrich Japan K.K. (Tokyo, Japan). They were used without further purification. Restriction enzymes were purchased from New England Biolabs Japan Inc. (Tokyo, Japan). AzoMTX was dissolved in DMSO (spectrochemical analysis grade, Wako) before spectroscopic measurements, to facilitate its solubilization in aqueous solution.

NMR spectra were recorded on a Bruker AVANCE III 400 instrument at 400 MHz for ^{1}H NMR and 101 MHz for ^{13}C NMR or a Bruker AVANCE III 500 instrument at 500 MHz for ^{1}H NMR and 126 MHz for ^{13}C NMR. Chemical shifts (δ) are quoted in ppm downfield from tetramethylsilane, referenced to residual solvent signals (^{1}H NMR: δ = 7.26 for $CDCl_3$, 2.50 for DMSO-d_6, 3.31 for CD_3OD, and 4.79 for D_2O; ^{13}C NMR: δ = 39.5 for DMSO-d_6 and 49.1 for CD_3OD). The high-resolution mass spectrometry analyses were performed on a Bruker micrOTOF-Q II mass spectrometer. HPLC analyses and purification were performed with an Inertsil ODS-3 column (4.6 mm × 250 mm for analysis or 14.0 mm × 250 mm for purification, GL-Science Inc.), using an HPLC system that comprised a pump (PU-2080, JASCO) and a detector (MD-2018, JASCO), and the absorbance was monitored at 215, 254, and 280 nm unless otherwise specified. Buffer A was composed of 0.1% formic acid in water. Buffer B was composed of 0.1% formic acid in acetonitrile. UV/vis absorption spectra and time-dependent absorption change were measured by using a SHIMADZU UV-2450 spectrophotometer, with the slit width set to 1 nm. For photoisomerization analysis of azoMTX, light irradiation was performed by using a Xe light source (MAX-303; Asahi Spectra) equipped with band-pass filters (330/10, 365/10, 394/10, 450/10, 488/10, 515/10, or 560/10 nm). Fluorescence polarization was measured by using a JASCO FP-8500 spectrometer. The slit widths were set to 10 nm for both excitation and emission. Excitation and emission wavelengths were set to 497 nm and 520 nm, respectively.

Synthesis of azoMTX

Synthesis of 6-nitroquinazoline-2,4-diamine (**2**)[31]

The solution of **1** (5.00 g, 30.6 mmol), guanidine hydrochloride (3.50 g, 36.6 mmol), and potassium carbonate (10.1 g, 73.1 mmol) in dry DMF (70 mL) was heated and stirred at 120 °C under a nitrogen atmosphere for 13 h. After cooling, volatile materials were removed in vacuo. The remaining solid was washed with water and acetone to give **2** (5.74 g, 28.0 mmol, 92%) as an orange solid.
^{1}H NMR (400 MHz, DMSO-d_6): δ 9.07 (d, J = 2.5 Hz, 1H), 8.20 (dd, J = 9.3 Hz, 2.5 Hz, 1H), 7.81 (br s, 2H), 7.21 (d, J = 9.3 Hz, 1H), 6.72 (br s, 2H).

Synthesis of quinazoline-2,4,6-triamine (**3**)[32]

The suspension of **2** (1.00 g, 4.87 mmol) and 10% palladium on carbon (Pd/C, 101 mg, 10 wt%) in DMF (50 mL) was stirred at ambient temperature under a hydrogen atmosphere for 11 h. After the removal of palladium on carbon through Celite 535, the filtrate was concentrated in vacuo to give **3** (822 mg, 4.69 mmol, 96%) as a pale brown solid.
^{1}H NMR (400 MHz, D_2O) δ 7.11 (dd, J = 8.7, 2.2 Hz, 1H), 7.06 (d, J = 8.7 Hz, 1H), 6.91 (d, J = 2.2 Hz, 1H).

Synthesis of methyl 4-nitrosobenzoate (**5**)[33]

To the solution of **4** (1.00 g, 6.62 mmol) in dichloromethane (25 mL) was added oxone (8.11 g, 13.2 mmol) in water (100 mL), and the mixture was stirred at ambient temperature for 1 h. After the separation of organic and water layers, the organic materials were extracted with dichloromethane (2 × 50 mL). The combined organic layer was washed with 1 M aqueous hydrochloric acid solution (100 mL), saturated aqueous sodium bicarbonate solution (75 mL), water (75 mL), and brine (75 mL). The organic layer was dried over magnesium sulfate and concentrated in vacuo. The crude material was purified by recrystallization from ethyl acetate to give **5** (931 mg, 5.64 mmol, 85%) as a yellow crystal.
^{1}H NMR (400 MHz, $CDCl_3$) δ 8.30 (d, J = 8.6 Hz, 2H), 7.94 (d, J = 8.6 Hz, 2H), 3.98 (s, 3H).

Synthesis of methyl (*E*)-4-[(2,4-diaminoquinazolin-6-yl)diazenyl]benzoate (**6**)

The solution of **3** (359 mg, 1.53 mmol), **5** (470 mg, 2.85 mmol) in THF (8.0 mL), and acetic acid (8.0 mL) was stirred at 40 °C for 18 h. After the removal of the volatile materials in vacuo, the remaining solid was washed with water, methanol, and dichloromethane to give **6** (210 mg, 652 μmol, 43%) as a brown solid.
^{1}H NMR (400 MHz, DMSO-d_6) δ 8.76 (d, J = 2.2 Hz, 1H), 8.16 (d, J = 8.7 Hz, 2H), 8.04 (dd, J = 9.1, 2.2 Hz, 1H), 7.93 (d, J = 8.7 Hz, 2H), 7.64 (br s, 2H), 7.26 (d, J = 9.1 Hz, 1H), 6.49 (br s, 2H), 3.90 (s, 3H); ^{13}C NMR (101 MHz, DMSO-d_6) δ 172.1, 165.7, 163.2, 162.1, 155.8, 154.9, 145.4, 130.5, 126.4, 125.4, 122.5, 122.2, 109.9, 52.3; HRMS (ESI$^+$) m/z: Calcd. for $C_{16}H_{15}N_6O_2^+$ $[M+H]^+$ 323.1251, found 323.1256.

Synthesis of di-tert-butyl (*E*)-{4-[(2,4-diaminoquinazolin-6-yl)diazenyl]benzoyl}-L-glutamate (**8**)

The suspension of **6** (76.6 mg, 238 μmol) in THF (6.0 mL) and a 10% aqueous solution of sodium hydroxide (6.0 mL) was heated and stirred at 60 °C for 14 h. After cooling, the reaction mixture was neutralized with 1 M aqueous hydrochloric acid solution at 0 °C. After concentration in vacuo, the residue was washed with water and THF to give crude material (54.1 mg) as a brown solid. The suspension of crude material (54.1 mg), **7** (50.2 mg, 170 μmol), 1-ethyl-3-(3-dimethylaminopropyl)carbodiimide monohydrochloride (EDC·HCl, 35.6 mg, 186 μmol), 1-hydroxy-1*H*-benzotriazole hydrate (HOBt·H_2O, 26.0 mg, 170 μmol), and triethylamine (52 μL, 38 mg, 3.7 × 10^2 μmol) in dry DMF (17 mL) was stirred at 40 °C under a nitrogen atmosphere for 26 h. After the addition of a saturated aqueous sodium bicarbonate solution (20 mL) at 0 °C, the organic materials were extracted with dichloromethane (4 × 30 mL). The organic layer was washed with saturated aqueous ammonium chloride solution (60 mL) and brine (100 mL), dried over sodium sulfate and concentrated in vacuo. The crude material was purified by silica gel column chromatography (5–10% methanol/dichloromethane) to give **8** (59.7 mg, 109 μmol, 47% (2 steps)) as an orange solid.
^{1}H NMR (400 MHz, DMSO-d_6) δ 8.27–8.20 (m, 2H), 7.98 (d, J = 8.6 Hz, 2H), 7.92 (d, J = 8.6 Hz, 2H), 7.52 (d, J = 8.9 Hz, 1H), 7.19 (d, J = 7.2 Hz, 1H), 5.71 (br s, 2H), 5.08 (br s, 2H), 4.72–4.65 (m, 1H), 2.52–2.04 (m, 4H), 1.51 (s, 9H), 1.43 (s, 9H); ^{13}C NMR (101 MHz, DMSO-d_6) δ 171.6, 171.1, 166.1, 163.2, 162.2, 156.0, 153.9, 145.3, 135.1, 128.8, 126.1, 125.6, 122.4, 121.9, 109.9, 80.7, 79.9, 52.7, 31.4, 27.8, 27.7, 25.9; HRMS (ESI$^+$) m/z: Calcd. for $C_{28}H_{36}N_7O_5^+$ $[M+H]^+$ 550.2772, found 550.2779.

Synthesis of (*E*)-{4-[(2,4-diaminoquinazolin-6-yl)diazenyl]benzoyl}-L-glutamic acid (azoMTX)

The solution of **9** (59.7 mg, 109 μmol) in dry dichloromethane (8.0 mL) and trifluoroacetic acid (TFA, 2.0 mL) was stirred at ambient temperature under a nitrogen atmosphere for 15 h. After the removal of the volatile materials in vacuo, the residue was washed with dichloromethane and acetonitrile to give azoMTX (45.3 mg, 104 μmol, 95%) as an orange solid.
^{1}H NMR (500 MHz, DMSO-d_6) δ 12.50 (br s, 2H), 8.88 (d, J = 2.0 Hz, 1H), 8.81 (d, J = 7.7 Hz, 1H), 8.65 (br s, 2H), 8.22 (dd, J = 9.0, 2.0 Hz, 1H), 8.11 (d, J = 5.0 Hz, 2H), 7.96 (d, J = 5.0 Hz, 2H), 7.61 (br s, 2H), 7.51 (d, J = 9.0 Hz, 1H), 4.48–4.41 (m, 1H), 2.39 (t, J = 7.5 Hz, 2H), 2.17–2.08 (m, 1H), 2.03–1.93 (m, 1H); ^{13}C NMR (126 MHz, DMSO-d_6) δ 173.9, 173.4, 165.8, 163.2, 158.6, 158.4, 153.5, 147.0, 135.9, 128.9, 125.2, 124.2, 122.2, 120.8, 109.9, 52.1, 30.5, 26.0; HRMS (ESI$^+$) m/z: Calcd. for $C_{20}H_{20}N_7O_5^+$ $[M+H]^+$ 438.1520, found 438.1539.

Synthesis of MTX-Fl

Synthesis of *tert*-butyl (*S*)-18-{[(benzyloxy)carbonyl]amino}-2,2-dimethyl-4,15-dioxo-3,8,11-trioxa-5,14-diazanonadecan-19-oate (**12**)

Compound **10** was prepared according to the previously described procedures.[34] The solution of **10** (265 mg, 1.07 mmol), **11** (242 mg, 717 μmol), EDC·HCl (164 mg, 856 μmol), HOBt·H_2O (120 mg, 783 μmol), and diisopropylethylamine (DIPEA, 3.0×10^2 μL, 2.2×10^2 mg, 1.7 mmol) in dry dichloromethane (2.0 mL) was stirred at ambient temperature under a nitrogen atmosphere for 14 h. After the addition of a saturated aqueous ammonium chloride solution (3 mL) at 0 °C, the organic materials were extracted with dichloromethane (3 × 5 mL). The organic layer was washed with a saturated aqueous sodium bicarbonate solution (30 mL) and brine (40 mL), dried over magnesium sulfate and concentrated in vacuo. The crude material was purified by silica gel column chromatography (0–5% methanol/dichloromethane) to give **12** (353 mg, 622 μmol, 87%) as a pale yellow oil.

^{1}H NMR (400 MHz, DMSO-d_6) δ 7.86 (t, J = 5.5 Hz, 1H), 7.59 (d, J = 7.8 Hz, 1H), 7.41–7.23 (m, 5H), 6.74 (t, J = 5.4 Hz, 1H), 5.03 (dd, J = 18.7, 12.5 Hz, 2H), 3.92–3.83 (m, 1H), 3.48 (s, 4H), 3.37 (q, J = 6.3 Hz, 4H), 3.18 (q, J = 5.8 Hz, 2H), 3.05 (q, J = 6.0 Hz, 2H), 2.16 (t, J = 7.6 Hz, 2H), 1.97–1.85 (m, 1H), 1.80–1.67 (m, 1H), 1.39 (s, 9H), 1.37 (s, 9H); ^{13}C NMR (101 MHz, DMSO-d_6) δ 171.4, 171.3, 156.0, 155.6, 137.0, 128.3, 127.8, 127.7, 80.5, 77.6, 69.5, 69.4, 69.1, 65.4, 54.9, 54.2, 38.5, 31.5, 28.2, 27.6, 26.7; HRMS (ESI$^+$) m/z: Calcd. for $C_{28}H_{45}N_3O_9Na^+$ $[M+Na]^+$ 590.3048, found 590.3071.

Synthesis of *tert*-butyl (*S*)-18-amino-2,2-dimethyl-4,15-dioxo-3,8,11-trioxa-5,14-diazanonadecan-19-oate (**13**)

The suspension of **12** (326 mg, 574 μmol) and Pd/C (32.4 mg, 10 wt%) in methanol (2.0 mL) was stirred at ambient temperature under a hydrogen atmosphere for 3 h. After the removal of palladium on carbon through Celite 535, the filtrate was concentrated in vacuo to give **13** (237 mg, 547 μmol, 95%) as a colorless oil.

^{1}H NMR (400 MHz, DMSO-d_6) δ 7.84 (t, J = 5.4 Hz, 1H), 6.74 (br s, 1H), 3.49 (s, 4H), 3.38 (q, J = 6.5 Hz, 4H), 3.17 (q, J = 5.8 Hz, 2H), 3.13 (dd, J = 8.1, 5.2 Hz, 1H), 3.06 (q, J = 6.0 Hz, 2H), 2.14 (t, J = 7.8 Hz, 2H), 1.83–1.72 (m, 1H), 1.63–1.50 (m, 1H), 1.41 (s, 9H), 1.37 (s, 9H), (An NH_2 peak was overlapped.); ^{13}C NMR (101 MHz, DMSO-d_6) δ 175.0, 171.8, 155.6, 79.8, 77.6, 69.5, 69.4, 69.2, 69.1, 54.1, 38.5, 31.6, 30.6, 28.2, 27.7, (Two peaks were overlapped.); HRMS (ESI$^+$) m/z: Calcd. for $C_{20}H_{40}N_3O_7^+$ $[M+H]^+$ 434.2861, found 434.2876.

Synthesis of *tert*-butyl (*S*)-18-(4-{[(2,4-diaminopteridin-6-yl)methyl](methyl)amino}benzamido)-2,2-dimethyl-4,15-dioxo-3,8,11-trioxa-5,14-diazanonadecan-19-oate (**15**)

The suspension of **13** (60.4 mg, 139 μmol), **14** (30.7 mg, 94.4 μmol), EDC·HCl (21.6 mg, 113 μmol), HOBt·H_2O (14.0 mg, 91.4 μmol), and DIPEA (40 μL, 30 mg, 2.3×10^2 μmol) in dry DMF (2.0 mL) was stirred at ambient temperature under a nitrogen atmosphere for 28 h. After the removal of the volatile materials in vacuo, the residue was dissolved in dichloromethane (30 mL) and washed with a saturated aqueous sodium bicarbonate solution (30 mL). After the organic materials were extracted with dichloromethane (15 mL × 3), the combined organic layer was washed with brine (30 mL), dried over sodium sulfate, and concentrated in vacuo. The crude material was purified by silica gel column chromatography (7–10% methanol/dichloromethane) to give **15** (60.1 mg, 81.1 μmol, 86%) as a pale yellow oil.

^{1}H NMR (400 MHz, CD_3OD) δ 8.55 (s, 1H), 7.74 (d, *J* = 9.0 Hz, 2H), 6.84 (d, *J* = 9.0 Hz, 2H), 4.83 (s, 2H), 4.42 (dd, *J* = 9.6, 4.5 Hz, 1H), 3.53 (s, 4H), 3.46 (t, *J* = 5.7 Hz, 2H), 3.34–3.32 (overlapped with CD_2HOD), 3.24 (s, 3H), 3.19 (t, *J* = 5.6 Hz, 2H), 2.36 (t, *J* = 6.7 Hz, 2H), 2.26–2.16 (m, 1H), 2.12–2.00 (m, 1H), 1.46 (s, 9H), 1.41 (s, 9H); ^{13}C NMR (101 MHz, CD_3OD) δ 175.1, 173.0, 170.2, 164.7, 164.1, 158.4, 155.5, 153.2, 150.3, 149.2, 130.2, 123.3, 122.5, 112.7, 82.9, 80.1, 71.2, 71.1, 70.5, 56.6, 54.9, 41.2, 40.4, 39.8, 33.4, 28.8, 28.3, 28.1, (Two peaks were overlapped.); HRMS (ESI^+) *m*/*z*: Calcd. for $C_{35}H_{52}N_{10}O_8Na^+$ $[M+Na]^+$ 763.3862, found 768.3873.

Synthesis of N^5-{2-[2-(2-aminoethoxy)ethoxy]ethyl}-N^2-(4-{[(2,4-diaminopteridin-6-yl)methyl](methyl)amino}benzoyl)-L-glutamine (**16**)

The solution of **15** (60.1 mg, 81.1 μmol) in dry dichloromethane (2.0 mL) and TFA (2.0 mL) was stirred at ambient temperature under a nitrogen atmosphere for 14 h. After the removal of the volatile materials in vacuo, the crude **16** was used for the next reaction without further purification.

^{1}H NMR (400 MHz, CD_3OD) δ 8.64 (s, 1H), 7.77 (d, *J* = 9.1 Hz, 2H), 6.86 (d, *J* = 9.1 Hz, 2H), 4.92 (s, 2H), 4.55 (dd, *J* = 9.3, 4.7 Hz, 1H), 3.68 (t, *J* = 5.1 Hz, 2H), 3.66–3.59 (m, 4H), 3.52 (t, *J* = 5.6 Hz, 2H), 3.43–3.32 (m, 2H), 3.27 (s, 3H), 3.11 (t, *J* = 5.1 Hz, 2H), 2.38 (t, *J* = 7.7 Hz, 2H), 2.33–2.22 (m, 1H), 2.16–2.06 (m, 1H); MS (ESI^+) *m*/*z*: Calcd. for $C_{26}H_{37}N_{10}O_6^+$ $[M+H]^+$ 585.29, found 585.30.

Synthesis of (*S*)-1-[4-carboxy-3-(6-hydroxy-3-oxo-3H-xanthen-9-yl)phenyl]-15-(4-{[(2,4-diaminopteridin-6-yl)methyl](methyl)amino}benzamido)-1,12-dioxo-5,8-dioxa-2,11-diazahexadecan-16-oic acid (MTX-Fl)

6-FAM-NHS was prepared according to the previously described procedures.[35] The solution of crude **16**, 6-FAM-NHS (50.9 mg, 108 μmol), and DIPEA (95 μL, 71 mg, 5.5×10^2 μmol) in dry DMF (4.0 mL) was stirred at ambient temperature under a nitrogen atmosphere for 17 h. After the removal of the volatile materials in vacuo, the crude material was purified by HPLC to give MTX-Fl (18.0 mg, 19.1 μmol, 18% (2 steps)) as a yellow solid.

^{1}H NMR (500 MHz, DMSO-d_6) δ 10.18 (br s, 2H), 8.77 (t, J = 5.6 Hz, 1H), 8.59 (s, 1H), 8.26 (d, J = 7.5 Hz, 1H), 8.17 (dd, J = 8.0, 1.3 Hz, 1H), 8.10–8.03 (m, 2H), 7.87 (t, J = 5.6 Hz, 1H), 7.83 (br s, 1H), 7.72 (d, J = 9.1 Hz, 2H), 7.69 (s, 1H), 6.98 (br s, 2 H), 6.81 (d, J = 9.1 Hz, 2H), 6.69 (d, J = 2.2 Hz, 2H), 6.59 (d, J = 8.7 Hz, 2H), 6.55 (dd, J = 8.7, 2.2 Hz, 2H), 4.80 (s, 2H), 4.31–4.24 (m, 1H), 3.48–3.40 (m, 5H), 3.35 (t, J = 5.6 Hz, 2H), 3.31 (t, J = 6.0 Hz, 2H), 3.21 (s, 4H), 3.11 (q, J = 5.8 Hz, 2H), 2.19 (t, J = 8.2 Hz, 2H), 2.08–1.99 (m, 1H), 1.94–1.85 (m, 1H); ^{13}C NMR (126 MHz, DMSO-d_6) δ 173.8, 171.7, 168.1, 166.2, 164.6, 162.7, 161.1, 159.6, 152.7, 151.8, 150.9, 149.0, 147.3, 140.5, 129.4, 129.3, 128.9, 128.2, 124.9, 122.3, 121.6, 121.2, 112.8, 111.1, 109.2, 102.3, 83.3, 69.4, 69.0, 68.6, 54.9, 52.3, 48.6, 38.5, 31.9, 26.5, (Three peaks could not be discriminated due to overlap with another peak.); HRMS (ESI$^+$) *m*/*z*: Calcd. for $C_{47}H_{47}N_{10}O_{12}^+$ $[M+H]^+$ 943.3369, found 943.3359.

Construction of expression vectors

Escherichia coli (*E. coli*) dihydrofolate reductase (eDHFR)

A gene coding eDHFR was obtained from the plasmid pLL-1 (Active Motif) using a standard PCR method. The forward primer introduced a unique *Nde*I restriction site, and the reverse primer introduced a unique *Bam*HI restriction site. The sequence of the forward primer is 5′-GTA CAT ATG ATC AGT CTG ATT GCG GCG TTA GCG G-3′. The sequence of the reverse primer is 5′-CAA GGA TCC TTA CCG CCG CTC CAG AAT CTC AAA GC-3′. The PCR product was purified by gel after digestion with *Nde*I and *Bam*HI. The fragment was ligated into a modified pET-28a(+) plasmid, in which a sequence inserted for His-tag cleavage by a thrombin protease was replaced with a sequence encoding a TEV protease recognition sequence (ENLYFQG) and a following linker (GGGS). The resulting expression vector was termed pET28tev-eDHFR.

His-tagged Tobacco etch virus NIa proteinase (TEV protease)

A synthetic gene coding TEV protease (S219V-238Δ)[36] was purchased from Eurofins Genomics. An *Nde*I/*Xho*I fragment containing the protease gene was inserted into a corresponding region of non-modified pET-28a(+) to achieve a pET28-TEV expression vector.

Preparation of proteins

eDHFR

E. coli strain BL21(DE3) (Nippon Gene) was transformed with pET28tev-eDHFR and grown at 37 °C in LB medium (Becton, Dickinson) containing 20 μg mL^{-1} kanamycin. When OD_{600} reached 0.7, IPTG (final concentration: 0.4 mM) was added to induce eDHFR at 37 °C. After a 4 h induction, the cells were harvested by centrifugation at 3,800 × *g* for 20 min. The cell pellet was re-suspended in 30 mL of Buffer A (20 mM Tris-HCl, pH 7.4, 350 mM NaCl, 1 mM phenylmethylsulfonyl fluoride, 0.5 mM dithiothreitol (DTT), and 10% glycerol) and lysed by sonication. After the lysate was centrifuged at 3,800 × *g* for 20 min, the supernatant was loaded on a HisTrap HP column (GE Healthcare), equilibrated with Buffer B (20 mM Tris-HCl, pH 7.4, 350 mM NaCl, 0.5 mM DTT, and

10% glycerol) containing 10 mM imidazole. Elution of the His-tagged eDHFR was performed using an imidazole gradient from 10 to 270 mM in Buffer B. The appropriate fractions were collected and repeatedly ultra-filtered (Amicon Ultra-15, cut off 10 kDa, Millipore) for buffer exchange to Buffer C (50 mM Tris-HCl, pH 8.0, 1 mM DTT, 0.5 mM ethylenediaminetetraacetate, and 10% glycerol). The purified protein (400 μM) was incubated with His-tagged TEV protease (3.9 μM) at 4 °C for 16 h for tag removal. The digestion solution was passed through a HisTrap HP column to remove any protein/peptide containing the His-tag. Untagged eDHFR was repeatedly ultra-filtered for buffer exchange to Buffer D (20 mM HEPES-NaOH, pH 7.4, 1 mM DTT, and 10% glycerol). The concentrated protein was stored at −80 °C until use. The concentration of eDHFR was calculated from absorbance at 280 nm (ε_{280} = 74.6 mM^{-1} cm^{-1}).[37]

His-tagged TEV protease

E. coli BL21(DE3) carrying pET28-TEV was grown at 37 °C in the LB medium containing kanamycin until OD_{600} reached 0.7. After a 6 h induction with 0.5 mM IPTG at 37 °C, the cells were harvested by centrifugation at 3,800 × *g* for 20 min. The cell pellet was re-suspended in Buffer B and lysed by sonication. After the lysate was centrifuged at 15,700 × *g* for 30 min, the supernatant was loaded on a HisTrap HP column equilibrated with Buffer B containing 10 mM imidazole. Elution of the His-tagged TEV protease was performed using an imidazole gradient from 25 to 275 mM in Buffer B. The appropriate fractions were repeatedly ultra-filtered for buffer exchange to Buffer B. The concentrated protein was stored at –80 °C until use. The absorption coefficient of the His-tagged TEV protease was calculated by a ProtParam tool at an ExPASy web site (ε_{280} = 32 mM^{-1} cm^{-1}).

Photo- and thermal isomerization of azoMTX

AzoMTX was dissolved in 100 mM HEPES-NaOH buffer (pH 7.4) containing 100 mM NaCl and 1% DMSO at the concentration of 30 μM for absorption measurement or in 100 mM HEPES-NaOH buffer (pH 7.4) containing 1% DMSO at 100 μM for the HPLC experiment. The samples were irradiated with various light wavelengths (5.0 mW cm^{-2}) at 25 °C before the experiment, excepting the time-dependent absorption measurement. The absorption spectrum of *Z*-azoMTX was estimated by subtracting the absorbance of the remaining fraction of *E*-azoMTX, which was determined by HPLC analyses (Figure 2-6 and Table 1), from those of the various PSSs. For the time-dependent absorption measurement, the sample was irradiated from the top in the UV/vis spectrometer sample chamber, and the acquisition of absorbance at 350 nm was continued under light irradiation (6.0 mW cm^{-2}). For the thermal relaxation experiment, the sample absorbance at 350 nm was recorded at 25 °C under dark conditions after illumination at 394/10 nm light (5 min, 5.0 mW cm^{-2}).

Binding assay

Competitive binding assays for MTX, azoMTX at dark state, and azoMTX at PSS_{394} toward eDHFR were carried out using eDHFR (2 nM) bound with MTX-Fl (2 nM) in 100 mM HEPES-NaOH buffer (pH 7.4) containing 100 mM NaCl at 25 °C. AzoMTX at PSS_{394} was irradiated with 394/10 nm light at 5.0 mW cm^{-2} for 5 min just before the assay. The IC_{50} values were determined from the plot using nonlinear least-squares analysis.

Optical control of eDHFR activity with azoMTX

Determination of initial enzyme reaction rate

The photo-regulation of the eDHFR activity with azoMTX was evaluated from the enzyme reaction rate. The reaction rate under excess amounts of dihydrofolate and NADPH was determined by monitoring the decrease in NADPH absorbance at 340 nm (ε_{340} = 13.2 mM^{-1} cm^{-1}). eDHFR (10 nM) was pre-incubated with 60 μM NADPH (and 50 nM inhibitor) at 25 °C in 100 mM HEPES-NaOH buffer (pH 7.4) containing 100 mM NaCl. The measurement was started 30 s after the reaction was initiated upon addition of 50 μM dihydrofolate at 25 °C. AzoMTX at various PSSs was irradiated with 330/10, 365/10, 394/10, 450/10, 488/10, 515/10, or 560/10 nm (5.0 mW cm^{-2}) before measurements. The initial rates of the enzyme reaction (v_0) were determined using the following equation,

$$v_0 = |A_{340,30s} - A_{340,0s}| / [(30/60) \times (13.2 \times 10^{-3})] \ (\mu M\ min^{-1})$$

, where $A_{340,30s}$ is the absorbance at 340 nm after 30 s from the measurement start, and $A_{340,0s}$ is the absorbance at 340 nm just after the start.

Reversible photo-regulation of enzyme reaction

AzoMTX (100 nM) were mixed with 90 μM NADPH and 75 μM dihydrofolate in 100 mM HEPES-NaOH buffer (pH 7.4) containing 100 mM NaCl and pre-incubated at 25 °C. The measurement was started 45 s after the enzyme reaction was initiated, upon addition of 5 nM eDHFR, and the reaction sample was repeatedly irradiated with 394/10 or 515/10 nm wavelength light.

^{1}H and ^{13}C NMR spectra

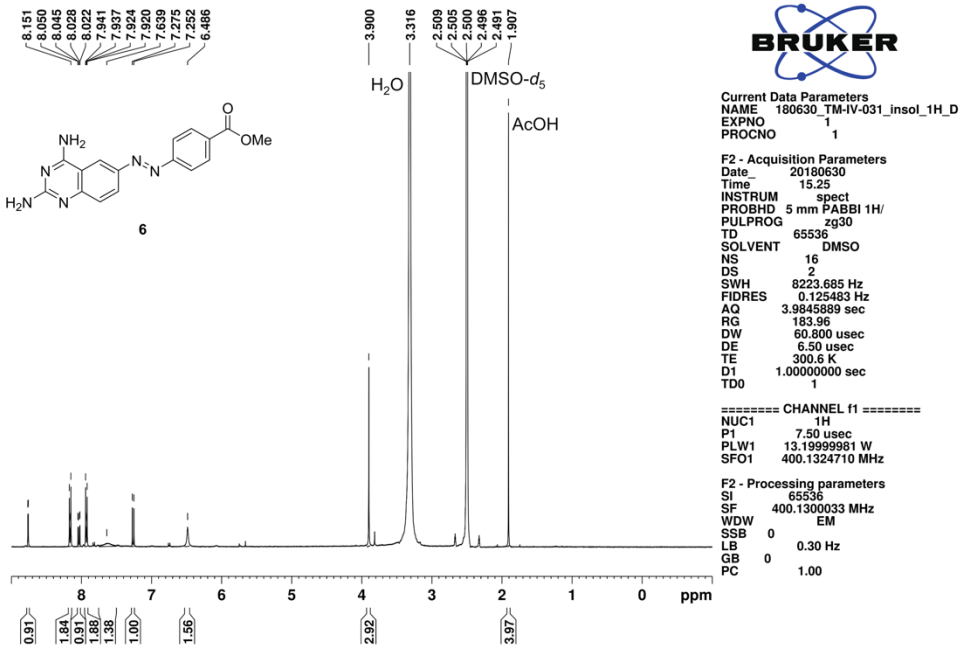

Figure S2-1. ^{1}H NMR spectrum of compound **6** (400 MHz, DMSO-d_6).

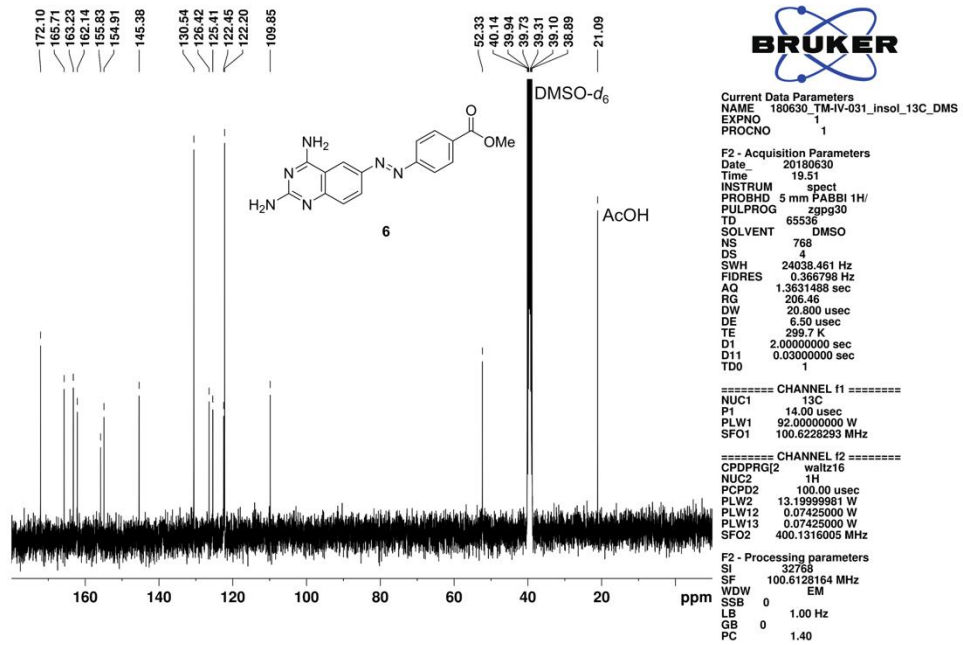

Figure S2-2. ^{13}C NMR spectrum of compound **6** (101 MHz, DMSO-d_6).

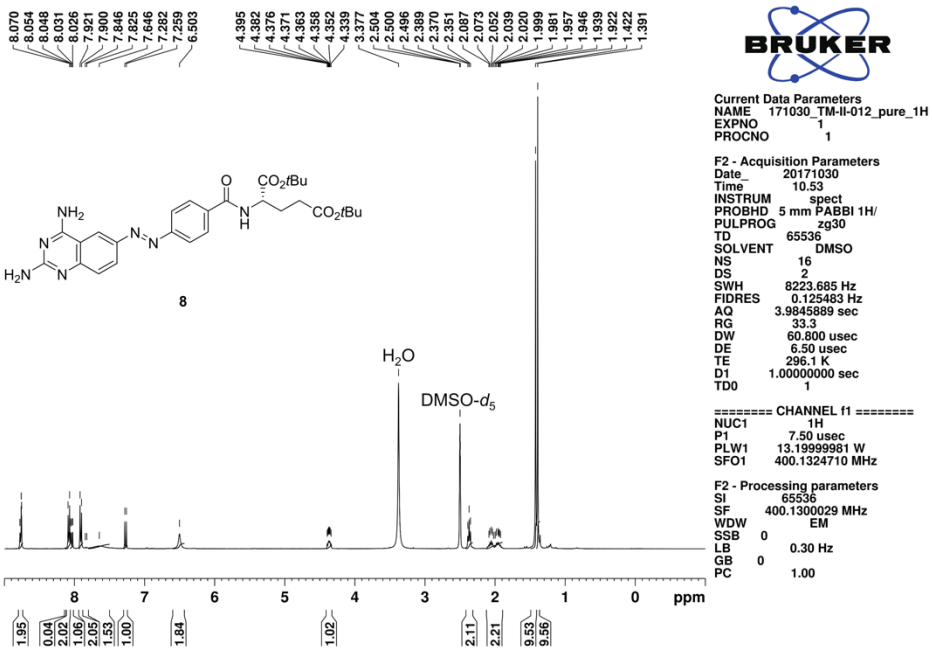

Figure S2-3. ^{1}H NMR spectrum of compound **8** (400 MHz, DMSO-d_6).

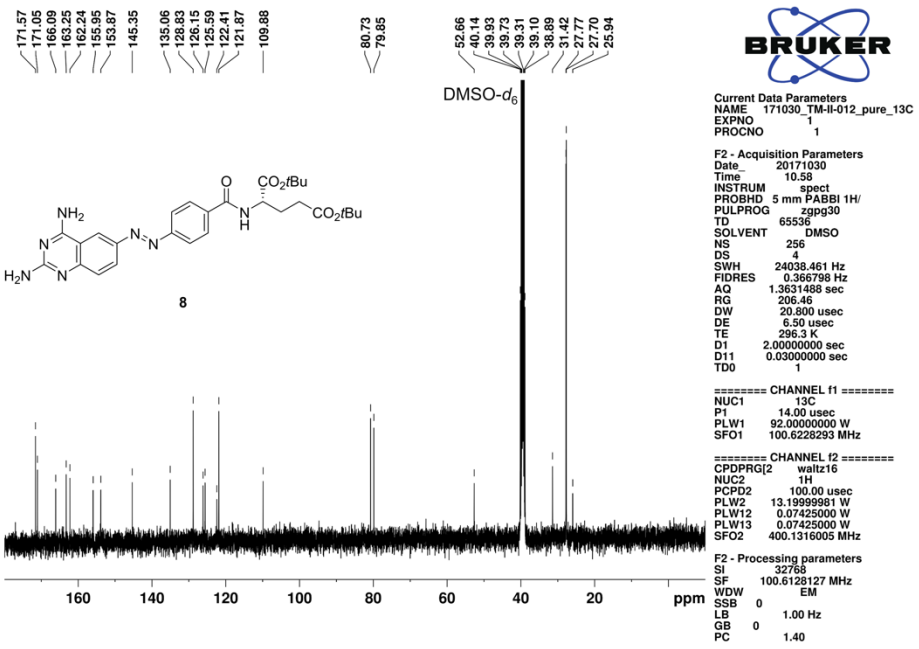

Figure S2-4. ^{13}C NMR spectrum of compound **8** (101 MHz, DMSO-d_6).

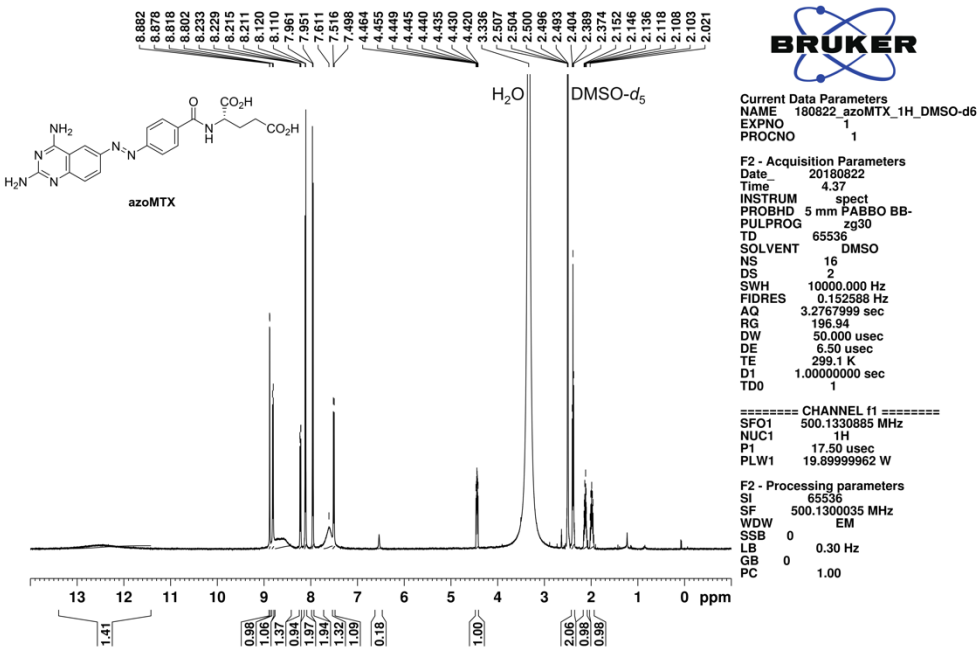

Figure S2-5. ^{1}H NMR spectrum of compound azoMTX (500 MHz, DMSO-d_6).

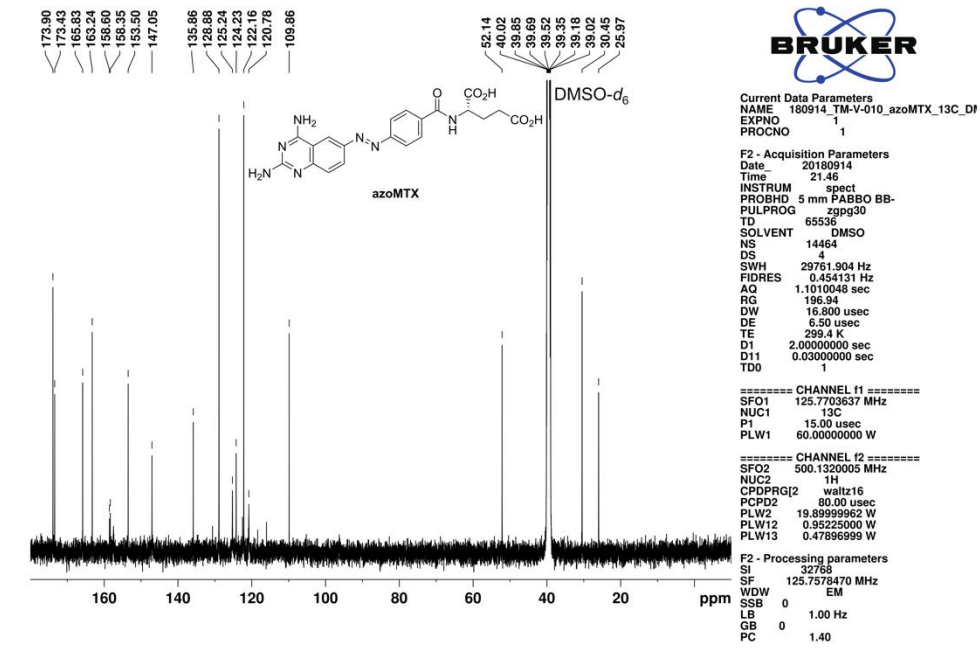

Figure S2-6. ^{13}C NMR spectrum of compound azoMTX (126 MHz, DMSO-d_6).

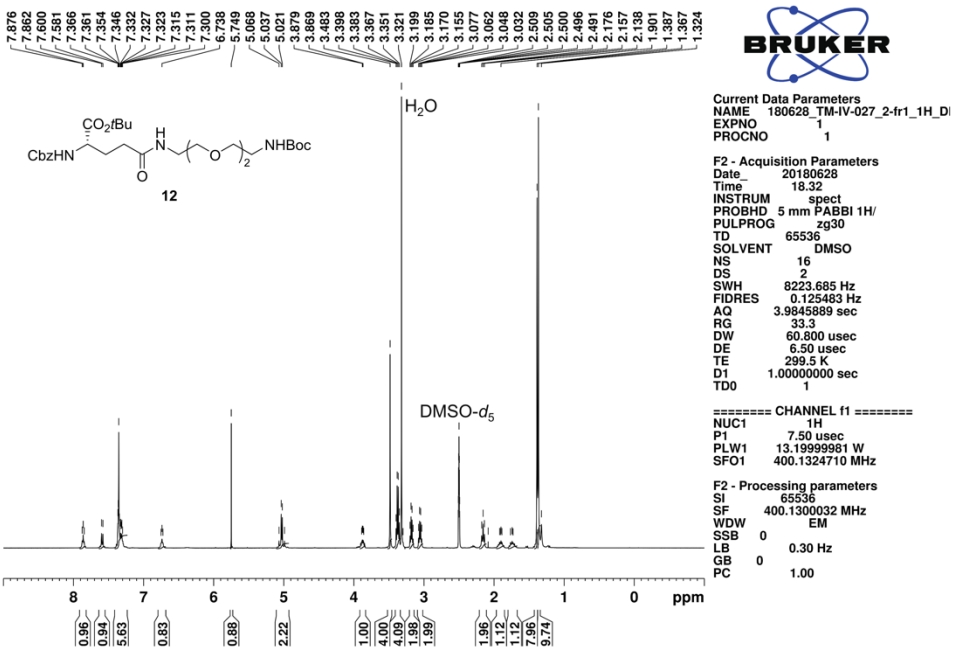

Figure S2-7. ^{1}H NMR spectrum of compound **12** (400 MHz, DMSO-d_6).

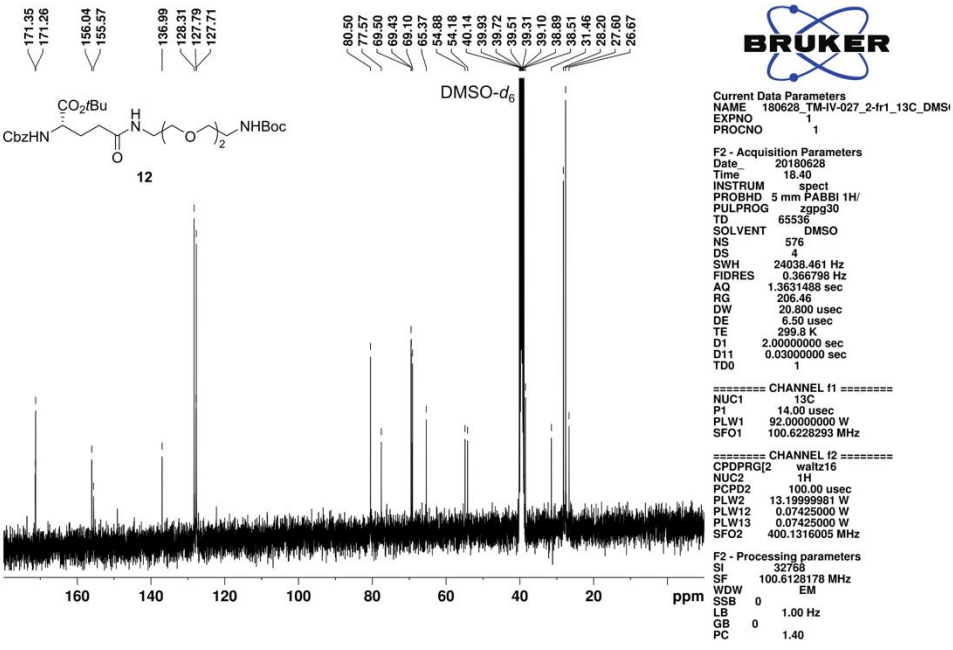

Figure S2-8. ^{13}C NMR spectrum of compound **12** (101 MHz, DMSO-d_6).

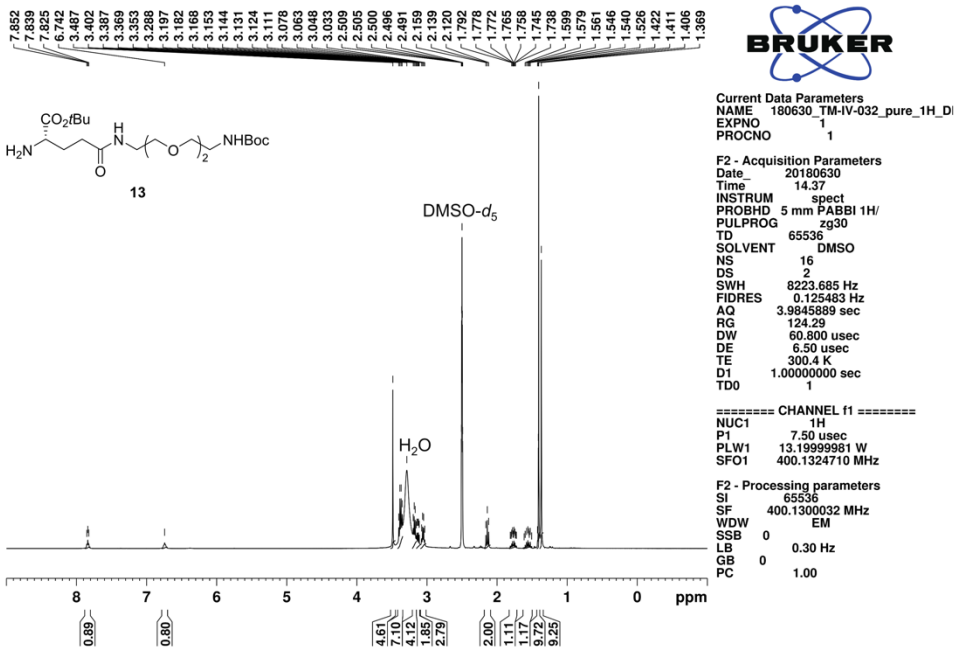

Figure S2-9. ^{1}H NMR spectrum of compound **13** (400 MHz, DMSO-d_6).

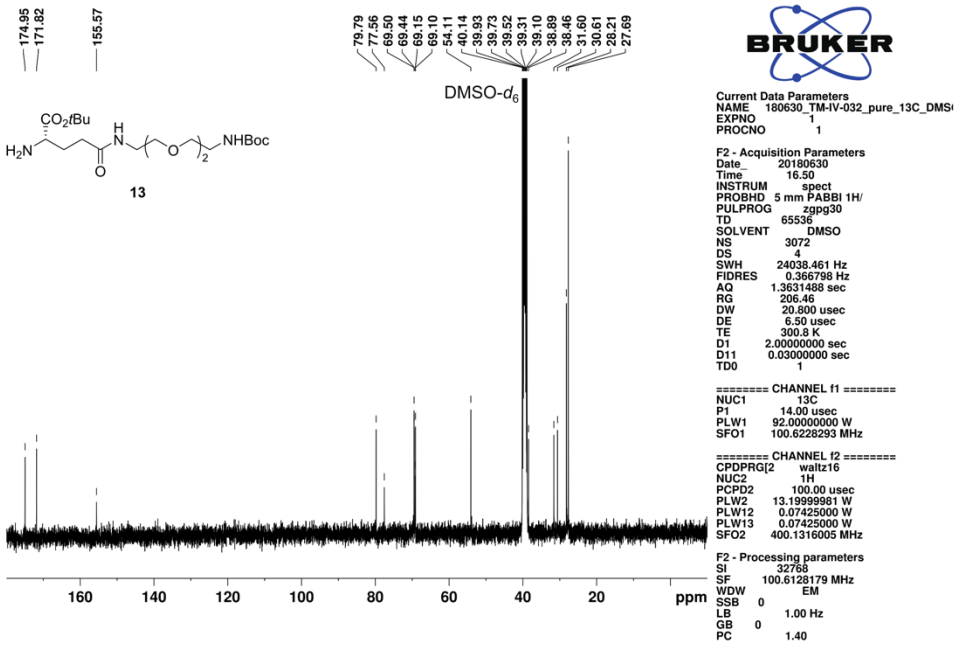

Figure S2-10. ^{13}C NMR spectrum of compound **13** (101 MHz, DMSO-d_6).

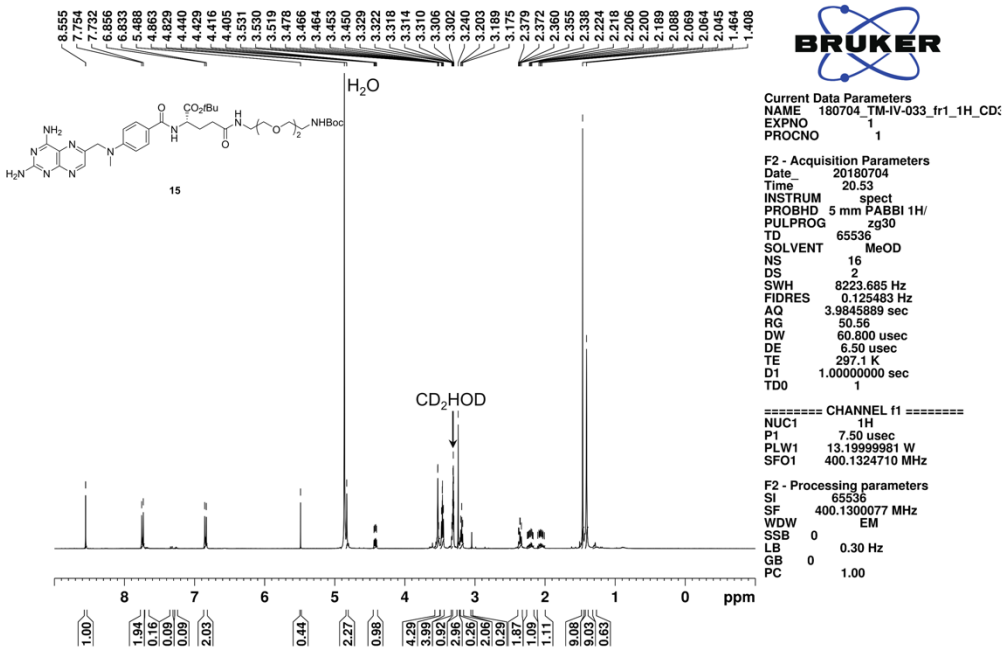

Figure S2-11. ^{1}H NMR spectrum of compound **15** (400 MHz, CD_3OD).

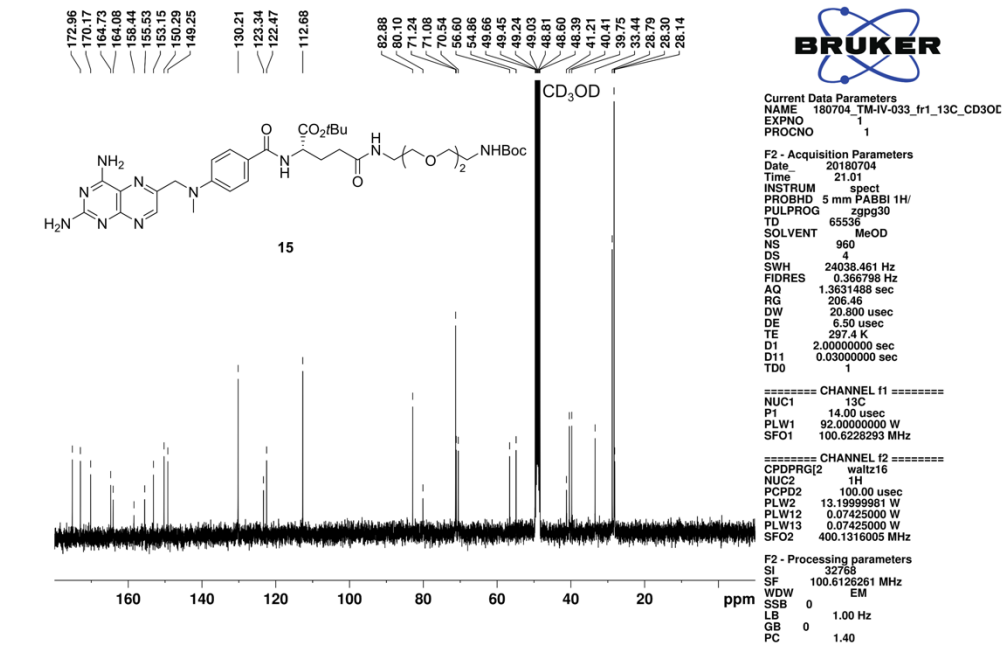

Figure S2-12. ^{13}C NMR spectrum of compound **15** (101 MHz, CD_3OD).

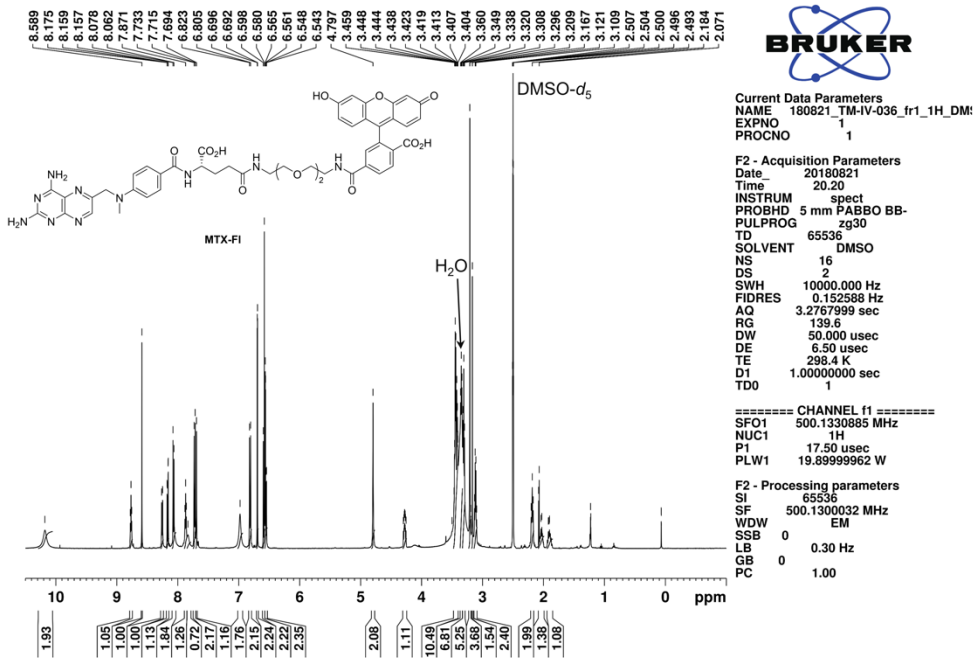

Figure S2-13. ^{1}H NMR spectrum of compound MTX-Fl (500 MHz, DMSO-d_6).

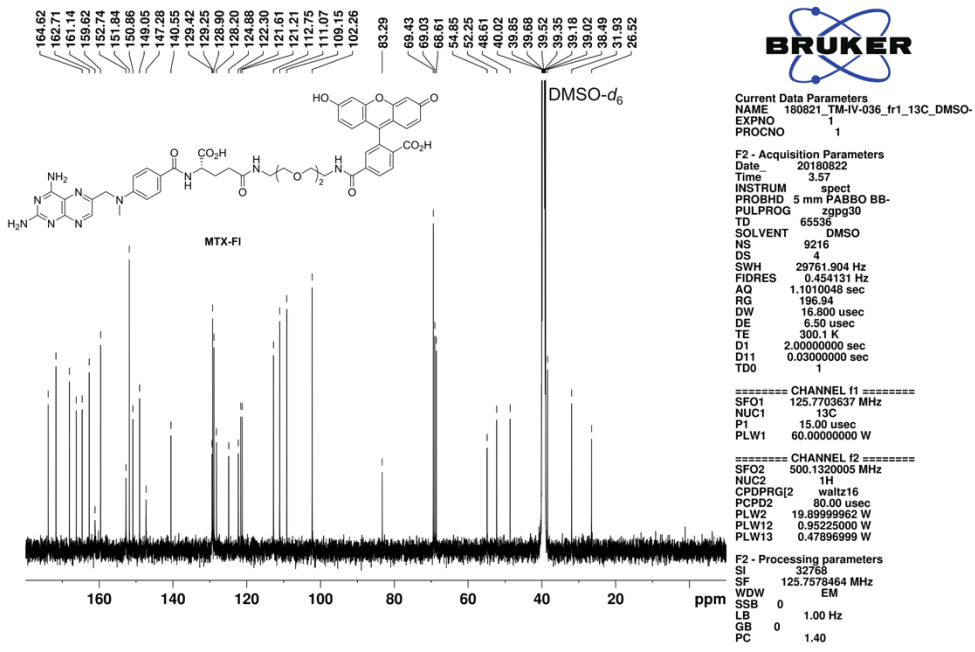

Figure S2-14. ^{13}C NMR spectrum of compound MTX-Fl (126 MHz, DMSO-d_6).

2-7. References (chapter 2)

1. Brieke, C.; Rohrbach, F.; Gottschalk, A.; Mayer, G.; Heckel, A., Light-Controlled Tools. *Angew. Chem. Int. Ed.* **2012,** *51* (34), 8446–8476.

2. Fenno, L.; Yizhar, O.; Deisseroth, K., The Development and Application of Optogenetics. *Annu. Rev. Neurosci.* **2011,** *34* (1), 389–412.

3. Ellis-Davies, G. C. R., Caged compounds: photorelease technology for control of cellular chemistry and physiology. *Nat. Methods* **2007,** *4* (8), 619–628.

4. Hansen, M. J.; Velema, W. A.; Lerch, M. M.; Szymanski, W.; Feringa, B. L., Wavelength-selective cleavage of photoprotecting groups: strategies and applications in dynamic systems. *Chem. Soc. Rev.* **2015,** *44* (11), 3358–3377.

5. Nagel, G.; Szellas, T.; Huhn, W.; Kateriya, S.; Adeishvili, N.; Berthold, P.; Ollig, D.; Hegemann, P.; Bamberg, E., Channelrhodopsin-2, a directly light-gated cation-selective membrane channel. *Proc. Natl. Acad. Sci. USA* **2003,** *100* (24), 13940–13945.

6. Szymański, W.; Beierle, J. M.; Kistemaker, H. A. V.; Velema, W. A.; Feringa, B. L., Reversible Photocontrol of Biological Systems by the Incorporation of Molecular Photoswitches. *Chem. Rev.* **2013,** *113* (8), 6114–6178.

7. Irie, M.; Fukaminato, T.; Matsuda, K.; Kobatake, S., Photochromism of Diarylethene Molecules and Crystals: Memories, Switches, and Actuators. *Chem. Rev.* **2014,** *114* (24), 12174–12277.

8. Hüll, K.; Morstein, J.; Trauner, D., In Vivo Photopharmacology. *Chem. Rev.* **2018,** *118* (21), 10710–10747.

9. Lerch, M. M.; Hansen, M. J.; van Dam, G. M.; Szymanski, W.; Feringa, B. L., Emerging Targets in Photopharmacology. *Angew. Chem. Int. Ed.* **2016,** *55* (37), 10978–10999.

10. Velema, W. A.; Szymanski, W.; Feringa, B. L., Photopharmacology: Beyond Proof of Principle. *J. Am. Chem. Soc.* **2014,** *136* (6), 2178–2191.

11. Broichhagen, J.; Frank, J. A.; Trauner, D., A Roadmap to Success in Photopharmacology. *Acc. Chem. Res.* **2015,** *48* (7), 1947–1960.

12. Stein, M.; Middendorp, S. J.; Carta, V.; Pejo, E.; Raines, D. E.; Forman, S. A.; Sigel, E.; Trauner, D., Azo-Propofols: Photochromic Potentiators of GABAA Receptors. *Angew. Chem. Int. Ed.* **2012,** *51* (42), 10500–10504.

13. Velema, W. A.; van der Berg, J. P.; Hansen, M. J.; Szymanski, W.; Driessen, A. J. M.; Feringa, B. L., Optical control of antibacterial activity. *Nat. Chem.* **2013,** *5* (11), 924–928.

14. Broichhagen, J.; Jurastow, I.; Iwan, K.; Kummer, W.; Trauner, D., Optical Control of Acetylcholinesterase with a Tacrine Switch. *Angew. Chem. Int. Ed.* **2014,** *53* (29), 7657–7660.

15. Wegener, M.; Hansen, M. J.; Driessen, A. J. M.; Szymanski, W.; Feringa, B. L., Photocontrol of Antibacterial Activity: Shifting from UV to Red Light Activation. *J. Am. Chem. Soc.* **2017,** *139* (49), 17979–17986.

16. Ferreira, R.; Nilsson, J. R.; Solano, C.; Andréasson, J.; Grøtli, M., Design, Synthesis and Inhibitory Activity of Photoswitchable RET Kinase Inhibitors. *Sci. Rep.* **2015,** *5* (1), 9769.

17. Engdahl, A. J.; Torres, E. A.; Lock, S. E.; Engdahl, T. B.; Mertz, P. S.; Streu, C. N., Synthesis, Characterization, and Bioactivity of the Photoisomerizable Tubulin Polymerization Inhibitor azo-Combretastatin A4. *Org. Lett.* **2015,** *17* (18), 4546–4549.
18. Borowiak, M.; Nahaboo, W.; Reynders, M.; Nekolla, K.; Jalinot, P.; Hasserodt, J.; Rehberg, M.; Delattre, M.; Zahler, S.; Vollmar, A.; Trauner, D.; Thorn-Seshold, O., Photoswitchable Inhibitors of Microtubule Dynamics Optically Control Mitosis and Cell Death. *Cell* **2015,** *162* (2), 403–411.
19. Schoenberger, M.; Damijonaitis, A.; Zhang, Z.; Nagel, D.; Trauner, D., Development of a New Photochromic Ion Channel Blocker via Azologization of Fomocaine. *ACS Chem. Neurosci.* **2014,** *5* (7), 514–518.
20. Pittolo, S.; Gómez-Santacana, X.; Eckelt, K.; Rovira, X.; Dalton, J.; Goudet, C.; Pin, J.-P.; Llobet, A.; Giraldo, J.; Llebaria, A.; Gorostiza, P., An allosteric modulator to control endogenous G protein-coupled receptors with light. *Nat. Chem. Biol.* **2014,** *10* (10), 813–815.
21. Kwon, Y. K.; Higgins, M. B.; Rabinowitz, J. D., Antifolate-Induced Depletion of Intracellular Glycine and Purines Inhibits Thymineless Death in E. coli. *ACS Chem. Biol.* **2010,** *5* (8), 787–795.
22. Miller, L. W.; Cai, Y.; Sheetz, M. P.; Cornish, V. W., In vivo protein labeling with trimethoprim conjugates: a flexible chemical tag. *Nat. Methods* **2005,** *2* (4), 255–257.
23. Miller, L. W.; Sable, J.; Goelet, P.; Sheetz, M. P.; Cornish, V. W., Methotrexate Conjugates: A Molecular In Vivo Protein Tag. *Angew. Chem. Int. Ed.* **2004,** *43* (13), 1672–1675.
24. Hynes, J. B.; Harmon, S. J.; Floyd, G. G.; Farrington, M.; Hart, L. D.; Gale, G. R.; Washtien, W. L.; Susten, S. S.; Freisheim, J. H., Chemistry and antitumor evaluation of selected classical 2,4-diaminoquinazoline analogs of folic acid. *J. Med. Chem.* **1985,** *28* (2), 209–215.
25. Chen, X.; Wu, Y.-W., Tunable and Photoswitchable Chemically Induced Dimerization for Chemo-optogenetic Control of Protein and Organelle Positioning. *Angew. Chem. Int. Ed.* **2018,** *57* (23), 6796–6799.
26. Aonbangkhen, C.; Zhang, H.; Wu, D. Z.; Lampson, M. A.; Chenoweth, D. M., Reversible Control of Protein Localization in Living Cells Using a Photocaged-Photocleavable Chemical Dimerizer. *J. Am. Chem. Soc.* **2018,** *140* (38), 11926–11930.
27. Zhang, H.; Aonbangkhen, C.; Tarasovetc, E. V.; Ballister, E. R.; Chenoweth, D. M.; Lampson, M. A., Optogenetic control of kinetochore function. *Nat. Chem. Biol.* **2017,** *13* (10), 1096–1101.
28. Ballister, E. R.; Aonbangkhen, C.; Mayo, A. M.; Lampson, M. A.; Chenoweth, D. M., Localized light-induced protein dimerization in living cells using a photocaged dimerizer. *Nat. Commun.* **2014,** *5* (1), 5475.
29. Matera, C.; Gomila, A. M. J.; Camarero, N.; Libergoli, M.; Soler, C.; Gorostiza, P., Photoswitchable Antimetabolite for Targeted Photoactivated Chemotherapy. *J. Am. Chem. Soc.* **2018,** *140* (46), 15764–15773.
30. Burchall, J. J.; Hitchings, G. H., Inhibitor binding analysis of dihydrofolate reductases from various species. *Mol. Pharmacol.* **1965,** *1* (2), 126–36.
31. Mendoza-Martínez, C.; Correa-Basurto, J.; Nieto-Meneses, R.; Márquez-Navarro, A.; Aguilar-Suárez,

R.; Montero-Cortes, M. D.; Nogueda-Torres, B.; Suárez-Contreras, E.; Galindo-Sevilla, N.; Rojas-Rojas, Á.; Rodriguez-Lezama, A.; Hernández-Luis, F., Design, synthesis and biological evaluation of quinazoline derivatives as anti-trypanosomatid and anti-plasmodial agents. *Eur. J. Med. Chem.* **2015,** *96*, 296–307.

32. Tomašić, T.; Zidar, N.; Rupnik, V.; Kovač, A.; Blanot, D.; Gobec, S.; Kikelj, D.; Mašič, L. P., Synthesis and biological evaluation of new glutamic acid-based inhibitors of MurD ligase. *Bioorg. Med. Chem. Lett.* **2009,** *19* (1), 153–157.

33. Priewisch, B.; Rück-Braun, K., Efficient Preparation of Nitrosoarenes for the Synthesis of Azobenzenes. *J. Org. Chem.* **2005,** *70* (6), 2350–2352.

34. Otremba, T.; Ravoo, B. J., Dynamic multivalent interaction of phenylboronic acid functionalized dendrimers with vesicles. *Tetrahedron* **2017,** *73* (33), 4972–4978.

35. Terai, T.; Kohno, M.; Boncompain, G.; Sugiyama, S.; Saito, N.; Fujikake, R.; Ueno, T.; Komatsu, T.; Hanaoka, K.; Okabe, T.; Urano, Y.; Perez, F.; Nagano, T., Artificial Ligands of Streptavidin (ALiS): Discovery, Characterization, and Application for Reversible Control of Intracellular Protein Transport. *J. Am. Chem. Soc.* **2015,** *137* (33), 10464–10467.

36. Blommel, P. G.; Fox, B. G., A combined approach to improving large-scale production of tobacco etch virus protease. *Protein Expr. Purif.* **2007,** *55* (1), 53–68.

37. Miller, G. P.; Benkovic, S. J., Deletion of a Highly Motional Residue Affects Formation of the Michaelis Complex for Escherichia coli Dihydrofolate Reductase. *Biochemistry* **1998,** *37* (18), 6327–6335.

CHAPTER 3

Protein Dimerization System that Allows Photo-reversible Control of Protein Localization in a Live Cell

3-1. Introduction

Cellular events are spatiotemporally regulated by the dynamics of various biomolecules, such as protein-protein interaction or protein translocation.[1, 2] Therefore, artificial regulation of these dynamics with precision in time and space offers valuable insight on causality between biomolecular dynamics and cellular processes.[3, 4] Chemical and optogenetic tools have been reported as versatile methods that provide exquisite control of biomolecular dynamics.[5] Optogenetic tools employ photo-responsive proteins whose conformations are changed upon illumination.[6-10] These tools have allowed reversible induction of protein association or dimerization dependent on light, achieving light-dependent regulation of diverse cellular processes within a few seconds. Moreover, several biological questions that have been difficult or impossible to be addressed with other tools have been solved with optogenetic tools that dynamically manipulate protein localization with high precision in space and time.[11-13] However, most optogenetic tools are faced with a couple of problems, such as activation wavelength overlapping with fluorescent proteins,[14, 15] slow turn-off kinetics,[16] and small dynamic range.[17]

Alternative tools are chemically induced dimerization (CID) systems furnished by chemical dimerizers. CID systems use small molecules interacting with two proteins to induce the dimerization or association.[18, 19] Over a couple of decades, photo-activatable or photo-cleavable CID systems have been reported and attracted attention as new chemical tools for the precise regulation of protein dynamics.[20-22] Among several photo-responsive CID systems, non-diffusible systems through a covalent bond to one protein are superior to diffusible ones because of high spatial precision.[23-25] In these non-diffusible systems, one ligand forms a covalent bond with the corresponding protein to suppress diffusion of a chemical dimerizer, and the photolabile group is attached on the other ligand or between ligands. Furthermore, using two different photolabile groups in a chemical dimerizer, both-directional control of protein localization and diffusion was also achieved for one-time use.[26, 27] Using these photo-responsive CID systems as chemical-biology tools, the molecular mechanisms of various cellular events have been revealed.[28, 29] Although the photo-responsive CID systems have provided exquisite control in time and space, they cannot be switched on and off repetitively upon light, unlike optogenetic tools.

Herein, the author presents a novel photochromic CID system capable of repetitive switching on and off upon light. Azobenzene analog was employed for a photo-responsive group, and photoisomerization of the ligand altered the affinity to the corresponding protein. Repetition of dimerization was evaluated in cells by induction of protein translocation to various organelles, and

quick and reversible control of protein translocation was feasible. Finally, the photochromic CID system was applied to optical regulation of autophagy-mediated degradation of mitochondria. In summary, the photochromic CID allows a cycle of both-directional control of protein localization and diffusion dependent on light with fast kinetics, facilitating precise control of intracellular protein dynamics to ravel unsolved biological questions.

3-2. Design and characterization of photo-switchable dimerizer

In chapter 2, the author has developed a photo-reversible ligand, azoMTX, which binds to eDHFR in a photo-reversible manner. Violet light irradiation, typically at 394 nm, isomerized azoMTX from *E* isomer to *Z* isomer, whereas green light, typically at 560 nm, induces the reverse isomerization from *Z* to *E*. Since (*Z*)-azoMTX had a higher affinity to eDHFR than *E* isomer, azoMTX was associated with and dissociated from eDHFR repeatedly by alternating irradiation with different wavelengths of light. Accordingly, the author designed the photochromic eDHFR ligand (pcDL) conjugated with a HaloTag ligand (pcDH) to establish a photochromic CID system (Figure 3-1a). In this system, while pDL binds to eDHFR photo-reversibly, the HaloTag ligand makes a covalent bond to HaloTag protein, a mutant bacterial haloalkane dehalogenase specifically forms a covalent bond with a chloroalkane derivative.[30] Initially, the HaloTag ligand moiety of pcDH is labeled to HaloTag-fused protein, while the binding between pDL and eDHFR is suppressed because of the lower affinity. UV light irradiation causes *E*-to-*Z* isomerization of pDL and enhances the affinity to eDHFR to induce dimerization. However, green light irradiation inversely isomerizes pDL from *Z* to *E* and reduces affinity to eDHFR, leading to dissociation of protein dimer (Figure 3-1b). Notably, one of the carboxy groups on azoMTX was removed to design pcDH with higher cell membrane permeability.

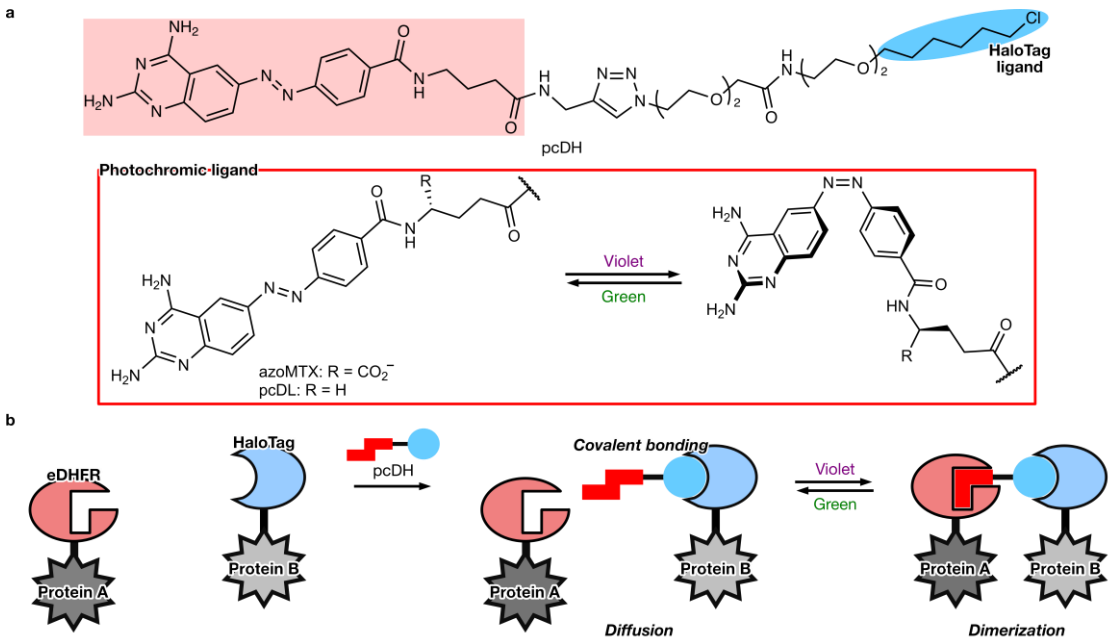

Figure 3-1. Design of pcDH. **a**) Chemical structure of the photoisomerizable dimerizer, pcDH. **b**) Schematic illustration of photochromism-based protein translocation.

Scheme 3-1. Synthetic route to pcDH

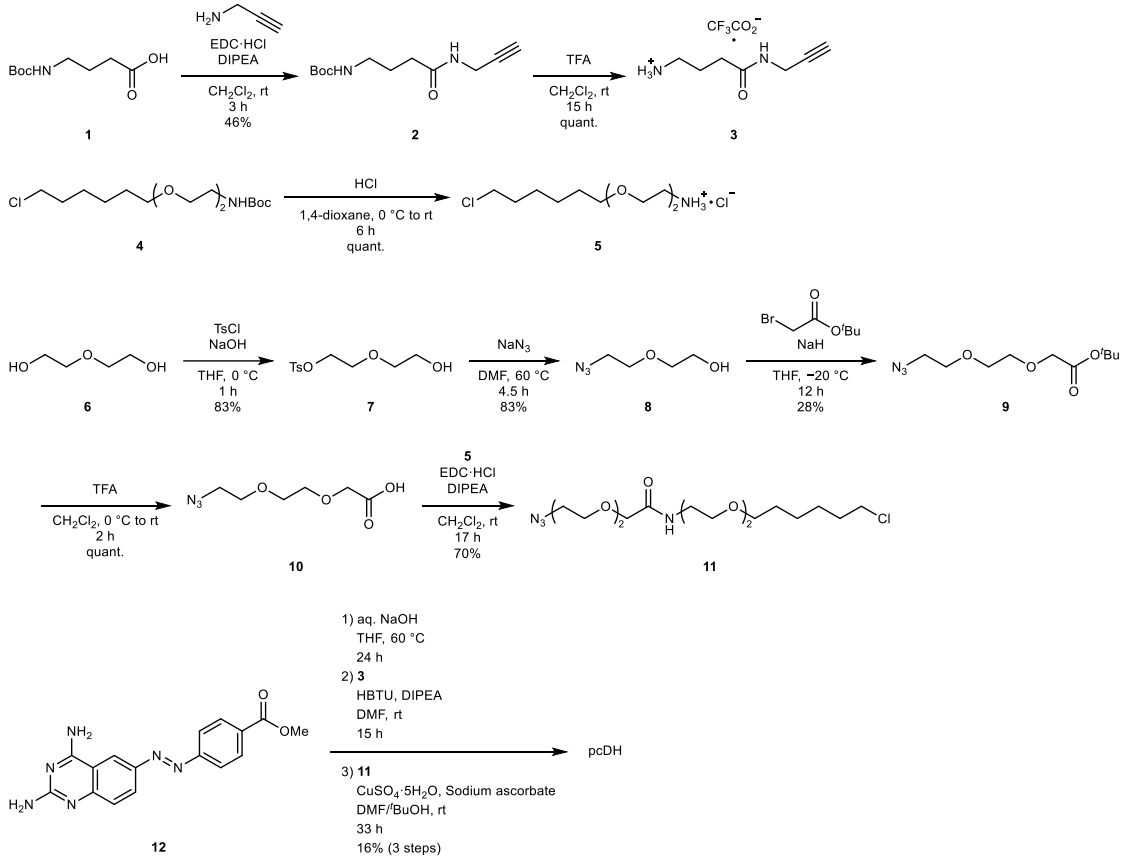

Based on the abovementioned strategy, pcDH was synthesized (Scheme 3-1), and the photophysical property was studied in an aqueous solution. Irradiation of 394-nm and 560-nm light induced *E*-to-*Z* and *Z*-to-*E* isomerization, respectively (Figure 3-2a). The photoisomerization of pcDH was repeatedly achieved by alternating light at 394 and 560 nm (Figure 3-2b). In addition, the fraction of *E* and *Z* isomer at the photostationary state was varied according to the irradiation wavelength (82% *Z* isomer at 394 nm, 11% *Z* isomer at 560 nm) (Figure 3-2c). The binding assay results indicated that pcDH under 394-nm irradiation had a three times higher affinity to eDHFR than dark conditions ($K_{d,Dark}$ = 0.26 ± 0.04 μM, $K_{d,394\text{-}nm}$ = 0.097 ± 0.015 μM, mean ± s.d., n = 4; Figure 3-2d). These properties agreed well with the results of azoMTX in chapter 2.

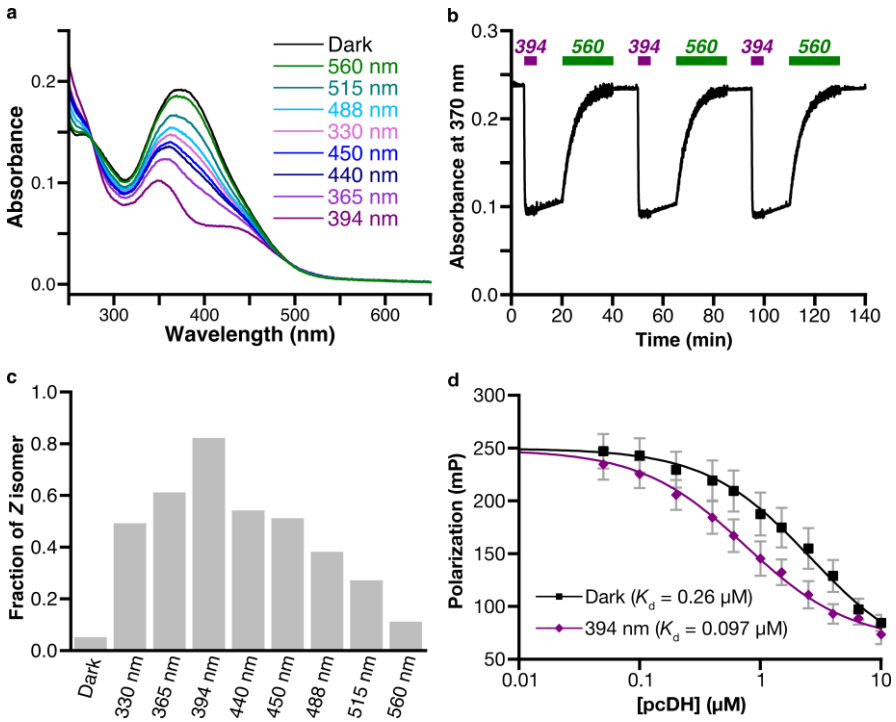

Figure 3-2. Characterization of pcDH. **a**) Absorption spectra of a photochromic dimerizer, pcDH, at the thermal equilibrium state and the various photostatinary states. pcDH (20 μM) was dissolved in 100 mM HEPES-NaOH buffer (pH 7.4) containing 100 mM NaCl and 1% DMSO. The solution of pcDH was incubated at 37 °C for 1 h under dark condition (Dark) or was irradiated at various light wavelengths (5.0 mW cm^{-2}) for 5 min (330, 365, 394, 440, 450, 488, and 515 nm), or 15 min (560 nm) before measurement at 37 °C. **b**) Time course of absorption changes at 370 nm under alternating light irradiation. Light intensity was set to 5.0 mW cm^{-2} for each wavelength. **c**) Fractions of *Z* isomer of pDLH at the various photostationary states, determined by HPLC analyses. **d**) Competitive binding assay of pcDH and eDHFR using fluorescence polarization. pcDH under 394-nm was irradiated with violet light (394/10 nm, 5.0 mW cm^{-2}) for 5 min before the measurement. R^2 value was >0.99. Data shown are mean ± s.d. (n = 4).

3-3. Photo-reversible protein translocation using pcDH

Having confirmed that the affinity of pcDH to eDHFR can be modulated upon light irradiation, the author next tried to control subcellular protein translocation using pcDH. HeLa cells were transfected with two plasmids that express eDHFR-fused miRFP670nano with an NES sequence at the C-terminus (eDHFR-miRFP670nano-NES) and HaloTag-fused mOrange2 with a CAAX sequence at the C-terminus (Halo-mOrange2-CAAX) targeting the cytosolic interface of the plasma membrane. After incubating the cells with pcDH for 1 h, the time-lapse images were acquired by spinning-disk confocal fluorescence microscopy. Before light irradiation, eDHFR-miRFP670nano-NES diffused in the cytosol. Then, violet light irradiation quickly induced the translocation of eDHFR-miRFP670nano-NES to the plasma membrane, where Halo-mOrange2-CAAX was localized (Figure 3-3a). Subsequently, green light irradiation quickly diffused eDHFR-miRFP670nano-NES to the cytosol again. This recruitment of eDHFR-miRFP670nano-NES to the plasma membrane was reversible and repeatable (Figure 3-3b). Contrariwise, in the absence of pcDH, no translocation of eDHFR-miRFP670nano-NES was observed upon either violet or green light illumination (Figure 3-3b).

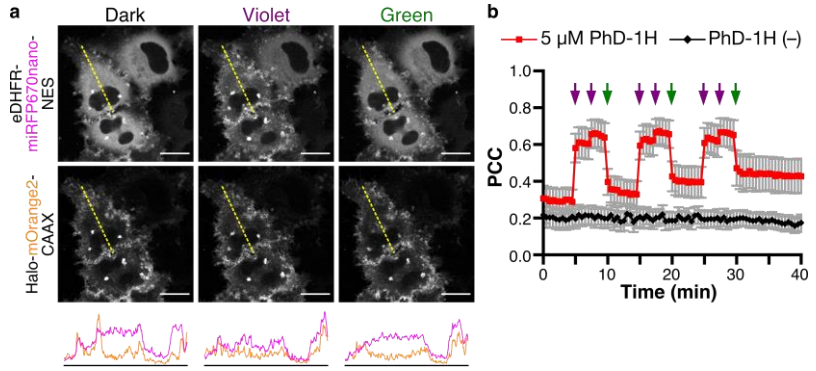

Figure 3-3. Translocation of cytosolic protein to the plasma membrane based on photochromic CID. **a**) Photochromism-inducible recruitment of cytoplasmic proteins to plasma membrane. Confocal fluorescence images of HeLa cells expressing Halo-mOrange2-CAAX and eDHFR-miRFP670nano-NES before and after light illumination with 405 nm (Violet) and 555 nm (Green). **b**) Time course changes of Pearson correlation coefficient (PCC). The arrows indicate light irradiation of 405 nm (violet) and 555 nm (green), respectively. Data shown are mean ± s.e.m., *n* = 9 cells, two independent experiments. Scale bars in all images, 20 μm.

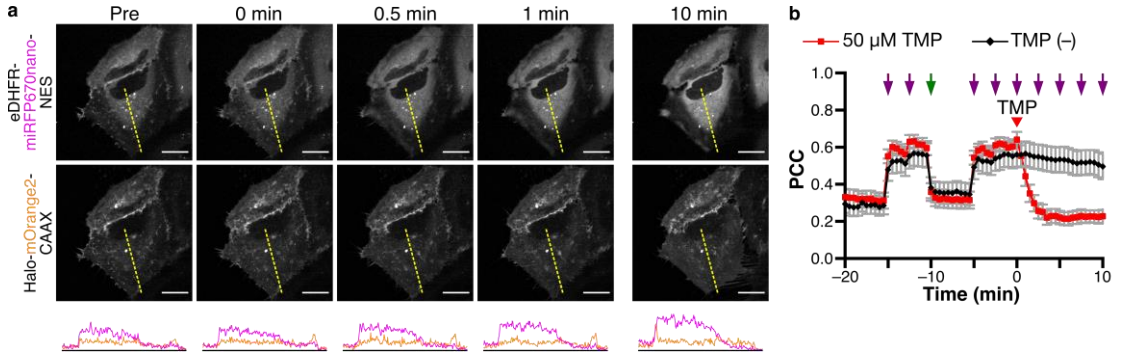

Figure 3-4. Suppression of the recruitment to plasma membrane upon addition of TMP. **a**) Photochromism-inducible recruitment of cytoplasmic proteins to plasma membrane followed by diffusion by the addition of TMP. Confocal fluorescence images of HeLa cells expressing Halo-mOrange2-CAAX and eDHFR-miRFP670nano-NES before and after light illumination with 405 nm (Violet) and 555 nm (Green). **b**) Time course changes of PCC. The arrows indicate light irradiation of 405 nm (violet) and 555 nm (green), respectively. Addition of TMP (final concentration: 50 μM, red triangle) at 0 min diffused eDHFR recruited to the plasma membrane, whose rate was slower than diffusion induced by green light (green arrow at −10 min). Data shown are mean ± s.e.m., *n* = 10 cells, two independent experiments. Scale bars in all images, 20 μm.

Moreover, the addition of an excess amount of trimethoprim (TMP), which selectively binds to eDHFR with a high affinity,[31] suppressed translocation of eDHFR-miRFP670nano-NES (Figure 3-4). These results indicate that the photo-switchable translocation is due to photochromism-based affinity change of pcDH with eDHFR.

To validate the versatility of this photochromic CID system, the author addressed photo-switchable protein translocation to the different intracellular compartments. Halo-mOrange2-NLS, Halo-mOrange2-Cb5, and Tom20-mOrange2-Halo were used for translocation to the nucleus, endoplasmic reticulum (ER), and mitochondrial outer membrane, respectively. In every case, photo-switchable protein translocation was attained (Figure 3-5) as well as the plasma membrane case. Moreover, eDHFR-miRFP670nano-NES rapidly localized to or diffused from ER and mitochondria (Figure 3-

5d,f). Interestingly, in the case of nuclear translocation, both localization and diffusion of eDHFR-miRFP670nano took a longer time than in other cases (Figure 3-5b). This delay is presumably because some barriers such as nuclear pores suppressed protein diffusion.

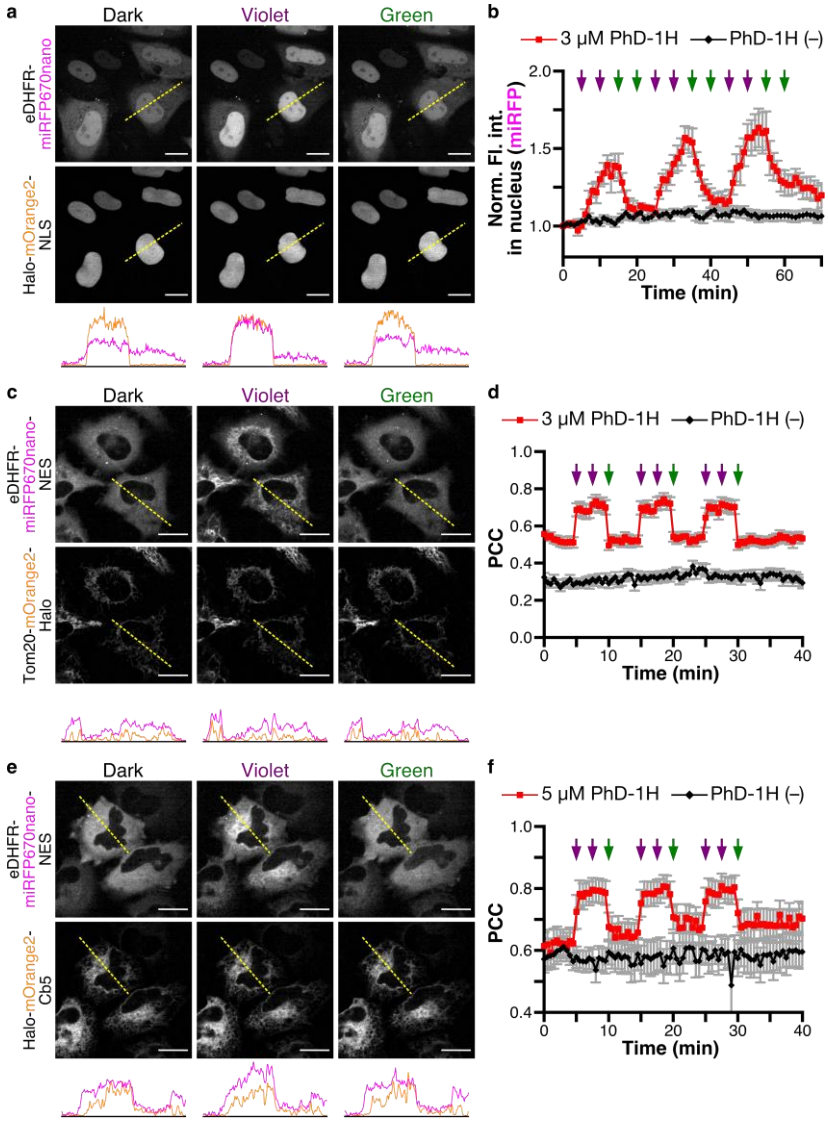

Figure 3-5. Translocation of cytosolic protein to the subcellular compartments. **a**) Photochromism-inducible recruitment of cytoplasmic proteins to nucleus. Confocal fluorescence images of HeLa cells expressing Halo-mOrange2-NLS and eDHFR-miRFP670nano before and after light illumination with 405 nm (Violet) and 555 nm (Green). **b**) Time course changes of average fluorescence intensity in the nucleus. **c**) Photochromism-inducible recruitment of cytoplasmic proteins to mitochondrial outer membrane. Confocal fluorescence images of HeLa cells expressing Tom20-mOrange2-Halo and eDHFR-miRFP670nano-NES before and after light illumination with 405 nm (Violet) and 555 nm (Green). **d**) Time course changes of average PCC. **e**) Photochromism-inducible recruitment of cytoplasmic proteins to ER. Confocal fluorescence images of HeLa cells expressing Halo-mOrange2-Cb5 and eDHFR-miRFP670nano-NES before and after light illumination with 405 nm (Violet) and 555 nm (Green). **f**) Time course changes of average PCC. Data shown are mean ± s.e.m., *n* = 10 cells, two independent experiments. Scale bars in all images, 20 μm.

The author further investigated the kinetics of the rapid protein translocation between the cytoplasm and mitochondrial outer membrane. Kinetic analysis of mitochondria recruitment of eDHFR-miRFP670nano-NES showed rapid induction with a $t_{1/2,on}$ of 0.72 ± 0.08 s when violet light was applied (Figure 3-6). Diffusion kinetics was also estimated at a $t_{1/2,off}$ less than 0.3 s when green light was applied (Figure 3-6). To the author's knowledge, the kinetic properties of this photo-switchable tool using pcDH are faster than or comparable to other photo-reversible tools that employ photo-responsive proteins (Table 3-1),[32] such as CRY2/CIBN[8] ($t_{1/2,on}$ = 3.7 s, $t_{1/2,off}$ = 290 s), iLID[7] ($t_{1/2,on}$ = 1.2 s, $t_{1/2,off}$ = 4 s), Magnets[6] ($t_{1/2,on}$ = 1.4 s, $t_{1/2,off}$ = 15 s), and its derivative eMagnets[33] ($t_{1/2,on}$ = 3.6 s, $t_{1/2,off}$ = 23 s).

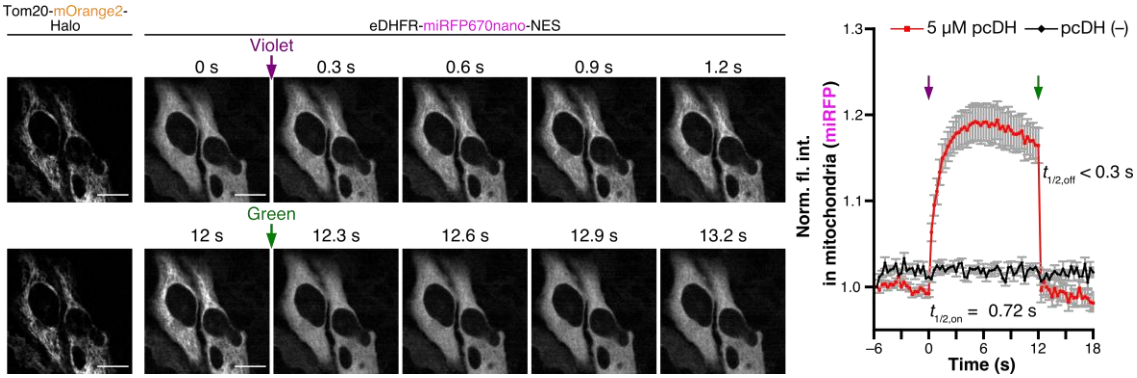

Figure 3-6. Time course of violet light-dependent recruitment of eDHFR-miRFP670nano-NES to the mitochondrial outer membrane and its dissociation to the cytosol induced by green light. Mitochondria localization of Tom20-mOrange2-Halo is shown on the left. The $t_{1/2,on}$ (0.72 ± 0.08 s) was determined using the mono-exponential functions. Data shown are mean ± s.e.m., *n* = 27 cells, two independent experiments. Scale bars in all images, 20 μm.

Table 3-1. The property of photochromic CID system and optogenetic tools

Name		eDHFR/ Halo	CRY2/ CIBN	iLID	Magnet	eMags	PhyB/ PIF
Size (kDa)		18/34	55/19	17	34/51	17/17	99/11
Cofactor		pcDH	FAD	FMN	FAD	FAD	Phycocyanobilin
Wavelength (nm) (ON/OFF)		405/555	488/Dark	488/Dark	488/Dark	488/Dark	650/750
ON/OFF rate	$t_{1/2,on}$ (s)	0.72 ± 0.08	3.7 ± 0.9	1.2 ± 0.3	1.4 ± 0.1	3.6 ± 0.3	1.3 ± 0.5
	$t_{1/2,off}$ (s)	< 0.3	290 ± 30	4 ± 1	15 ±3	23.1 ± 0.6	4 ± 1

3-4. Quantitative regulation of protein recruitment upon light irradiation

In a cell signaling pathway, the dose and frequency of protein recruitment critically affect cellular responses.[13, 34] The photochromic CID system accomplished the quick and repetitive regulation of protein recruitment by violet and green light illumination. Since the proportion of *E* and *Z* isomers of pcDH at the photostationary state is determined by illumination light wavelength, the author assumed the protein recruitment could be quantitatively regulated by illumination wavelength. The author treated HeLa cells transiently expressing eDHFR-miRFP670nano-NES and Halo-mOrange2-CAAX with pcDH followed by violet, blue, and green light illumination. After blue light illumination, HaloTag and eDHFR signals were less colocalized than after violet light illumination (Figure 3-7a,b). The Pearson correlation coefficient (PCC) representing the colocalization of eDHFR with HaloTag after the blue light illumination (PCC = 0.54 ± 0.04; mean ± s.e.m., n = 15 cells) was lower than after violet light illumination (PCC = 0.67 ± 0.03) and higher than after green light illumination (PCC = 0.38 ± 0.05) (Figure 3-7c). A similar variation on the correlation coefficients between the two signals

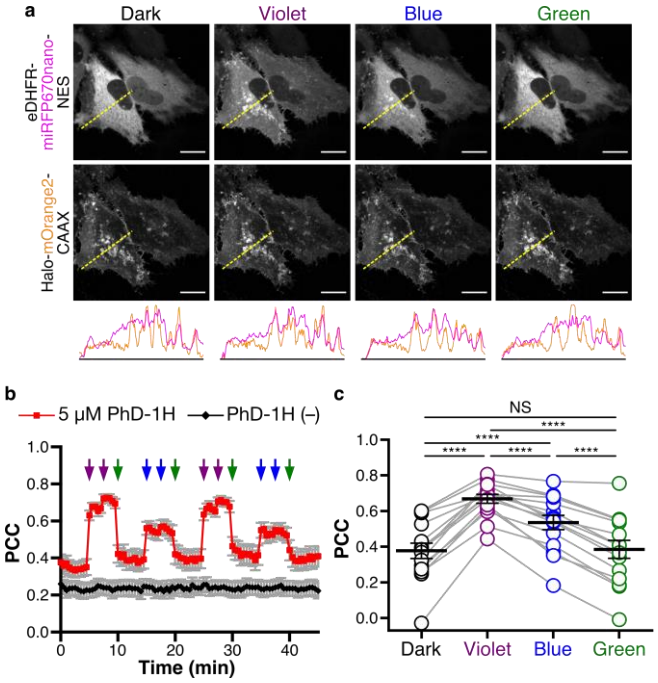

Figure 3-7. Quantitative recruitment of cytosolic protein in a wavelength-dependent manner. **a**) Photochromism-inducible recruitment of cytoplasmic proteins to plasma membrane. Confocal fluorescence images of HeLa cells expressing Halo-mOrange2-CAAX and eDHFR-miRFP670nano-NES before (Dark) and after light illumination with 405 nm (Violet), 555 nm (Green). **b**) Time-course changes of average PCC. The arrows indicate light irradiation of 405 nm (violet), 445 nm (blue), and 555 nm (green), respectively. **c**) Quantification of eDHFR recruitment upon light illumination. Photochromism-inducible recruitment of cytoplasmic proteins to nucleus. Confocal fluorescence images of HeLa cells expressing Halo-mOrange2-NLS and eDHFR-miRFP670nano before and after light illumination with 405 nm (Violet) and 555 nm (Green). Data shown are mean ± s.e.m., Two-tailed paired Student's *t*-test assuming equal variance. ****P < 0.0001 and not significant (NS) for P > 0.05. n = 15 cells, three independent experiments. Scale bars in all images, 20 μm.

was also induced by treating different concentrations of TMP-HTL, a conventional chemical dimerizer of eDHFR and HaloTag (Figure 3-8). These results indicate that the amount of (*Z*)-pcDH with a higher affinity to eDHFR than (*E*)-pcDH plays a dominant role in translocation efficiency and that quantitative protein recruitment was achieved by manipulating (*Z*)-pcDH concentration by illumination wavelength.

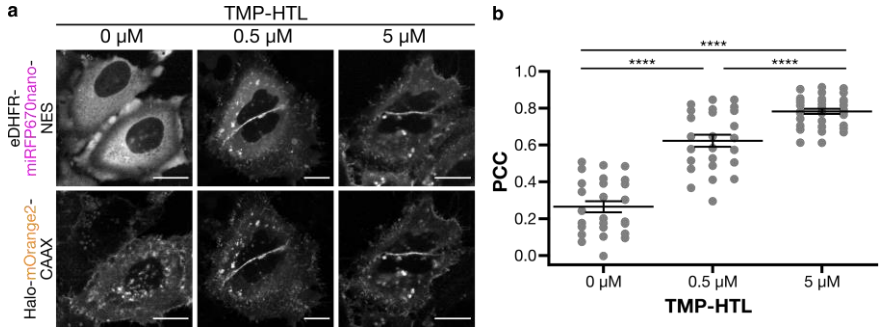

Figure 3-8. Quantitative recruitment of cytosolic protein induced by different concentrations of TMP-HTL. **a**) Recruitment of cytoplasmic proteins to plasma membrane upon conventional chemical dimerizer, TMP-HTL. Confocal fluorescence images of HeLa cells expressing Halo-mOrange2-CAAX and eDHFR-miRFP670nano-NES treated with 0, 0.5, or 5 μM TMP-HTL. **b**) Quantification of eDHFR recruitment upon light illumination. Data shown are mean ± s.e.m., Two-tailed paired Student's t-test without assuming equal variance. ****P < 0.0001; n = 26 (0 μM), 25 (0.5 μM), or 34 (5 μM), respectively; three independent experiments. Scale bars in all images, 20 μm.

3-5. Optical regulation of mitophagy

Lastly, the author applied the photochromic CID system to the manipulation of cellular functions. Autophagy-mediated degradation of mitochondria, termed mitophagy, is an essential intracellular event for maintaining cellular homeostasis. In normal cells, damaged or dysfunctional mitochondria are ubiquitinated and degraded in lysosomes.[35] PINK1/Parkin-mediated pathway plays a crucial role in removing damaged mitochondria among several mechanisms. Damaged mitochondria accumulate PINK1 (PTEN-induced putative kinase 1) on the outer membrane, on which it recruits and activates the E3 ubiquitin ligase Parkin to induce mitophagy dependent on the kinase activity of PINK1.[36, 37] While the conventional CID system allowed PINK1 to recruit on the outer membrane of mitochondria followed by mitophagy induction,[38] the methods to induce PINK1/Parkin-mediated mitophagy in a photo-responsive manner has yet to be established.

To accomplish optical regulation of mitophagy, the author fused eDHFR to a cytosolic domain of PINK1 (PINK1Δ1–110, termed cytPINK1)[39] so that cytPINK1 would be recruited on the outer membrane of mitochondria by light (Figure 3-9a). cytPINK1-mOrange2-eDHFR and miRFP670nano-Parkin were co-expressed in HeLa cells with mitochondrial-outer-membrane anchored Halo-OMP25 and mEGFP-rLC3B, an autophagosome marker consisting of a microtubule-associated protein light chain 3[40] (LC3) and labeled with 7 μM pcDH.

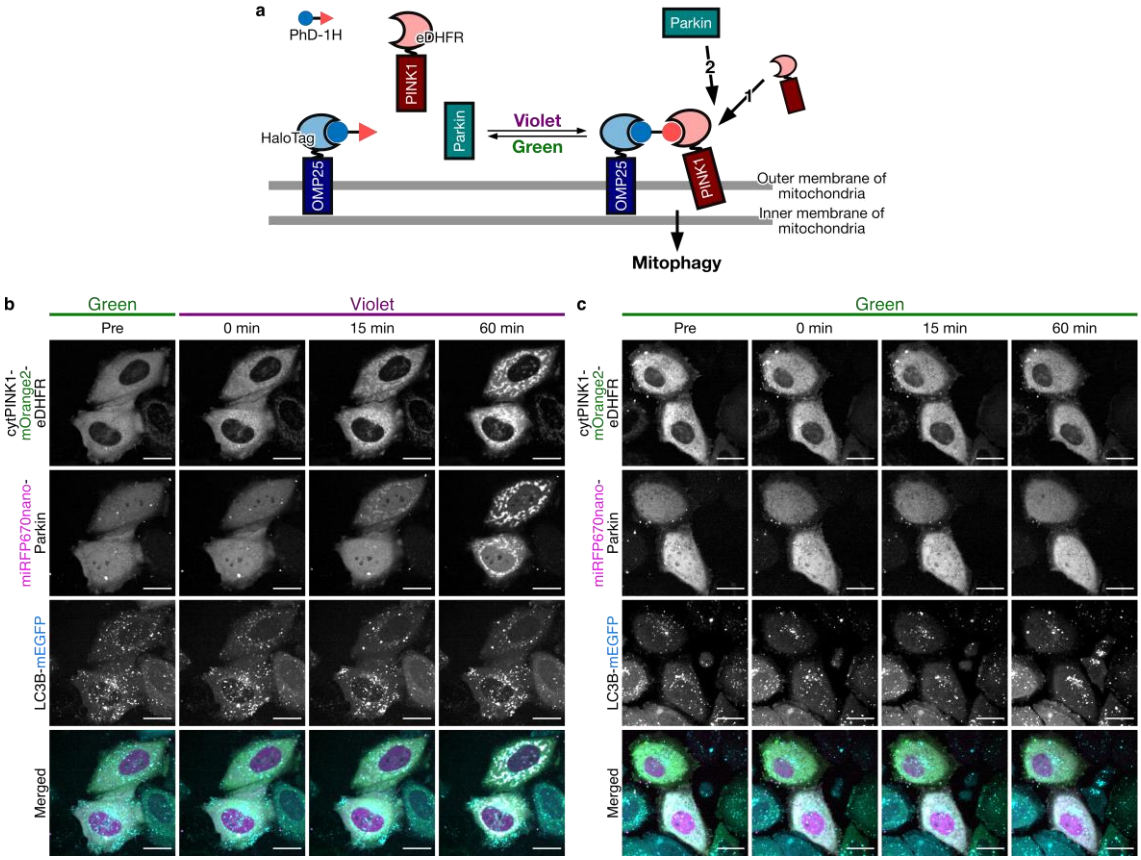

Figure 3-9. Optical regulation of mitophagy by the photochromic CID system. **a**) Schematic illustration of optically regulated mitophagy using the photochromic CID system. **b**,**c**) Time course of violet light-dependent recruitment of cytPINK1-mOrange2-eDHFR followed by miRFP670nano-Parkin accumulation. Confocal fluorescence images of HeLa cells expressing cytPINK1-mOrange2-eDHFR, miRFP670nano-Parkin, LC3B-mEGFP, and Halo-OMP25. 405-nm (violet) light was irradiated before the 0-min images were acquired and after every image acquisition (0–60 min, **b**). 555-nm (Green) light was irradiated after every image acquisition to suppress recruitment of cytPINK1-mOrange2-eDHFR by excitation light (**c**). Scale bars in all images, 20 μm.

Before violet light irradiation, cytPINK1-mOrange2-eDHFR was diffused in the cytosol. After violet light illumination, cytPINK1-mOrange2-eDHFR was quickly recruited onto the mitochondrial outer membrane, where Halo-OMP25 was expressed (Figure 3-9b). On the other hand, miRFP670nano-Parkin remained in the cytosol just after the illumination and accumulated on the mitochondria with several-minute delays (Figure 3-9b) as a previous report on rapalog-induced mitophagy.[38] Moreover, accumulation of mEGFP-LC3 was also observed after the Parkin accumulation (Figure 3-9b). Without violet light illumination, however, the mitochondrial recruitment of cytPINK1-mOrange2-eDHFR and miRFP670nano-Parkin was suppressed, and the accumulation level of mEGFP-LC3B was not significantly changed from the basal level (Figure 3-9c). Conversely, in the absence of pcDH, no accumulation of cytPINK1-mOrange2-eDHFR, miRFP670nano-Parkin, nor mEGFP-LC3B was observed upon either violet or green light illumination (Figure 3-10). The author also treated cells not expressing Parkin with pcDH followed by light illumination. In this case, cytPINK1 recruitment was still observed after violet light illumination, but mEGFP-LC3 little accumulated (Figure 3-11). Overall, the photochromic CID system achieved the optical induction of

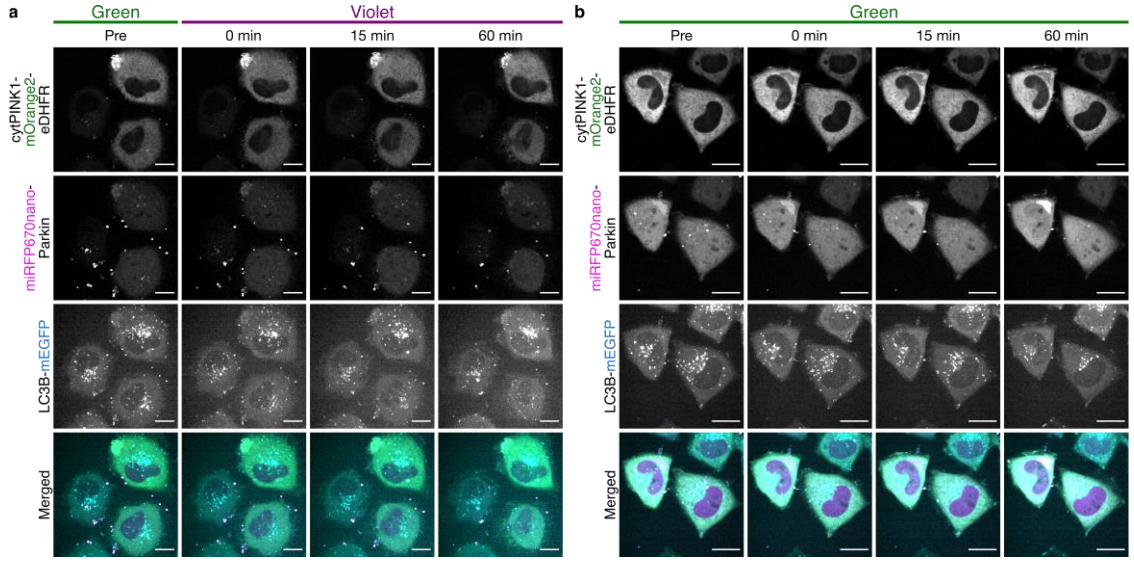

Figure 3-10. Evaluation of mitophagy induced by light-illumination. Confocal fluorescence images of HeLa cells expressing cytPINK1-mOrange2-eDHFR, miRFP670nano-Parkin, LC3B-mEGFP, and Halo-OMP25 without addition of pcDH. 405-nm (violet) light was irradiated before the 0-min images were acquired and after every image acquisition (0–60 min, **a**). 555-nm (Green) light was irradiated after every image acquisition to suppress recruitment of cytPINK1-mOrange2-eDHFR by excitation light (**b**). Scale bars in all images, 20 μm.

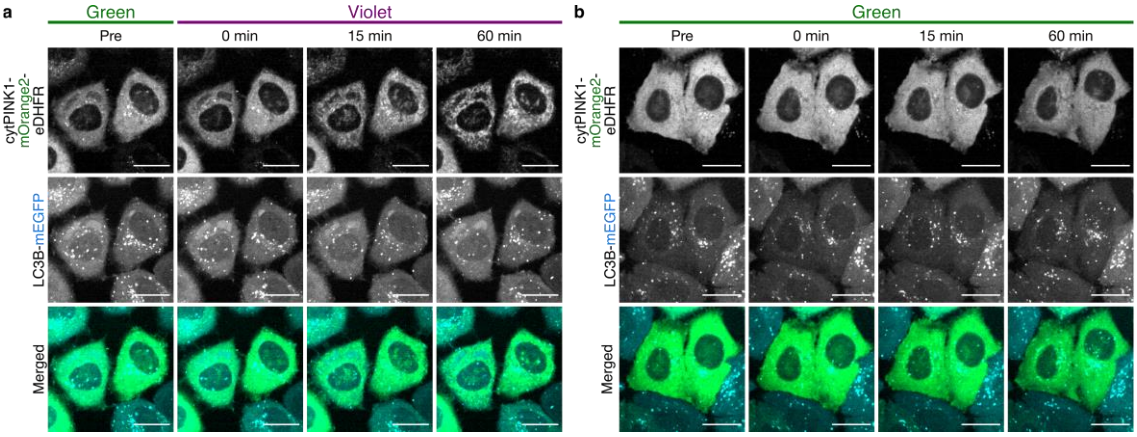

Figure 3-11. Verification of mitophagy induced by violet light illumination through PINK1/Parkin-mediated pathway. Confocal fluorescence images of HeLa cells expressing cytPINK1-mOrange2-eDHFR, miRFP670nano-Parkin, LC3B-mEGFP, and Halo-OMP25 teated with 7 μM pcDH. 405-nm (violet) light was irradiated before the 0-min images were acquired and after every image acquisition (0–60 min, **a**). 555-nm (Green) light was irradiated after every image acquisition to suppress recruitment of cytPINK1-mOrange2-eDHFR by excitation light (**b**). Scale bars in all images, 20 μm.

mitophagy through the PINK1/Parkin mediated pathway.

It was reported that the accumulation of phosphorylated ubiquitin on mitochondria is necessary for the removal of damaged mitochondria by mitophagy.[41] In the mitophagy pathway, deubiquitinating enzymes (DUBs) counter the pathway by removing ubiquitin chains from mitochondria until parkin activation is sufficient to overtake ubiquitin chain removal by DBUs.[42] This negative regulation seems to ensure that damage signals are strong enough to degrade so that healthy mitochondria do not inappropriately degrade. Indeed, it is thought that the balance between the activities of Parkin and DBUs sets a threshold for mitophagic flux that is dictated by the activity of PINK1 on the

mitochondria.[43] The author thereby speculated that temporal and quantitative recruitment of PINK1 on the mitochondria could determine mitophagy induction. Since the photochromic CID system recruits the eDHFR-fused protein repetitively, it can recruit cytPINK1 to the mitochondrial outer membrane in a temporally regulated manner. To achieve accurate control of PINK1 recruitment, the author co-expressed cytPINK1-mOrange2-eDHFR, miRFP670nano-Parkin together with Halo-OMP25 and mEGFP-rLC3B in HeLa cells. After treating the cells with 7 μM pcDH, the author temporally recruited cytPINK1 to the mitochondrial outer membrane by alternating violet and green light illumination. When cytPINK1 was recruited to the mitochondria for 10 min, accumulation of Parkin and LC3 was observed in most cells (Figure 3-12). Decreasing the duration of cytPINK1 recruitment on mitochondria, however, depleted accumulation of Parkin and LC3 (Figure 3-12b). These results may suggest a threshold on the duration time of PINK1 recruitment on the mitochondria for mitophagy induction.

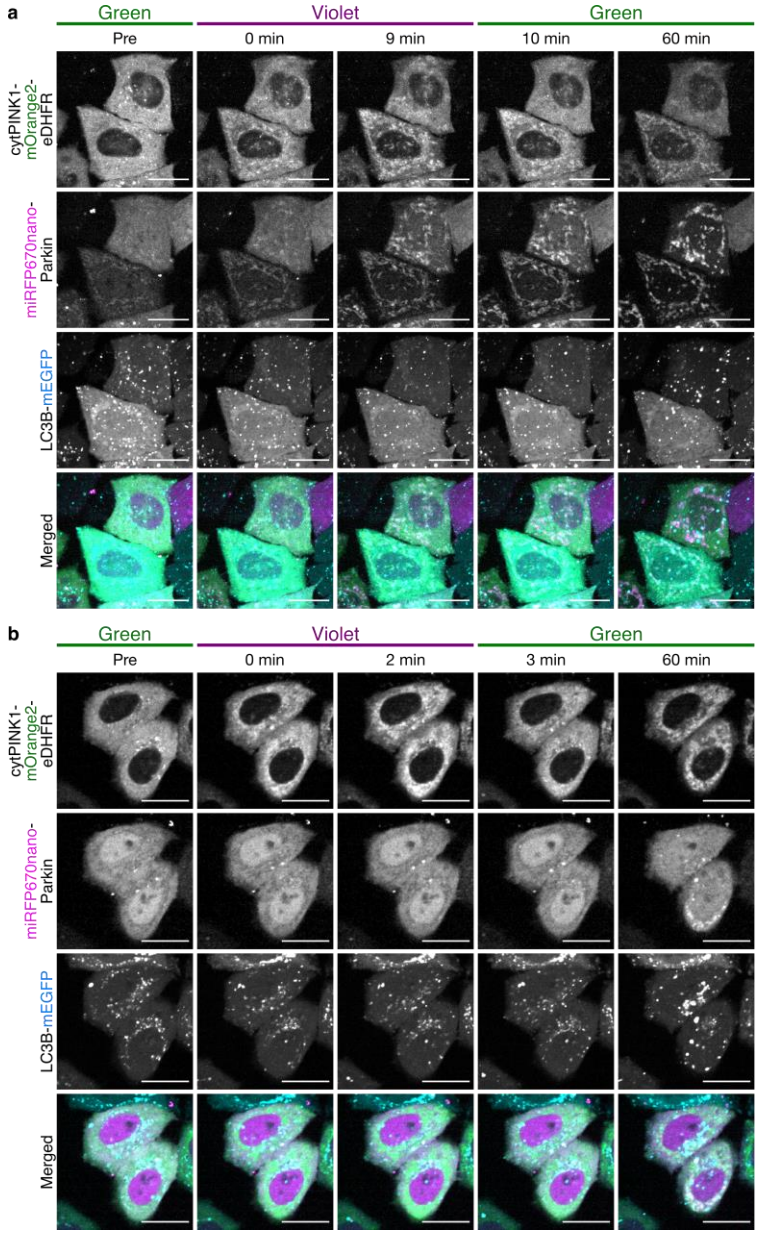

Figure 3-12. Temporal recruitment of cytPINK1 to mitochondria. 405-nm (violet) light was irradiated before the 0-min images were acquired and after every image acquisition during 0–9 min (**a**) or 0–2 min (**b**). 555-nm (Green) light was irradiated before the 10-min images (**a**) or 3-min images (**b**) were acquired and after every following images acquisition. Scale bars in all images, 20 μm.

3-6. Discussion

The author has developed a photoisomerization-based CID system that repetitively and quantitatively controls intracellular protein localization upon light irradiation. Treatment of live cells expressing organelle-targeting HaloTag and eDHFR with a photoisomerizable chemical dimerizer, pcDH, followed by violet and green light illumination reversibly localized and diffused eDHFR-fused protein. The cytosolic protein was repetitively localized to the plasma membrane, nucleus, ER membrane, and mitochondrial outer membrane using this photochromic CID system. Moreover, most translocation was completed within a few seconds, except for translocation through the nuclear membrane pores, which restricts the size of the transporting molecules.

The association and dissociation rates were quite fast upon light illumination. Since the bimolecular rate constant of the association is dependent on the concentrations of eDHFR, HaloTag, and the photochromic dimerizer, an accurate comparison with optogenetic tools requires more quantitative analysis, including the expression amount of the proteins. Meanwhile, the dissociation rate of a monomolecular reaction was faster than any conventional optogenetic tool. This result suggests that the photochromic CID system, which does not undergo a conformational change of protein, may offer more precise regulation in time than optogenetics. The duration of localization for several minutes required a couple of shot irradiation, presumably because the excitation light for a fluorescent protein isomerized pDL from *Z* isomer to *E* isomer. This isomerization is practically negligible using repetitive illumination with low-intensity light.

A few advanced methods recently have achieved quantitative translocation by optogenetics and photo-responsive CID systems that adopted illumination dose for quantitative translocation.[13, 15, 26] For the optogenetic PhyB-PIF system, irradiation simultaneous with different intensity ratios of activating and inactivating light was used to recruit protein at a certain level.[13, 15] For a photo-responsive CID system, the dose of illumination tuned translocation level.[26] Despite their great potential to quantitatively regulate protein recruitment, fine-tuning of translocation is expected to be difficult using a photo-responsive CID system because of its irreversibility. On the other hand, the photochromic CID system achieved quantitative translocation of the protein depending on the wavelength of irradiated light. That will be a complemental method for quantitative control of protein translocation.

Light-dependent recruitment of cytPINK1 to the mitochondrial outer membrane using the photochromic CID system provided deep insight on PINK1/Parkin-mediated mitophagy with higher temporal resolution than conventional CID systems. The activity of PINK1 to recruit Parkin to mitochondria is thought to be regulated by the autophosphorylation by the intermolecular reaction.[44] Since the efficiency of an intermolecular reaction is dependent on the concentration of components, temporal and quantitative regulation of PINK1 localization has the potential to ravel the relationship between the induction of mitophagy and the activity or quantity of PINK1 on the mitochondria. In the future, the photochromic CID approach can be a powerful complement for optogenetic and photo-responsive CID systems to perturb various cellular dynamics in a light-regulated manner.

The author demonstrated the photochromic CID approach; however, the author considers the

essence of this study as an innovative photo-reversible protein labeling system. The photo-reversible protein labeling system based on photochromism has the potential to provide a sophisticated spatiotemporal regulation to the conventional labeling systems, such as HaloTag,[30] SNAP-tag,[45] and eDHFR–TMP,[46] though the eDHFR–pDL pair has room for improvement about the difference between dissociation constants of *E*/*Z* isomers. That is likely due to removal or conversion to an amide of carboxylate groups in the parent molecule, azoMTX, while this suggests that proper derivatization of the photochromic ligand may enhance the affinity difference between the isomers. In addition to the derivatization of photochromic ligand, the author has addressed mutation into the substrate-binding site of the eDHFR and for the establishment of a system with better *E*/*Z* selectivity in chapter 4.

Finally, over a decade, CID approaches have still been used for artificial regulation of biomolecular dynamics even after tens of optogenetic tools were established. This suggests that the clear on/off switch offered by the CID approach is particularly useful in finding causality between biomolecular dynamics and cellular processes. Furthermore, splitting a module into protein and ligand brings various advantages, such that the concentration of small molecules can provide a simple adjustment of an amount of active module. Additionally, the ligand used is an option according to the intended use, such that the conventional chemical dimerizer can be used when light modulation is not required. That may provide an advantage in the investigation of an unsolved biological question as it is beneficial to start with conventional CID systems for robustness and switch to a photochromic CID system for finer control. HaloTag and eDHFR used in this study can also be visualized with the previously reported fluorescent ligands. It is possible to control the function of endogenous proteins by light with an endogenous protein-ligand linked to pDL instead of the HaloTag ligand. The author envisions that a photochromism-based strategy for optical control may expand the toolkit for precise control of the dynamics of intracellular protein and contribute to the study of diverse cellular processes.

3-7. Experimental section (chapter 3)

Materials, reagents, and instruments for chemical synthesis

Unless otherwise specified, all reagents were purchased from the chemical suppliers Fujifilm Wako Pure Chemical Corporation, Tokyo Chemical Industry Co., Kanto Chemical Co., Nacalai Tesque, Watanabe Chemical Industries, and Sigma-Aldrich Japan K.K. and were used without further purification. For all reactions requiring anhydrous conditions, the oven-heated glassware was dried in a vacuum, and the reactions were performed under a nitrogen atmosphere. Analytical thin-layer chromatography was performed using 60 F_{254} silica plates (Merck & Co., Inc.) and visualized under UV light or by staining with anisaldehyde, phosphomolybdic acid, or ninhydrin. Silica gel column chromatography was performed using PSQ60B (Fuji Silysia Chemical Ltd.).

NMR spectra were recorded on a Bruker AVANCE III 400 instrument at 400 MHz for ^{1}H NMR and 101 MHz for ^{13}C NMR, a Bruker AVANCE III 500 instrument at 500 MHz for ^{1}H NMR and 126 MHz for ^{13}C NMR, or a Bruker AVANCE III 600 instrument equipped with cryogenic probe at 600 MHz for ^{1}H NMR and 151 MHz for ^{13}C NMR. Chemical shifts (δ) are quoted in ppm downfield from tetramethylsilane, referenced to residual solvent signals (^{1}H NMR: δ = 7.26 for $CDCl_3$, 2.50 for DMSO-d_6, 3.31 for CD_3OD, and 4.79 for D_2O; ^{13}C NMR: δ = 39.5 for DMSO-d_6 and 49.1 for CD_3OD). Multiplicities are indicated as follows: s = singlet; d = doublet; t = triplet; q = quartet; quint = quintet; dd = doublet of doublet; m = multiplet. The high-resolution mass spectrometry analyses were performed on a Bruker micrOTOF-Q II mass spectrometer for electrospray ionization (ESI). High-performance liquid chromatography (HPLC) was performed with an Inertsil ODS-3 column (4.6 mm × 250 mm for analysis, 14.0 mm × 250 mm for purification, GL-Science Inc.), using an HPLC system that comprised a pump (PU-2080, JASCO) and a detector (MD-2010, JASCO), and the absorbance was monitored at 215, 254, 280, and 350 nm. Eluent A was composed of 0.1% formic acid in water. Eluent B was composed of 0.1% formic acid in acetonitrile.

Synthesis of pcDH, TMP-Fl, and TMP-HTL

Synthesis of pcDH

tert-Butyl (4-oxo-4-(prop-2-yn-1-ylamino)butyl)carbamate (**2**)[47]

The solution of **1** (1.00 g, 4.92 mmol), propargylamine (387 μL, 325 mg, 5.90 mmol), 1-ethyl-3-(3-dimethylaminopropyl)carbodiimide hydrochloride (EDC·HCl, 1.03 g, 5.37 mmol), and *N*,*N*-diisopropylethylamine (DIPEA, 2.00 mL, 1.52 g, 11.8 mmol) in dry dichloromethane (12 mL) was stirred at ambient temperature for 3 h. After the addition of saturated aqueous sodium bicarbonate solution (15 mL) at 0 °C, the organic materials were extracted with dichloromethane (6 × 20 mL). The organic layer was washed with saturated aqueous ammonium chloride solution (100 mL) and brine (100 mL), dried over magnesium sulfate, and concentrated in vacuo. The crude material was purified by silica gel column chromatography (1–3% methanol/dichloromethane) to give **2** (547 mg, 2.28 mmol, 46%) as a white solid.

^{1}H NMR (400 MHz, $CDCl_3$) δ 6.46 (br s, 1H), 4.76 (br s, 1H), 4.04 (dd, *J* = 5.2, 2.6 Hz, 2H), 3.21–3.12 (m, 2H), 2.24 (t, *J* = 7.3 Hz, 2H), 2.22 (t, *J* = 2.6 Hz, 1H), 1.81 (quint, *J* = 6.8 Hz, 2H), 1.44 (s, 9H); MS (ESI^+) *m*/*z*: Calc. for $C_{12}H_{20}N_2O_3Na^+$ $[M+Na]^+$ 263.14, found 263.14.

4-Oxo-4-(prop-2-yn-1-ylamino)butan-1-aminium 2,2,2-trifluoroacetate (**3**)

The solution of **2** (519 mg, 2.16 mmol) in dry dichloromethane (4.0 mL) and trifluoroacetic acid (TFA, 1.0 mL) was stirred at ambient temperature for 15 h. The removal of the volatile materials in vacuo to give **3** (569 mg, 2.16 mmol, quant.) as a yellow oil.

^{1}H NMR (400 MHz, DMSO-d_6) δ 8.40 (br t, *J* = 5.4 Hz, 1H), 7.92 (br s, 3H), 3.84 (dd, *J* = 5.4, 2.5 Hz, 2H), 3.08 (t, *J* = 2.5 Hz, 1H), 2.84–2.72 (m, 2H), 2.19 (t, *J* = 7.4 Hz, 2H), 1.75(quint, *J* = 7.4 Hz, 2H). MS (ESI^+) *m*/*z*: Calc. for $C_7H_{13}N_2O^+$ $[M+H]^+$ 141.10, found 141.10.

2-(2-((6-Chlorohexyl)oxy)ethoxy)ethan-1-aminium chloride (**5**)[48]

Hydrogen chloride in 1,4-dioxane (ca. 4 M, 1.9 mL) was added to the solution of **4** (801 mg, 2.49 mmol) in dry dichloromethane (5.0 mL) at 0 °C, and the solution was stirred at ambient temperature for 6 h. The removal of the volatile materials in vacuo to give **3** (651 mg, 2.49 mmol, quant.) as a yellow solid.

^{1}H NMR (400 MHz, $CDCl_3$) δ 8.59 (br s, 2H), 3.82 (t, *J* = 4.9 Hz, 2H), 3.70–3.68 (m, 2H), 3.61–3.58 (m, 2H), 3.55 (t, *J* = 6.7 Hz, 2H), 3.48 (t, *J* = 6.7 Hz, 2H), 3.23 (t, *J* = 4.9 Hz, 2H), 1.79 (tt, *J* = 7.8, 6.7 Hz, 2H), 1.62 (tt, *J* = 6.9, 6.9 Hz, 2H), 1.51–1.43 (m, 2H), 1.40–1.32 (m, 2H); MS (ESI^+) *m*/*z* Calc. for $C_{10}H_{23}{}^{35}ClNO_2^+$ $[M+H]^+$ 224.14, found 224.15.

2-(2-Hydroxyethoxy)ethyl 4-methylbenzenesulfonate (**7**)[49]

The solution of *p*-toluenesulfonyl chloride (4.00 g, 21.0 mmol) in tetrahydrofuran (THF, 30 mL) was added to the solution of **6** (16.0 mL, 17.9 g, 169 mmol) in THF (20 mL) and 2 M aqueous solution of sodium hydroxide (21 mL) at 0 °C, and the mixture was stirred at 0 °C for 1 h. After the addition of 10% aqueous solution of citric acid (40 mL) at 0 °C, the organic materials were extracted with ethyl acetate (3 × 40 mL). The organic layer was washed with brine (40 mL), dried over sodium sulfate, and concentrated in vacuo. The crude material was purified by silica gel column chromatography (33–100% ethyl acetate/haxane) to give **2** (547 mg, 2.28 mmol, 83%) as a white solid.

^{1}H NMR (400 MHz, $CDCl_3$) δ 7.80 (d, J = 8.4 Hz, 2H), 7.35 (d, J = 8.4 Hz, 2H), 4.20 (t, J = 4.8 Hz, 2H), 3.70 (t, J = 4.8 Hz, 2H), 3.66 (t, J = 4.8 Hz, 2H), 3.53 (t, J = 4.8 Hz, 2H), 2.45 (s, 3H); MS (ESI$^+$) m/z Calc. for $C_{11}H_{16}O_5SNa^+$ $[M+Na]^+$ 283.06, found 283.06.

2-(2-Azidoethoxy)ethan-1-ol (**8**)[49]

The suspension of **7** (4.74 g, 17.5 mmol) and sodium azide (2.84 g, 43.8 mmol) in dry *N*,*N*-dimethylformamide (DMF, 35 mL) was heated and stirred at 60 °C for 4.5 h. After the filtration through Celite 535, the filtrate was concentrated in vacuo. The remaining solution was diluted with brine (30 mL), and the organic materials were extracted with ethyl acetate (9 × 30 mL). The organic layer was dried over sodium sulfate and concentrated in vacuo to give **8** (1.90 g, 14.5 mmol, 83%) as a pale yellow oil.

^{1}H NMR (400 MHz, $CDCl_3$) δ 3.78 (dt, J = 6.0, 4.8 Hz, 2H), 3.69 (t, J = 4.8 Hz, 2H), 3.62 (t, J = 4.8 Hz, 2H), 3.42 (t, J = 4.8 Hz, 2H), 2.01 (t, J = 6.0 Hz, 1H); MS (ESI$^+$) m/z Calc. for $C_4H_9N_3O_2Na^+$ $[M+Na]^+$ 154.06, found 154.06.

tert-Butyl 2-(2-(2-azidoethoxy)ethoxy)acetate (**9**)[49]

The solution of *tert*-butyl bromoacetate (760 μL, 1.01 g, 5.18 mmol) in dry THF (14 mL) was added dropwise to the solution of 60% sodium hydride (159 mg, 3.97 mmol) and **8** (400 mg, 3.05 mmol) in dry THF (8.0 mL) at −20 °C, and the mixture was stirred at −20 °C for 12 h. After the addition of saturated aqueous ammonium chloride solution (30 mL) at 0 °C, the organic materials were extracted with ethyl acetate (3 × 30 mL). The organic layer was washed with brine (70 mL), dried over sodium sulfate, and concentrated in vacuo. The crude material was purified by silica gel column chromatography (0–50% ethyl acetate/hexane) to give **9** (300 mg, 867 μmol, 28%) as a colorless oil.

^{1}H NMR (400 MHz, $CDCl_3$) δ 4.04 (s, 2H), 3.72–3.67 (m, 6H), 3.42 (t, J = 5.2 Hz, 2H), 1.48 (s, 9H); MS (ESI$^+$) m/z Calc. for $C_{10}H19N_3O_4Na^+$ $[M+Na]^+$ 268.13, found 268.13.

2-(2-(2-Azidoethoxy)ethoxy)acetic acid (**10**)[49]

TFA (4.0 mL) was added to the solution of **9** (397 mg, 1.02 mmol) in dry dichloromethane (16 mL) at 0 °C and the mixture was stirred at ambient temperature for 2 h. After the removal of the volatile materials in vacuo, the crude material was purified by silica gel short pad (20% ethyl acetate/hexane and 25% methanol/ethyl acetate) to give **10** (193 mg, 1.02 mmol, quant.) as a pale yellow oil.
^{1}H NMR (400 MHz, $CDCl_3$) δ 8.37 (br s, 1H), 4.20 (s, 2H), 3.78–3.76 (m, 2H), 3.72–3.68 (m, 4H), 3.41 (t, J = 5.2 Hz, 2H); MS (ESI$^+$) m/z Calc. for $C_6H1_{11}N_3O_4Na^+$ $[M+Na]^+$ 212.06, found 268.13.

2-(2-(2-azidoethoxy)ethoxy)-*N*-(2-(2-((6-chlorohexyl)oxy)ethoxy)ethyl)acetamide (**11**)

The solution of **10** (22.7 mg, 120 μmol), **5** (37.5 mg, 144 μmol), EDC·HCl (36.8 mg, 192 μmol), and DIPEA (65.1 μL, 47.6 mg, 384 μmol) in dry dichloromethane (2.0 mL) was stirred at ambient temperature for 17 h. After the addition of saturated aqueous sodium bicarbonate solution (2 mL) at 0 °C, the organic materials were extracted with dichloromethane (3 × 2 mL). The organic layer was washed with brine (3 mL), dried over sodium sulfate, and concentrated in vacuo. The crude material was purified with silica gel column chromatography (50–100% ethyl acetate/hexane) to give **11** (34.5 mg, 84.4 μmol, 70%) as a pale yellow oil.
^{1}H NMR (400 MHz, $CDCl_3$) δ 7.05 (br s, 1H), 3.94 (s, 2H), 3.65–3.60 (m, 6H), 3.57–3.53 (m, 2H), 3.53–3.49 (m, 4H), 3.49–3.42 (m, 4H), 3.39 (t, J = 6.7 Hz, 2H), 3.36 (t, J = 5.0 Hz, 2H), 1.76–1.66 (m, 2H), 1.58–1.49 (m, 2H), 1.44–1.26 (m, 4H); ^{13}C NMR (101 MHz, $CDCl_3$) δ 169.7, 71.2, 70.8, 70.6, 70.2, 70.1, 70.0, 69.8, 50.5, 45.0, 38.5, 32.5, 29.4, 26.6, 25.4. (Two peaks were overlapped.); HRMS (ESI$^+$) m/z:Calcd. for $C_{16}H_{31}{}^{35}ClN_4O_5^+$ $[M+H]^+$ 395.2056, found 395.2063.

(*E*)-*N*-(4-(((1-(21-Chloro-8-oxo-3,6,12,15-tetraoxa-9-azahenicosyl)-1*H*-1,2,3-triazol-4-yl)methyl)amino)-4-oxobutyl)-4-((2,4-diaminoquinazolin-6-yl)diazenyl)benzamide (pcDH)

The suspension of **12** (330 mg, 1.02 mmol) in 10% aqueous solution of sodium hydroxide (5.0 mL) and THF (20 mL) was heated and stirred at 60 °C for 24 h. After the removal of the volatile materials in vacuo, the remaining solid was dissolved in water (30 mL) and was neutralized with 2 M aqueous hydrochloric acid (35 mL). The precipitation was washed with water to give the carboxylic acid as a dark red solid (279 mg). The suspension of the carboxylic acid (40.0 mg), **3** (49.3 mg, 194 μmol), 2-(1*H*-benzotriazole-1-yl)-1,1,3,3-tetramethyluronium hexafluorophosphate (HBTU, 54.0 mg, 142 μmol), and DIPEA (66.3 μL, 50.4 mg, 390 μmol) in DMF (2.5 mL) was stirred at ambient temperature for 15 h. After the removal of the volatile materials in vacuo, the remaining solid was washed with dichloromethane to give the alkyne (64.3 mg) as an orange solid. The suspension of the alkyne (23.3 mg), **11** (21.4 mg, 54.2 μmol), copper(II) sulfate pentahydrate (1.41 mg, 5.65 μmol), and sodium ascorbate (2.21 mg, 11.2 μmol) in DMF (4.0 mL) and tert-butyl alcohol (1.0 mL) was stirred at ambient temperature for 33 h. After the removal of the volatile materials in vacuo, the remaining solid was purified by HPLC to give pcDH (6.73 mg, 8.15 μmol, 16% in 3 steps) as an orange solid.
^{1}H NMR (600 MHz, DMSO-d_6) δ 8.87 (d, J = 1.7 Hz, 1H), 8.71 (br s, 2H), 8.67 (br t, J = 5.6 Hz, 1H),

8.35 (br t, *J* = 5.7 Hz, 1H), 8.21 (dd, *J* = 8.9, 1.7 Hz, 1H), 8.06 (d, *J* = 8.6 Hz, 2H), 7.93 (d, *J* = 8.6 Hz, 2H), 7.91 (s, 1H), 7.65 (br s, 2H), 7.61 (br t, *J* = 5.8 Hz, 1H), 7.51 (d, *J* = 8.9 Hz, 1H), 4.50 (t, *J* = 5.3 Hz, 2H), 4.30 (d, *J* = 5.6 Hz, 2H), 3.83 (s, 2H), 3.81 (t, *J* = 5.3 Hz, 2H), 3.60 (t, *J* = 6.6 Hz, 2H), 3.57–3.52 (m, 4H), 3.49–3.46 (m, 2H), 3.45–3.42 (m, 2H), 3.41 (t, *J* = 6.0 Hz, 2H), 3.25 (q, *J* = 6.0 Hz, 2H), 2.19 (t, *J* = 7.5 Hz, 2H), 1.79 (quint, *J* = 7.3 Hz, 2H), 1.68 (quint, *J* = 7.0 Hz, 2H), 1.46 (quint, *J* = 7.0 Hz, 2H), 1.39–1.32 (m, 2H), 1.31–1.24 (m, 2H); ^{13}C NMR (151 MHz, DMSO-d_6) δ 172.2, 169.7, 165.9, 163.7, 163.5, 158.8, 158.6, 153.7, 147.6, 145.4, 137.1, 129.0, 125.9, 124.5, 123.6, 122.6, 110.3, 70.6, 70.5, 70.4, 70.0, 69.9, 69.8, 69.3, 69.2, 49.7, 45.8, 40.5, 38.4, 34.6, 33.3, 32.5, 29.5, 26.6, 25.7, 25.4; MS (ESI$^+$) m/z: Calcd. for $C_{38}H_{55}{}^{35}ClN_{12}O_7{}^+$ $[M+2H]^{2+}$ 413.20, found 413.21.

Synthesis of TMP-Fl

Scheme 3-2. Synthetic route to TMP-Fl

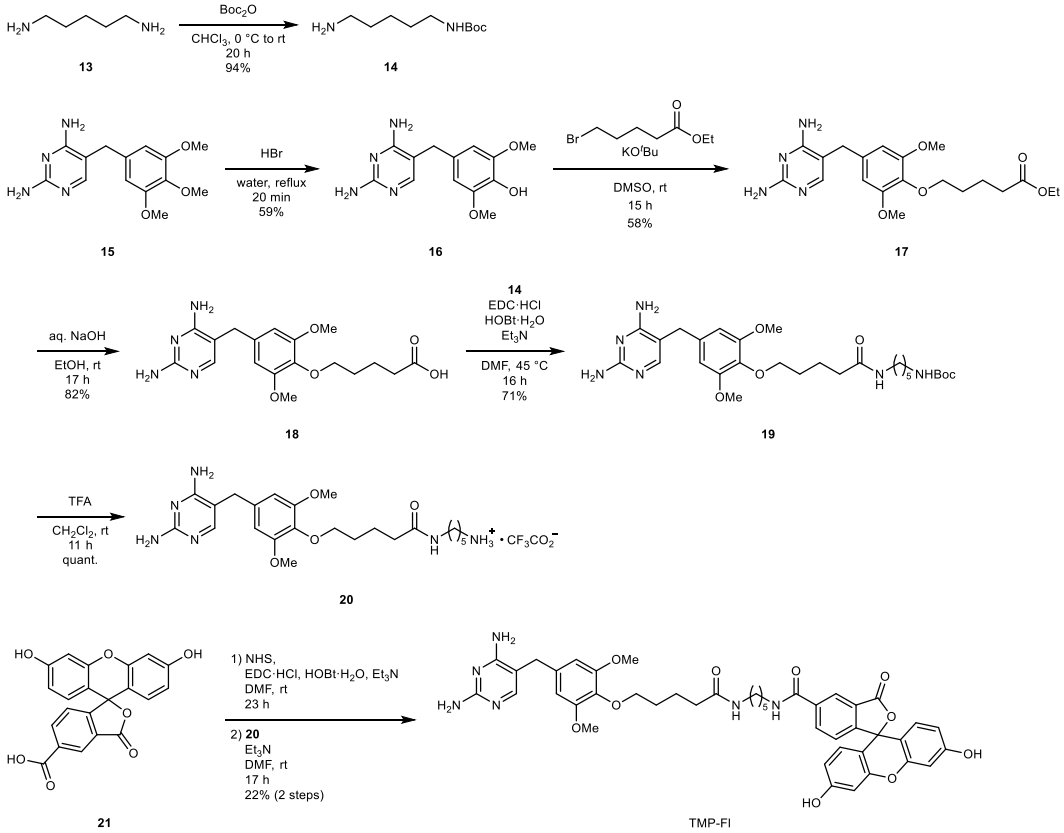

<u>*tert*-Butyl (5-aminopentyl)carbamate (**14**)[50]</u>

The solution of di-*tert*-butyl dicarbonate (750 µL, 713 mg, 3.27 mmol) in chloroform (3.0 mL) was added dropwise to the solution of **13** (2.10 mL, 1.83 g, 17.9 mmol) in chloroform (16 mL) at 0 °C, and the mixture was stirred at ambient temperature for 20 h. After the filtration through Celite 535, the filtrate was washed with water (60 mL) and brine (60 mL), dried over sodium sulfate, and concentrated in vacuo. The crude material was purified by silica gel column chromatography (7–20% methanol/dichloromethane containing 0.5% triethylamine) to give **14** (626 mg, 3.09 mmol, 94%) as a yellow oil.

^{1}H NMR (400 MHz, $CDCl_3$) δ 4.73 (br s, 1H), 3.09–2.99 (m, 2H), 2.63 (t, J = 7.0 Hz, 2H), 2.12 (br s, 2H), 1.48–1.33 (m, 13H), 1.33–1.23 (m, 2H).

4-((2,4-Diaminopyrimidin-5-yl)methyl)-2,6-dimethoxyphenol (**16**)[51]

The solution of **15** (5.00 g, 17.2 mmol) in 48% aqueous hydrobromic acid (60 mL) was heated and stirred at reflux temperature for 20 min. After cooling, the reaction mixture was neutralized with 50% aqueous solution of sodium hydroxide. The precipitation was washed with water and dissolved in boiling water. After the further neutralization with 10% aqueous ammonia solution, the precipitation was washed with water and dichloromethane to give **16** (2.80 g, 10.1 mmol, 59%) as a white solid.
^{1}H NMR (400 MHz, DMSO-d_6) δ 8.12 (br s, 1H), 7.45 (s, 1H), 6.49 (s, 2H), 6.16 (br s, 2H), 5.83 (br s, 2H), 3.70 (s, 6H), 3.47 (s, 2H); MS (ESI$^+$) m/z: Calc. for $C_{13}H_{17}N_4O_3^+$ $[M+H]^+$ 277.13, found 277.12.

Ethyl 5-(4-((2,4-diaminopyrimidin-5-yl)methyl)-2,6-dimethoxyphenoxy)pentanoate (**17**)[51]

The suspension of 16 (501 mg, 1.81 mmol), ethyl 5-bromovalerate (430 µL, 563 mg, 2.69 mmol), and potassium *tert*-butoxide (305 mg, 2.72 mmol) in dimethyl sulfoxide (DMSO, 5.0 mL) was stirred at ambient temperature for 15 h. After the addition of water (5 mL), the organic materials were extracted with ethyl acetate (8 × 10 mL). The organic layer was washed with water (30 mL) and brine (30 mL), dried over sodium sulfate, and concentrated in vacuo. The crude material was purified by silica gel column chromatography (3–10% methanol/dichloromethane) to give **17** (425 mg, 1.05 mmol, 58%) as a pale yellow solid.
^{1}H NMR (400 MHz, $CDCl_3$) δ 7.72 (s, 1H), 6.34 (s, 2H), 5.27 (br s, 2H), 4.76 (br s, 2H), 4.09 (q, J = 7.1 Hz, 2H), 3.90 (t, J = 6.2 Hz, 2H), 3.74 (s, 6H), 3.60 (s, 2H), 2.35 (t, J = 7.3 Hz, 2H), 1.85–1.69 (m, 4H), 1.21 (t, J = 7.1 Hz, 3H); MS (ESI$^+$) m/z: Calc. for $C_{20}H_{29}N_4O_5^+$ $[M+H]^+$ 405.21, found 405.22.

5-(4-((2,4-Diaminopyrimidin-5-yl)methyl)-2,6-dimethoxyphenoxy)pentanoic acid (**18**)[51]

The solution of **17** (304 mg, 752 µmol) in 5 M aqueous sodium hydroxide solution (0.45 mL) and ethanol (5.0 mL) was stirred at ambient temperature for 17 h. After the removal of the volatile materials in vacuo, the remaining materials were dissolved in water and neutralized with 1 M aqueous hydrochloric acid to give **18** (232 mg, 616 µmol, 82%) as a white solid.
^{1}H NMR (400 MHz, DMSO-d_6) δ 7.50 (s, 1H), 6.54 (s, 2H), 6.11 (br s, 2H), 5.71 (br s, 2H), 3.77 (t, J = 6.0 Hz, 2H), 3.70 (s, 6H), 3.52 (s, 2H), 2.26 (t, J = 7.1 Hz, 2H), 1.70–1.55 (m, 4H); MS (ESI$^+$) m/z: Calc. for $C_{18}H_{25}N_4O_5^+$ $[M+H]^+$ 377.18, found 377.18.

tert-Butyl (5-(5-(4-((2,4-diaminopyrimidin-5-yl)methyl)-2,6-dimethoxyphenoxy)pentanamido)pentyl)carbamate (**19**)[52]

The solution of **18** (100 mg, 266 μmol), **14** (81.8 mg, 404 μmol), EDC·HCl (62.2 mg, 324 μmol), 1-hydroxy-1*H*-benzotriazole hydrate (HOBt·H_2O, 41.1 mg, 268 μmol), and DIPEA (140 μL, 187 mg, 1.45 mmol) in dry DMF (1.5 mL) was heated and stirred at 45 °C for 15 h. After cooling, the volatile materials were removed in vacuo. The crude material was purified by silica gel column chromatography (5–16% methanol/dichloromethane) to give **19** (106 mg, 189 μmol, 71%) as a pale yellow solid.

^{1}H NMR (400 MHz, CD_3OD) δ 7.31 (s, 1H), 6.54 (s, 2H), 3.91 (t, *J* = 6.2 Hz, 2H), 3.79 (s, 6H), 3.65 (s, 2H), 3.16 (t, *J* = 7.0 Hz, 2H), 3.02 (t, *J* = 7.0 Hz, 2H), 2.25 (t, J = 7.3 Hz, 2H), 1.85–1.75 (m, 2H), 1.75–1.66 (m, 2H), 1.55–1.39 (m, 13H), 1.37–1.25 (m, 2H).

5-(5-(4-((2,4-Diaminopyrimidin-5-yl)methyl)-2,6-dimethoxyphenoxy)pentanamido)pentan-1-aminium 2,2,2-trifluoroacetate (**20**)

The solution of **19** (73.9 mg, 132 μmol) in TFA (0.50 mL) and dry dichloromethane (2.0 mL) was stirred at ambient temperature for 11 h. After the removal of the volatile materials in vacuo, the crude **20** (115 mg) was used for the next reaction without further purification.

^{1}H NMR (400 MHz, CD_3OD) δ 7.24 (s, 1H), 6.56 (s, 2H), 3.91 (t, *J* = 6.1 Hz, 2H), 3.80 (s, 6H), 3.66 (s, 2H), 3.19 (t, *J* = 7.0 Hz, 2H), 2.92 (t, *J* = 7.6 Hz, 2H), 2.26 (t, *J* = 7.3 Hz, 2H), 1.86–1.76 (m, 2H), 1.76–1.63 (m, 4H), 1.60–1.50 (m, 2H), 1.45–1.36 (m, 2H); MS (ESI$^+$) *m*/*z*: Calc. for $C_{23}H_{38}N_6O_4^{2+}$ $[M+2H]^{2+}$ 231.15, found 231.15.

N-(5-(5-(4-((2,4-Diaminopyrimidin-5-yl)methyl)-2,6-dimethoxyphenoxy)pentanamido)pentyl)-3',6'-dihydroxy-3-oxo-3*H*-spiro[isobenzofuran-1,9'-xanthene]-5-carboxamide (TMP-Fl)

The solution of **21** (20.2 mg, 53.7 μmol), *N*-hydroxysuccinimide (NHS, 14.2 mg, 123 μmol), EDC·HCl (12.7 mg, 66.2 μmol), HOBt·H_2O (9.27 mg, 60.5 μmol), and triethylamine (22.2 μL, 16.2 mg, 160 μmol) in dry DMF (1.0 mL) was stirred at ambient temperature for 23 h. After the addition of 10% aqueous solution of citric acid (10 mL) at ambient temperature, the organic materials were extracted with ethyl acetate (3 × 10 mL). The organic layer was washed with water (40 mL) and brine (40 mL), dried over magnesium sulfate, and concentrated in vacuo to give the activated ester (33.0 mg) as a yellow solid. The solution of the activated ester (33.0 mg), **20** (20.4 mg, 43.1 μmol), and triethylamine (30.0 μL, 21.9 mg, 216 μmol) in dry DMF (1.0 mL) was stirred at ambient temperature for 17 h. After the removal of the volatile materials in vacuo, the remaining solid was purified by HPLC to give TMP-Fl (9.60 mg, 11.7 μmol, 22% in 2 steps) as a yellow solid.

^{1}H NMR (600 MHz, CD_3OD) δ 8.42 (d, *J* = 1.7 Hz, 1H), 8.15 (dd, *J* = 8.0, 1.7 Hz, 1H), 7.31 (d, *J* = 8.0 Hz, 1H), 7.20 (s, 1H), 6.71 (d, *J* = 8.8 Hz, 2H), 6.68 (d, *J* = 2.4 Hz, 2H), 6.55 (dd, *J* = 8.8, 2.4 Hz, 2H), 6.53 (s, 2H), 3.90 (t, *J* = 6.3 Hz, 2H), 3.78 (s, 6H), 3.63 (s, 2H), 3.44 (t, *J* = 6.9 Hz, 2H), 3.21 (t, *J* = 6.8 Hz, 2H), 2.25 (t, *J* = 7.4 Hz, 2H), 1.82–1.76 (m, 2H), 1.73–1.66 (m, 4H), 1.61–1.55 (m, 2H),

1.49–1.42 (m, 2H); ^{13}C NMR (151 MHz, CD_3OD) δ 176.1, 171.2, 169.3, 168.6, 165.8, 157.7, 155.3, 155.1, 143.7, 137.8, 137.1, 134.1, 133.9, 130.7, 127.1, 126.0, 115.9, 112.2, 110.4, 107.3, 103.7, 73.9, 56.6, 49.6, 41.0, 40.1, 36.8, 34.1, 30.5, 30.1, 30.0, 25.3, 23.8 (Two peaks could not be discriminated because of overlap with another peak.); HRMS (ESI$^+$) *m*/*z* Calcd. for $C_{44}H_{47}N_6O_{10}^+$ $[M+H]^+$ 819.3348, found 819.3341.

Synthesis of TMP-HTL

Scheme 3-3. Synthetic route to TMP-HTL

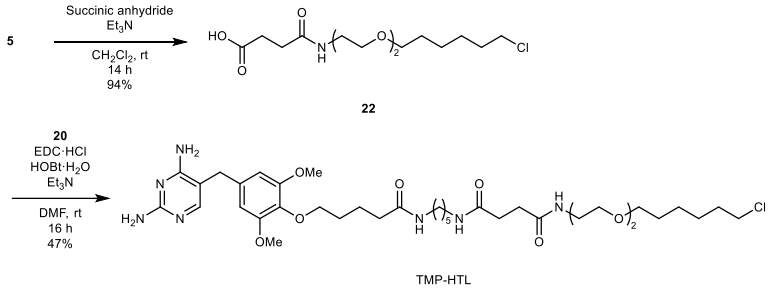

4-((2-(2-((6-Chlorohexyl)oxy)ethoxy)ethyl)amino)-4-oxobutanoic acid (**22**)[25]

The solution of **5** (187 mg, 454 µmol), succinic anhydride (136 mg, 1.36 mmol), and triethylamine (370 µL, 270 mg, 2.67 mmol) in dry dichloromethane (2.0 mL) was stirred at ambient temperature for 14 h. After the addition of 1 M aqueous solution of hydrochloric acid (5 mL) at 0 °C, the organic and water layers were separated. The organic layer was washed with 1 M aqueous solution of hydrochloric acid (2 × 5 mL), and dried over magnesium sulfate, and concentrated in vacuo to give **22** (138 mg, 426 µmol, 94%) as a brown oil.

^{1}H NMR (500 MHz, $CDCl_3$) δ 6.39 (s, 1H), 4.15 (s, 2H), 3.62 (s, 4H), 3.56–3.49 (m, 6H), 3.75–3.65 (m, 14H), 2.70–2.65 (m, 2H), 2.55–2.50 (m, 2H), 1.81–1.73 (m, 2H), 1.68–1.59 (m, 2H), 1.50–1.42 (m, 2H), 1.42–1.33 (m, 2H); MS (ESI$^-$) *m*/*z* Calcd. for $C_{14}H_{26}NO_5{}^{35}Cl^-$ $[M-H]^-$ 322.15, found 322.14.

N^1-(2-(2-((6-Chlorohexyl)oxy)ethoxy)ethyl)-*N*^{4}-(5-(5-(4-((2,4-diaminopyrimidin-5-yl)methyl)-2,6-dimethoxyphenoxy)pentanamido)pentyl)succinamide (TMP-HTL)

The solution of **22** (22.8 mg, 70.4 µmol), **20**, (48.3 mg, 84.1 µmol), EDC·HCl (16.4 mg, 85.6 µmol), HOBt·H_2O (11.5 mg, 75.1 µmol), and DIPEA (31.0 µL, 23.0 mg, 180 µmol) in dry DMF (1.0 mL) was stirred at ambient temperature for 15 h. After the removal of the volatile materials in vacuo, the remaining solid was purified by HPLC to give TMP-HTL (25.3 mg, 33.0 µmol, 47%) as a white solid.

^{1}H NMR (600 MHz, CD_3OD) δ 7.31 (s, 1H), 6.55 (s, 2H), 3.92 (t, *J* = 6.3 Hz, 2H), 3.80 (s, 6H), 3.65 (s, 2H), 3.61–3.57 (m, 4H), 3.55 (t, *J* = 6.6 Hz, 2H), 3.52 (t, *J* = 5.6 Hz, 2H), 3.48 (t, *J* = 6.6 Hz, 2H), 3.34 (t, *J* = 5.6 Hz, 2H), 3.19–3.13 (m, 4H), 2.50–2.43 (m, 4H), 2.25 (t, J = 7.4 Hz, 2H), 1.83–1.68 (m, 6H), 1.62–1.56 (m, 2H), 1.54–1.43 (m, 6H), 1.42–1.31 (m, 4H); ^{13}C NMR (151 MHz, CD_3OD) δ 176.0, 174.7, 174.5, 170.0, 165.8, 158.2, 155.0, 144.7, 137.1, 134.4, 110.2, 107.1, 73.9, 72.2, 71.3, 71.2, 70.5,

56.6, 45.7, 40.4, 40.3, 40.2, 36.8, 34.1, 33.7, 32.3, 30.6, 30.5, 30.1, 30.0, 27.7, 26.5, 25.2, 23.7. HRMS (ESI^+) *m/z*: Calc. for $C_{37}H_{60}{}^{35}ClN_7O_8^+$ $[M+H]^+$ 766.4265, found 766.4266.

pcDH characterization in vitro

UV/vis absorption spectra and time-dependent absorption change were recorded on a Shimadzu UV-2450 spectrophotometer, with the slit width set to 1 nm. pcDH (20 μM) was incubated at 37 °C for 1 h in 100 mM HEPES-NaOH buffer (pH 7.4) containing 100 mM NaCl and 1% DMSO before the measurements. For photoisomerization analysis of pcDH, light irradiation was performed by a Xe light source (MAX-303, Asahi Spectra) equipped with band-pass filters (330/10, 365/10, 394/10, 440/10, 450/10, 488/10, 515/10, or 560/10) at room temperature (5.0 mW cm^{-2}). For the thermal relaxation experiment, the sample absorbance at 350 nm was recorded at 37 °C in a dark state after illumination at 394 nm light (5.0 mW cm^{-2}).

HPLC analyses were performed with an Inertsil ODS-3 column (4.6 mm × 250 mm, GL-Science), using an HPLC system that comprised a pump (PU-2080, JASCO) and a detector (MD-2010, JASCO), and the absorbance was monitored at 264 and 414 nm that were isosbestic points of pcDH in the eluent. Eluent A was composed of 0.1% formic acid in water. Eluent B was composed of 0.1% formic acid in acetonitrile. pcDH (100 μM) was incubated at 37 °C for 1 h in 100 mM HEPES-NaOH buffer (pH 7.4) containing 2% DMSO before the measurements. Light irradiation was performed by a Xe light source at room temperature (5.0 mW cm^{-2}).

The binding affinity of pcDH and HaloTag-bonded pcDH was determined by a fluorescence depolarization assay recorded on a multimode plate reader (Nivo, PerkinElmer). The mixture of pcDH, TMP-Fl (1.5 nM), eDHFR (2.0 nM), and NADPH (5.0 μM) was incubated at 37 °C for 45 min in 100 mM HEPES-NaOH buffer (pH 7.4) containing 100 mM NaCl before the measurements. pcDH was irradiated with 394/10 nm light (5.0 mW cm^{-2}) at room temperature to obtain pcDH under 394-nm irradiation before mixing with other components. The IC_{50} values were determined from the obtained plot using equation (1).

$$P = P_{min} + (P_{max} - P_{min}) / (1 + ([pcDH] / IC_{50})) \quad (1)$$

, where P is the fluorescence polarization at each pcDH concentration, P_{max} is the fluorescence polarization without pcDH, and P_{min} is the minimum fluorescence polarzation.

The dissociation constant (K_d) was calculated from the determined IC_{50} value using Nikolovska-Coleska equation[53] (2).

$$K_d = [I]_{50} / ([L]_{50} / K_{d,L} + [P]_0 / K_{d,L} + 1) \quad (2)$$

, where $[I]_{50}$ is the concentration of the pcDH at 50% inhibition, $[L]_{50}$ the concentration of the free TMP-Fl at 50% inhibition, $[P]_0$ is the concentration of the free eDHFR at 0% inhibition, and $K_{d,L}$ is the dissociation constant of the eDHFR–TMP-Fl complex ($K_{d,L}$ = 0.25 ± 0.06 nM, mean ± s.d., n = 5).

DNA plasmid construction

Synthetic genes encoding mOrange2, miRFP670nano, and Parkin were purchased from Eurofins Genomics. A gene encoding cytPINK1 was obtained from pcDNA-DEST47 PINK1 C-GFP (Addgene, #13316) using a standard PCR method (Takara).

The plasmids for recombinant eDHFR expression was prepared according to a method described previously.[54]

For eDHFR-miRFP670nano, the gene encoding the fusion protein of eDHFR and miRFP670nano was inserted into the *Nhe*I/*Eco*RI site of the pcDNA3.1(+) vector (Invitrogen). A single *Hind*III site and three amino acids (AAA) were inserted between the eDHFR and miRFP670nano sequences. For nuclear exporting, human immunodeficiency virus-1 Rev protein nuclear exporting sequence (NES: LQLPPLERLTL)[55] were incorporated at the C-terminus of miRFP670nano, and a single *Bam*HI site and eight amino acids (QLGGSGGS) were inserted between the miRFP670nano and NES sequences.

For nuclear targeting Halo-mOrange2, three copies of the simian virus 40 (SV40) large T-antigen nuclear localization sequence (NLS: PKKKRKVDPKKKRKVDPKKKRKV)[56] were incorporated at the C-terminus of the fusion protein of HaloTag and mOrange2. A single *Hind*III site was inserted between the Halo and mOrange2 sequences, and a single *Bam*HI site and six amino acids (GGSGGS) were inserted between the mOrange2 and NLS sequences. The gene encoding Halo-mOrange2-NLS was inserted into the *Nhe*I/*Eco*RI site of the pcDNA3.1(+) vector. For anchoring Halo-mOrange2 to the cytosolic interface of the plasma membrane, the CAAX sequence of Kras (KKKKKKSKTKCVIM)[57] was incorporated at the C-terminus of the fusion protein of HaloTag and mOrange2. A single *Bam*HI site and an amino acid (G) were inserted between the mOrange2 and CAAX sequences. For ER targeting, the ER-targeting domain of cytochrome b5 (Cb5: amino acids 100–134)[58] was incorporated at the C-terminus of the fusion protein of HaloTag and mOrange2. A single *Bam*HI site and four amino acids (GGGS) were inserted between the mOrange2 and Cb5 sequences. For mitochondrial outer membrane targeting, the mitochondria-targeting domain of Tom20 (amino acids 1–33)[59] was incorporated at the N-terminus of the fusion protein of mOrange2 and HaloTag. There was only a single *Bam*HI site between the mOrange2 and Halo sequences and was only a single *Hind*III site between the Tom20 and mOrange2 sequences. The gene encoding Tom20-mOrange2-Halo was inserted into the *Nhe*I/*Eco*RI site of the pcDNA3.1(+) vector.

For cytPINK1-mOrange2-eDHFR, the gene encoding cytPINK1-mOrange2-eDHFR was inserted into the *Nhe*I/*Eco*RI site of the pcDNA3.1(+) vector. A 2×GGGS flexible linker was inserted into the *Afl*II/*Bam*HI site between cytPINK1 and mOrange2. V5-tag sequence was incorporated at the C-terminus of the fusion protein. Two amino acids (GS) and a single *Hind*III site was inserted between the mOrange2 and eDHFR sequences, and a single *Sac*II site and four amino acids (GGGS) were inserted between the eDHFR and V5-tag sequences.

For Parkin-miRFP670nano, the gene encoding Parkin-miRFP670nano was inserted into the *Nhe*I/*Eco*RI site of the pcDNA3.1(+) vector. HA-tag sequence was incorporated at the N-terminus of the fusion protein. There was only a single *Hind*III site between the HA-tag and miRFP670nano

sequences and was only a single *Bam*HI site between the miRFP670nano and Parkin sequences. All plasmids were verified by Sanger sequencing.

Recombinant protein expression and purification

Recombinant eDHFR was expressed and purified according to the reported method.[54]

Cell culture and transfection

HeLa cells were cultured in Minimum Essential Media (MEM, Nacalai) supplemented with 10% fetal bovine serum (FBS, Gibco), 100 U/mL penicillin and 100 μg/mL streptomycin (Nacalai) at 37 °C in a humidified incubator with 5% CO_2. Three days before imaging, the cells were seeded on 35-mm glass-bottomed dishes (AGC Techno Glass) in antibiotic-free MEM supplemented with 10% FBS. After 24 h, transfection was performed using FuGENE HD (Promega) according to the manufacturer's protocols with plasmid DNA and FuGENE HD at a 1:7 ratio in Opti-MEM (Gibco).

Live-cell imaging

All images were acquired on an inverted IX83 microscope (Olympus) equipped with a ×60/1.49 numerical aperture (NA) oil objective (APON 60XOTIRF, Olympus), a multi-wavelength laser diode light source (LDI-7, 89 North), a spinning-disk unit (CSU-W1, Yokogawa), and an ORCA-Fusion BT CMOS camera (Hamamatsu). The microscope was driven by Metamorph 7.10 software (Molecular device). mEGFP images were acquired using the 470-nm laser, a 405/488/561/640 dichroic mirror, and a 525/50 emission filter. mOrange2 images were acquired using the 555-nm laser, a 405/488/561/640 dichroic mirror, and a 600/50 emission filter. miRFP670nano images were acquired using the 640-nm laser, a 405/488/561/640 dichroic mirror, and a 700/75 emission filter. The cells were maintained in a controlled-environment chamber (Incubator System T, LCI) at 37 °C during imaging.

To perform photo-reversible protein translocation assay, HeLa cells were plated at 5.0×10^4 cells per dish and transfected with four pairs of plasmids (cytosolic interface of plasma membrane: pcDNA3.1(+)-eDHFR-miRFP670nano-NES and pcDNA3.1(+)-Halo-mOrange2-CAAX; nucleus: pcDNA3.1(+)-eDHFR-miRFP670nano and pcDNA3.1(+)-Halo-mOrange2-NLS; mitochondrial outer membrane: pcDNA3.1(+)-eDHFR-miRFP670nano-NES and pcDNA3.1(+)-Tom20-mOrange2-Halo; cytosolic interface of ER membrane: pcDNA3.1(+)-eDHFR-miRFP670nano-NES and pcDNA3.1(+)-Halo-mOrange2-Cb5). The ratio of the plasmids used were as follows: 1:2 (eDHFR-miRFP670nano-NES/Halo-mCherry-CAAX, eDHFR-miRFP670nano/Halo-mCherry-NLS) and 2:3 (eDHFR-miRFP670nano-NES/Tom20-mOrange2-Halo, eDHFR-miRFP670nano-NES/Halo-mOrange2-Cb5). After 36 h of transfection, the cells were washed twice with Hanks' Balanced Salt Solution (HBSS (+)) and treated with 5 μM pcDH (plasma membrane and ER) or 3 μM pcDH (nucleus and mitochondria) in Dulbecco's Modified Eagle Medium (DMEM) for 1 h. Before imaging, the culture medium was replaced with HBSS (+). Fluorescence images were acquired every 30 s for 40 min

(plasma membrane, mitochondria, and ER) or every 1 min for 70 min (nucleus). Violet and green light illumination was performed with a multi-wavelength laser diode at 405 nm (60 μW for 100 ms) and 555 nm (1.1 mW for 500 ms), respectively. For the competition assay of TMP, 200 μL HBSS (+) containing 500 μM TMP (a final concentration of 50 μM) was added at 20 min. Fluorescence images were acquired every 30 s for 40 min.

For the kinetic analysis of the mitochondria recruitment, HeLa cells were plated at 5.0×10^4 cells per dish and transfected with the plasmids expressing eDHFR-miRFP670nano-NES and Tom20-mOrange2-Halo at a 2:3 ratio. After 36 h of transfection, the cells were washed twice with HBSS (+) and treated with 3 μM pcDH in DMEM for 1 h. Before imaging, the culture medium was replaced with HBSS (+). Fluorescence images were acquired every 300 ms for 30 s. Violet, green light illumination was performed with a multi-wavelength laser diode at 405 nm (60 μW for 100 ms) and 555 nm (1.4 mW for 100 ms), respectively.

To perform a quantitative protein translocation assay, HeLa cells were plated at 5.0×10^4 cells per dish and transfected with the plasmids expressing eDHFR-miRFP670nano-NES and Halo-mOrange2-CAAX at a 1:2 ratio. After 36 h of transfection, the cells were washed twice with HBSS (+) and treated with 5 μM pcDH in DMEM for 1 h. Before imaging, the culture medium was replaced with HBSS (+). Fluorescence images were acquired every 30 s for 45 min. Violet, blue, and green light illumination was performed with a multi-wavelength laser diode at 405 nm (60 μW for 100 ms), 445 nm (130 μW for 300 ms), and 555 nm (1.1 mW for 500 ms), respectively.

To examine photo-regulation of mitophagy by photochromic CID system, HeLa cells stably expressing Halo-OMP25 and mEGFP-rLC3B were plated at 4.0×10^4 cells per dish and transfected with the plasmids expressing cytPINK1-mOrange2-eDHFR and miRFP670nano-Parkin at a 3:5 ratio. After 36 h of transfection, the cells were washed twice with HBSS (+) and treated with 7 μM pcDH in DMEM for 30 min. Before imaging, the culture medium was replaced with flesh DMEM supplemented with 10%FBS. Fluorescence images were acquired every 1 min for 70 min. Violet and green light illumination was performed with a multi-wavelength laser diode at 405 nm (110 μW for 100 ms) and 555 nm (1.1 mW for 500 ms), respectively.

Analysis of recruitment of cytosolic protein

The regions of interest (ROIs) for nucleus and mitochondria were defined by thresholding the mOrange2 signals for the determination of fluorescence intensity in the organelles. PCC between eDHFR-miRFP670nano-NES and organelle-targeted Halo-mOrange2 was determined for individual cells using EzColocalization plugin on Fiji (Fiji is ImageJ).

Analysis of recruitment rate to mitochondria

Fluorescence intensities from ROIs defined by thresholding the Tom20-Halo-mOrange2 signals were used to be fitted to the following mono-exponential equation (3).

$$F = Ae^{-kt} + B \quad (3)$$

, where F is the fluorescence intensity in an ROI at time t, A and B are parameters, and k is the rate constant. The half-life, $t_{1/2}$, was determined by the equation (4).

$$t_{1/2} = \ln 2 / k \quad (4)$$

Statistical analysis and data visualization

Unless otherwise stated, most statistical analysis was done with unpaired, two-tailed Student's *t*-test with assuming equal distributions. A paired, two-tailed Student's *t*-test was used in Figure 3-7c.

^{1}H and ^{13}C NMR spectra

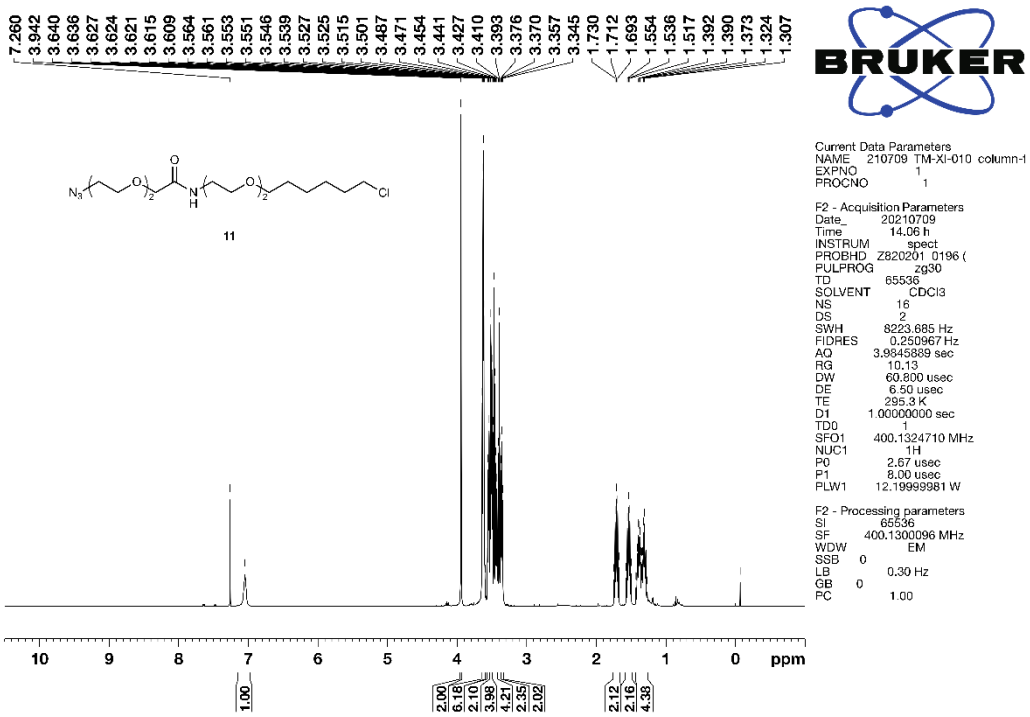

Figure S3-1. ^{1}H NMR spectrum of compound **11** (400 MHz, $CDCl_3$).

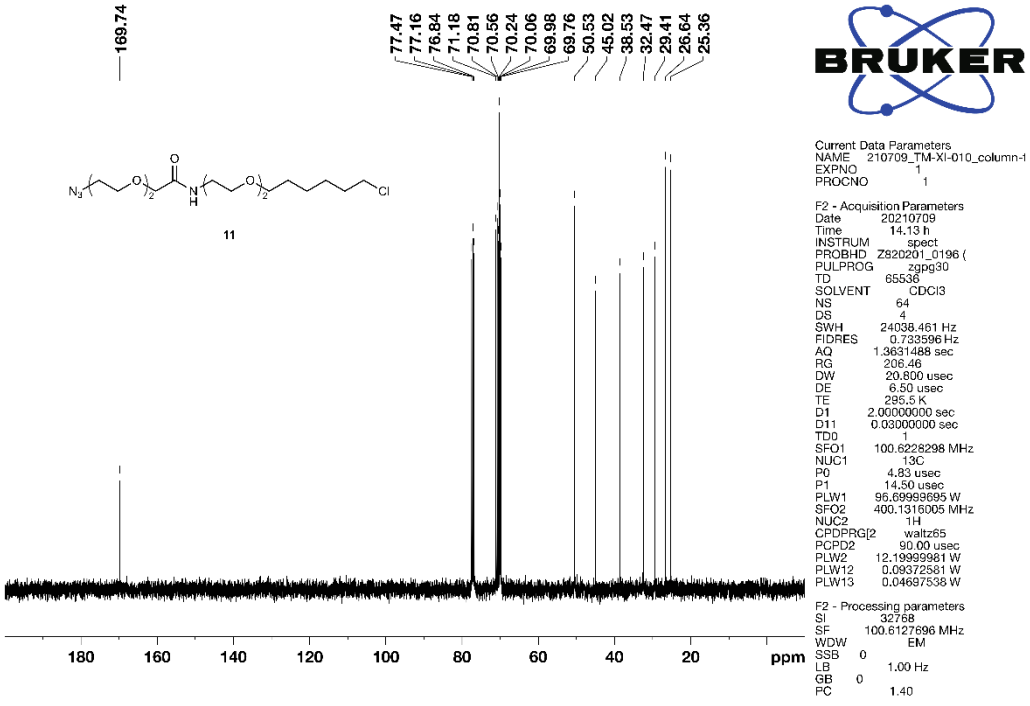

Figure S3-2. ^{13}C NMR spectrum of compound **11** (101 MHz, $CDCl_3$).

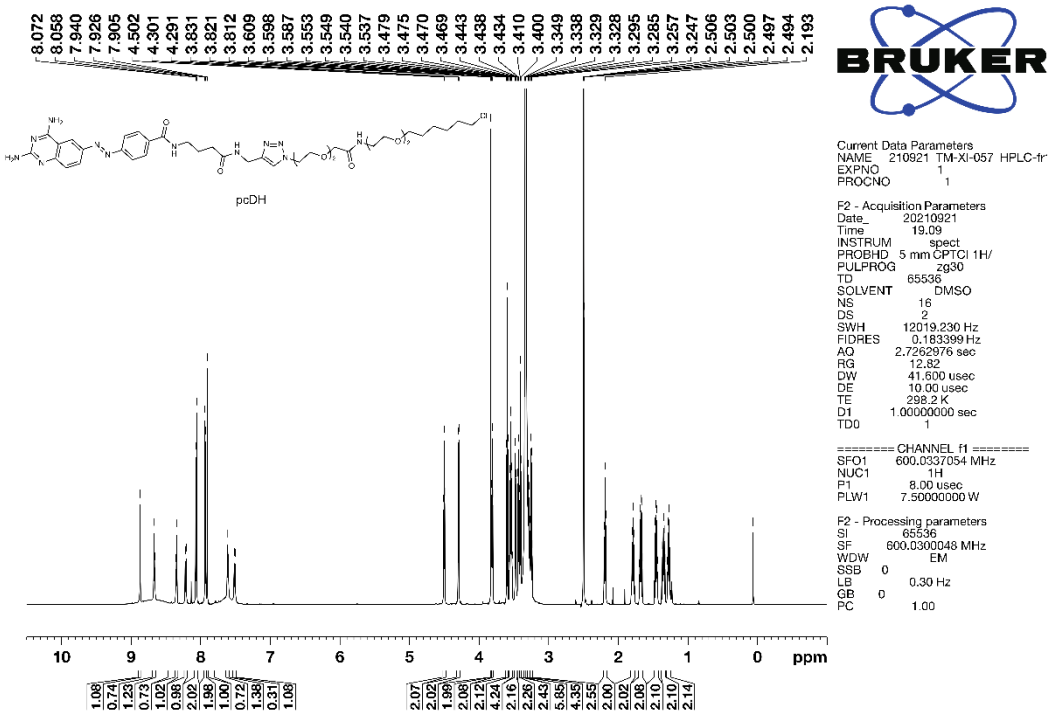

Figure S3-3. ^{1}H NMR spectrum of compound pcDH (600 MHz, DMSO-d_6).

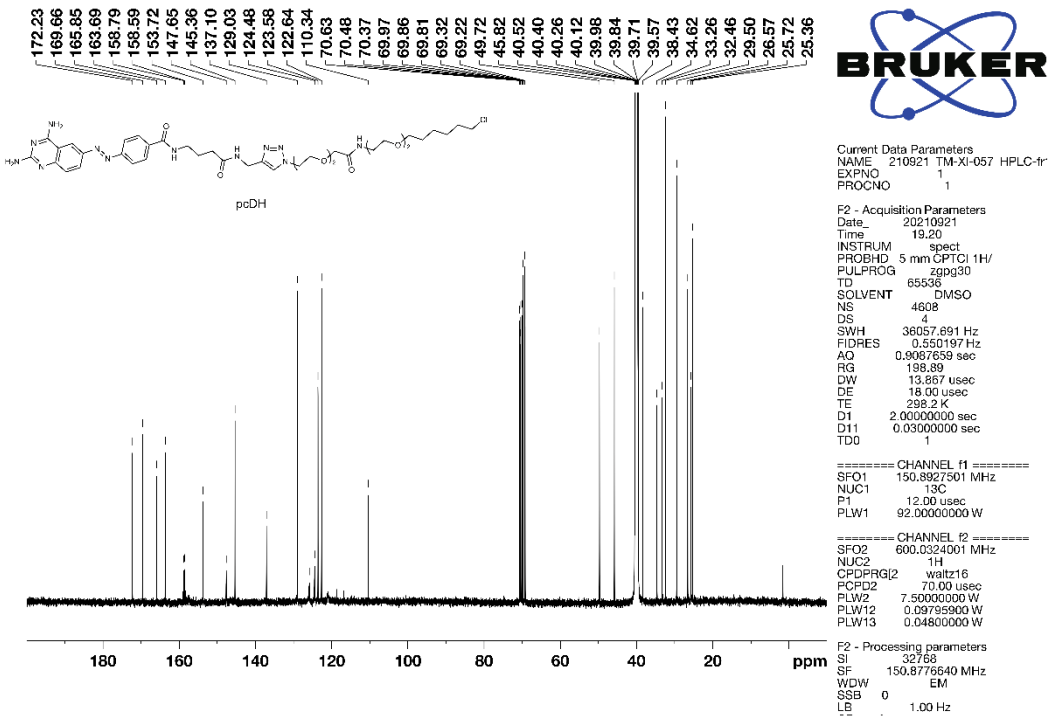

Figure S3-4. ^{13}C NMR spectrum of compound pcDH (151 MHz, DMSO-d_6).

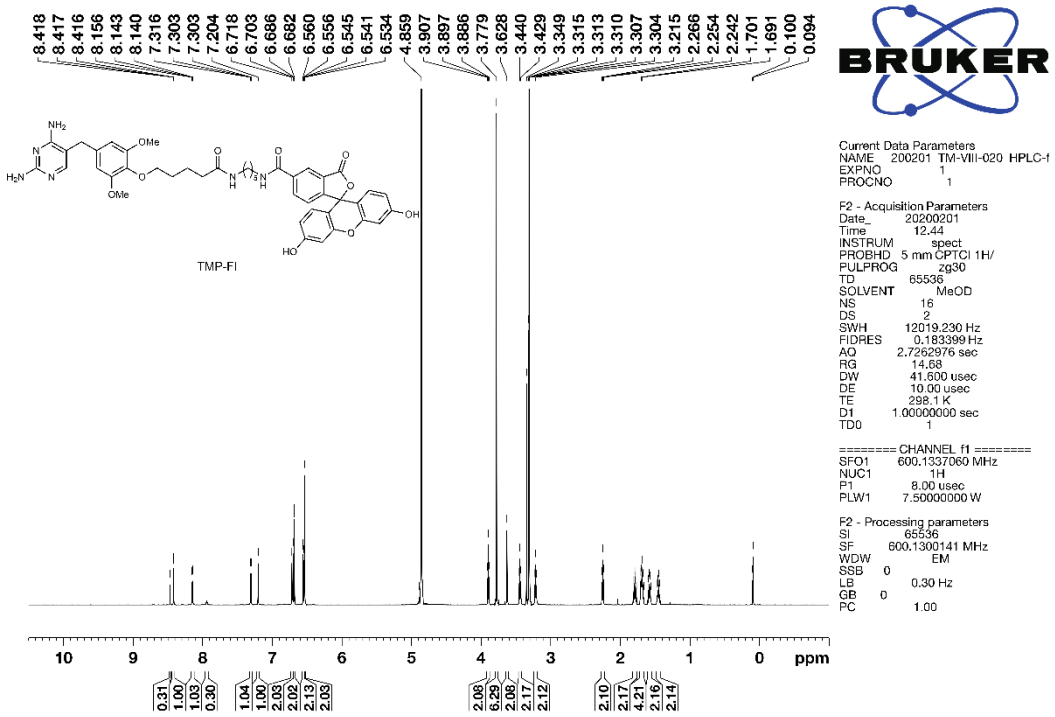

Figure S3-5. ^{1}H NMR spectrum of TMP-Fl (600 MHz, CD_3OD).

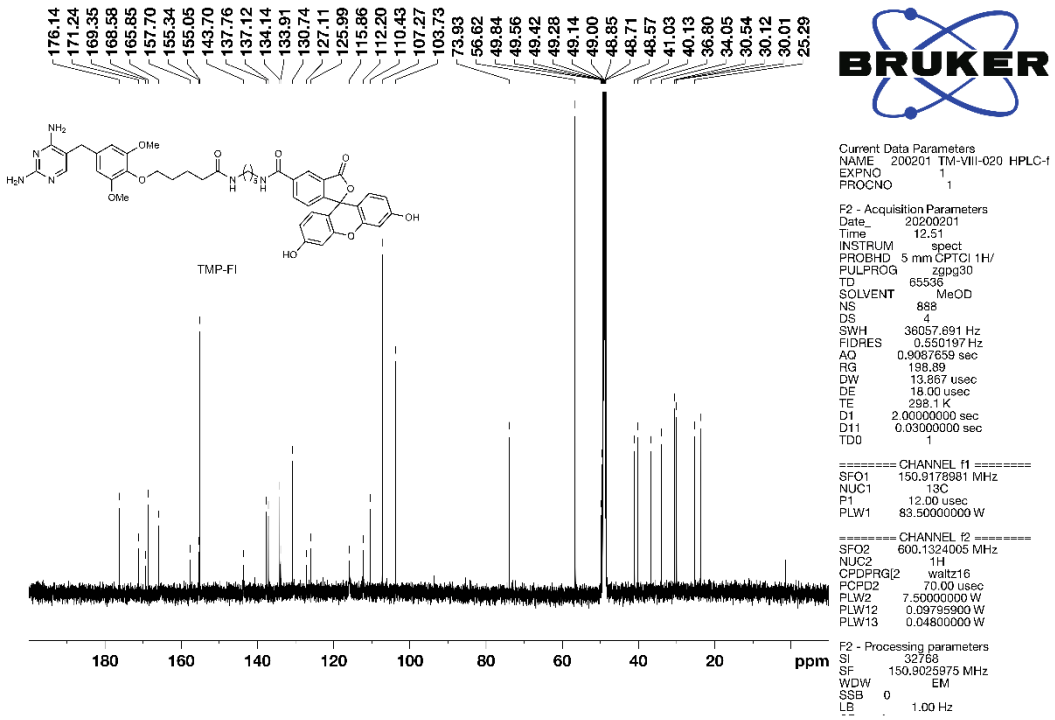

Figure S3-6. ^{13}C NMR spectrum of TMP-Fl (151 MHz, CD_3OD).

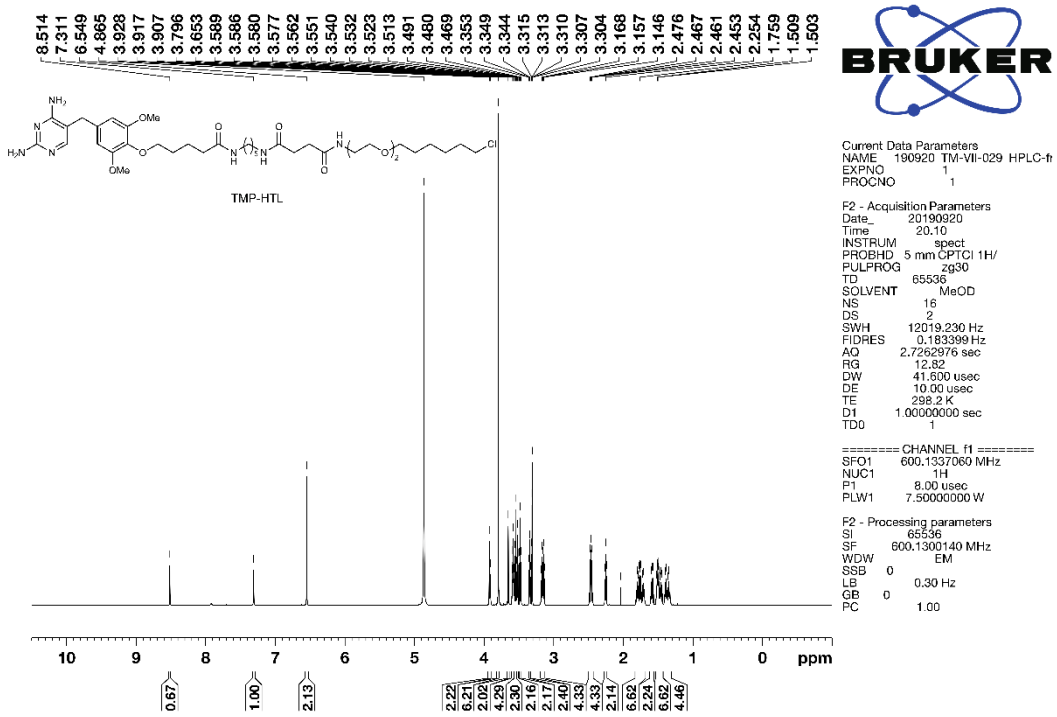

Figure S3-7. ^{1}H NMR spectrum of TMP-HTL (600 MHz, CD_3OD).

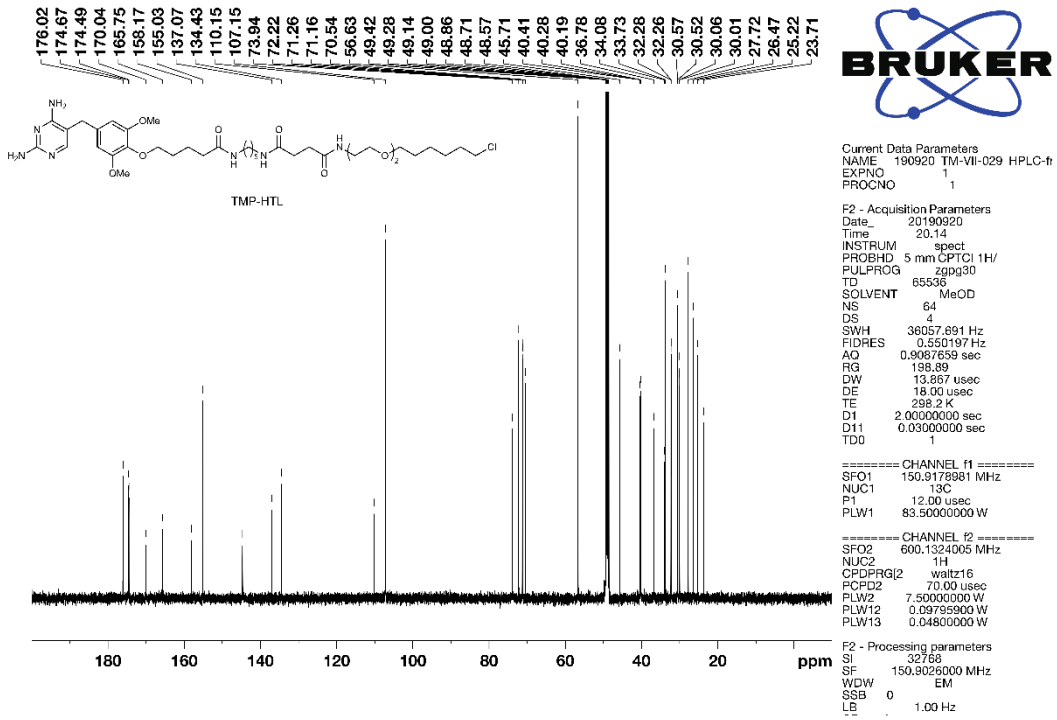

Figure S3-8. ^{13}C NMR spectrum of TMP-HTL (151 MHz, CD_3OD).

3-8. References (chapter 3)

1. Stanton, B. Z.; Chory, E. J.; Crabtree, G. R., Chemically induced proximity in biology and medicine. *Science* **2018,** *359* (6380), eaao5902.

2. Lavoie, H.; Therrien, M., Regulation of RAF protein kinases in ERK signalling. *Nat. Rev. Mol. Cell Biol.* **2015,** *16* (5), 281–298.

3. Tei, R.; Baskin, J. M., Induced proximity tools for precise manipulation of lipid signaling. *Curr. Opin. Chem. Biol.* **2021,** *65*, 93–100.

4. Passmore, J. B.; Nijenhuis, W.; Kapitein, L. C., From observing to controlling: Inducible control of organelle dynamics and interactions. *Curr. Opin. Cell Biol.* **2021,** *71*, 69–76.

5. Klewer, L.; Wu, Y.-W., Light-Induced Dimerization Approaches to Control Cellular Processes. *Chem. Eur. J.* **2019,** *25* (54), 12452–12463.

6. Kawano, F.; Suzuki, H.; Furuya, A.; Sato, M., Engineered pairs of distinct photoswitches for optogenetic control of cellular proteins. *Nat. Commun.* **2015,** *6* (1), 6256.

7. Guntas, G.; Hallett, R. A.; Zimmerman, S. P.; Williams, T.; Yumerefendi, H.; Bear, J. E.; Kuhlman, B., Engineering an improved light-induced dimer (iLID) for controlling the localization and activity of signaling proteins. *Proc. Natl. Acad. Sci. USA* **2015,** *112* (1), 112–117.

8. Kennedy, M. J.; Hughes, R. M.; Peteya, L. A.; Schwartz, J. W.; Ehlers, M. D.; Tucker, C. L., Rapid blue-light–mediated induction of protein interactions in living cells. *Nat. Methods* **2010,** *7* (12), 973–975.

9. Levskaya, A.; Weiner, O. D.; Lim, W. A.; Voigt, C. A., Spatiotemporal control of cell signalling using a light-switchable protein interaction. *Nature* **2009,** *461* (7266), 997–1001.

10. Farahani, P. E.; Reed, E. H.; Underhill, E. J.; Aoki, K.; Toettcher, J. E., Signaling, Deconstructed: Using Optogenetics to Dissect and Direct Information Flow in Biological Systems. *Annu. Rev. Biomed. Eng.* **2021,** *23* (1), 61–87.

11. Ma, G.; He, L.; Liu, S.; Xie, J.; Huang, Z.; Jing, J.; Lee, Y.-T.; Wang, R.; Luo, H.; Han, W.; Huang, Y.; Zhou, Y., Optogenetic engineering to probe the molecular choreography of STIM1-mediated cell signaling. *Nat. Commun.* **2020,** *11* (1), 1039.

12. Bugaj, L. J.; Sabnis, A. J.; Mitchell, A.; Garbarino, J. E.; Toettcher, J. E.; Bivona, T. G.; Lim, W. A., Cancer mutations and targeted drugs can disrupt dynamic signal encoding by the Ras-Erk pathway. *Science* **2018,** *361* (6405), eaao3048.

13. Toettcher, Jared E.; Weiner, Orion D.; Lim, Wendell A., Using Optogenetics to Interrogate the Dynamic Control of Signal Transmission by the Ras/Erk Module. *Cell* **2013,** *155* (6), 1422–1434.

14. Kaberniuk, A. A.; Shemetov, A. A.; Verkhusha, V. V., A bacterial phytochrome-based optogenetic system controllable with near-infrared light. *Nat. Methods* **2016,** *13* (7), 591–597.

15. Toettcher, J. E.; Gong, D.; Lim, W. A.; Weiner, O. D., Light-based feedback for controlling intracellular signaling dynamics. *Nat. Methods* **2011,** *8* (10), 837–839.

16. Taslimi, A.; Zoltowski, B.; Miranda, J. G.; Pathak, G. P.; Hughes, R. M.; Tucker, C. L., Optimized second-generation CRY2–CIB dimerizers and photoactivatable Cre recombinase. *Nat. Chem. Biol.* **2016,** *12* (6), 425–430.

17. Hallett, R. A.; Zimmerman, S. P.; Yumerefendi, H.; Bear, J. E.; Kuhlman, B., Correlating in Vitro and in Vivo Activities of Light-Inducible Dimers: A Cellular Optogenetics Guide. *ACS Synth. Biol.* **2016,** *5* (1), 53–64.
18. Rutkowska, A.; Schultz, C., Protein Tango: The Toolbox to Capture Interacting Partners. *Angew. Chem. Int. Ed.* **2012,** *51* (33), 8166–8176.
19. Belshaw, P. J.; Ho, S. N.; Crabtree, G. R.; Schreiber, S. L., Controlling protein association and subcellular localization with a synthetic ligand that induces heterodimerization of proteins. *Proc. Natl. Acad. Sci. USA* **1996,** *93* (10), 4604–4607.
20. Voß, S.; Klewer, L.; Wu, Y.-W., Chemically induced dimerization: reversible and spatiotemporal control of protein function in cells. *Curr. Opin. Chem. Biol.* **2015,** *28*, 194–201.
21. Brown, K. A.; Zou, Y.; Shirvanyants, D.; Zhang, J.; Samanta, S.; Mantravadi, P. K.; Dokholyan, N. V.; Deiters, A., Light-cleavable rapamycin dimer as an optical trigger for protein dimerization. *Chem. Commun.* **2015,** *51* (26), 5702–5705.
22. Karginov, A. V.; Zou, Y.; Shirvanyants, D.; Kota, P.; Dokholyan, N. V.; Young, D. D.; Hahn, K. M.; Deiters, A., Light Regulation of Protein Dimerization and Kinase Activity in Living Cells Using Photocaged Rapamycin and Engineered FKBP. *J. Am. Chem. Soc.* **2011,** *133* (3), 420–423.
23. Kowada, T.; Arai, K.; Yoshimura, A.; Matsui, T.; Kikuchi, K.; Mizukami, S., Optical Manipulation of Subcellular Protein Translocation Using a Photoactivatable Covalent Labeling System. *Angew. Chem. Int. Ed.* **2021,** *60* (20), 11378–11383.
24. Zimmermann, M.; Cal, R.; Janett, E.; Hoffmann, V.; Bochet, C. G.; Constable, E.; Beaufils, F.; Wymann, M. P., Cell-Permeant and Photocleavable Chemical Inducer of Dimerization. *Angew. Chem. Int. Ed.* **2014,** *53* (18), 4717–4720.
25. Ballister, E. R.; Aonbangkhen, C.; Mayo, A. M.; Lampson, M. A.; Chenoweth, D. M., Localized light-induced protein dimerization in living cells using a photocaged dimerizer. *Nat. Commun.* **2014,** *5* (1), 5475.
26. Chen, X.; Wu, Y.-W., Tunable and Photoswitchable Chemically Induced Dimerization for Chemo-optogenetic Control of Protein and Organelle Positioning. *Angew. Chem. Int. Ed.* **2018,** *57* (23), 6796–6799.
27. Aonbangkhen, C.; Zhang, H.; Wu, D. Z.; Lampson, M. A.; Chenoweth, D. M., Reversible Control of Protein Localization in Living Cells Using a Photocaged-Photocleavable Chemical Dimerizer. *J. Am. Chem. Soc.* **2018,** *140* (38), 11926–11930.
28. Zhang, H.; Aonbangkhen, C.; Tarasovetc, E. V.; Ballister, E. R.; Chenoweth, D. M.; Lampson, M. A., Optogenetic control of kinetochore function. *Nat. Chem. Biol.* **2017,** *13* (10), 1096–1101.
29. Akera, T.; Chmátal, L.; Trimm, E.; Yang, K.; Aonbangkhen, C.; Chenoweth, D. M.; Janke, C.; Schultz, R. M.; Lampson, M. A., Spindle asymmetry drives non-Mendelian chromosome segregation. *Science* **2017,** *358* (6363), 668–672.
30. Los, G. V.; Encell, L. P.; McDougall, M. G.; Hartzell, D. D.; Karassina, N.; Zimprich, C.; Wood, M. G.; Learish, R.; Ohana, R. F.; Urh, M.; Simpson, D.; Mendez, J.; Zimmerman, K.; Otto, P.; Vidugiris, G.;

Zhu, J.; Darzins, A.; Klaubert, D. H.; Bulleit, R. F.; Wood, K. V., HaloTag: A Novel Protein Labeling Technology for Cell Imaging and Protein Analysis. *ACS Chem. Biol.* **2008,** *3* (6), 373–382.
31. Baccanari, D. P.; Daluge, S.; King, R. W., Inhibition of dihydrofolate reductase: effect of NADPH on the selectivity and affinity of diaminobenzylpyrimidines. *Biochemistry* **1982,** *21* (20), 5068–5075.
32. Benedetti, L.; Barentine, A. E. S.; Messa, M.; Wheeler, H.; Bewersdorf, J.; De Camilli, P., Light-activated protein interaction with high spatial subcellular confinement. *Proc. Natl. Acad. Sci. USA* **2018,** *115* (10), E2238–E2245.
33. Benedetti, L.; Marvin, J. S.; Falahati, H.; Guillén-Samander, A.; Looger, L. L.; De Camilli, P., Optimized Vivid-derived Magnets photodimerizers for subcellular optogenetics in mammalian cells. *eLife* **2020,** *9*, e63230.
34. Cohen-Saidon, C.; Cohen, A. A.; Sigal, A.; Liron, Y.; Alon, U., Dynamics and Variability of ERK2 Response to EGF in Individual Living Cells. *Mol. Cell* **2009,** *36* (5), 885–893.
35. Sugiura, A.; McLelland, G.-L.; Fon, E. A.; McBride, H. M., A new pathway for mitochondrial quality control: mitochondrial-derived vesicles. *EMBO J.* **2014,** *33* (19), 2142–2156.
36. Ordureau, A.; Sarraf, Shireen A.; Duda, David M.; Heo, J.-M.; Jedrychowski, Mark P.; Sviderskiy, Vladislav O.; Olszewski, Jennifer L.; Koerber, James T.; Xie, T.; Beausoleil, Sean A.; Wells, James A.; Gygi, Steven P.; Schulman, Brenda A.; Harper, J. W., Quantitative Proteomics Reveal a Feedforward Mechanism for Mitochondrial PARKIN Translocation and Ubiquitin Chain Synthesis. *Mol. Cell* **2014,** *56* (3), 360–375.
37. Kane, L. A.; Lazarou, M.; Fogel, A. I.; Li, Y.; Yamano, K.; Sarraf, S. A.; Banerjee, S.; Youle, R. J., PINK1 phosphorylates ubiquitin to activate Parkin E3 ubiquitin ligase activity. *J. Cell Biol.* **2014,** *205* (2), 143–153.
38. Lazarou, M.; Jin, Seok M.; Kane, Lesley A.; Youle, Richard J., Role of PINK1 Binding to the TOM Complex and Alternate Intracellular Membranes in Recruitment and Activation of the E3 Ligase Parkin. *Dev. Cell* **2012,** *22* (2), 320–333.
39. Narendra, D. P.; Jin, S. M.; Tanaka, A.; Suen, D.-F.; Gautier, C. A.; Shen, J.; Cookson, M. R.; Youle, R. J., PINK1 Is Selectively Stabilized on Impaired Mitochondria to Activate Parkin. *PLoS Biol.* **2010,** *8* (1), e1000298.
40. Kabeya, Y.; Mizushima, N.; Ueno, T.; Yamamoto, A.; Kirisako, T.; Noda, T.; Kominami, E.; Ohsumi, Y.; Yoshimori, T., LC3, a mammalian homologue of yeast Apg8p, is localized in autophagosome membranes after processing. *EMBO J.* **2000,** *19* (21), 5720–5728.
41. Lazarou, M.; Sliter, D. A.; Kane, L. A.; Sarraf, S. A.; Wang, C.; Burman, J. L.; Sideris, D. P.; Fogel, A. I.; Youle, R. J., The ubiquitin kinase PINK1 recruits autophagy receptors to induce mitophagy. *Nature* **2015,** *524* (7565), 309–314.
42. Bingol, B.; Tea, J. S.; Phu, L.; Reichelt, M.; Bakalarski, C. E.; Song, Q.; Foreman, O.; Kirkpatrick, D. S.; Sheng, M., The mitochondrial deubiquitinase USP30 opposes parkin-mediated mitophagy. *Nature* **2014,** *510* (7505), 370–375.
43. Harper, J. W.; Ordureau, A.; Heo, J.-M., Building and decoding ubiquitin chains for mitophagy. *Nat.*

Rev. Mol. Cell Biol. **2018,** *19* (2), 93–108.

44. Okatsu, K.; Oka, T.; Iguchi, M.; Imamura, K.; Kosako, H.; Tani, N.; Kimura, M.; Go, E.; Koyano, F.; Funayama, M.; Shiba-Fukushima, K.; Sato, S.; Shimizu, H.; Fukunaga, Y.; Taniguchi, H.; Komatsu, M.; Hattori, N.; Mihara, K.; Tanaka, K.; Matsuda, N., PINK1 autophosphorylation upon membrane potential dissipation is essential for Parkin recruitment to damaged mitochondria. *Nat. Commun.* **2012,** *3* (1), 1016.

45. Keppler, A.; Gendreizig, S.; Gronemeyer, T.; Pick, H.; Vogel, H.; Johnsson, K., A general method for the covalent labeling of fusion proteins with small molecules in vivo. *Nat. Biotechnol.* **2003,** *21* (1), 86–89.

46. Miller, L. W.; Cai, Y.; Sheetz, M. P.; Cornish, V. W., In vivo protein labeling with trimethoprim conjugates: a flexible chemical tag. *Nat. Methods* **2005,** *2* (4), 255–257.

47. Bonger, K. M.; van den Berg, R. J. B. H. N.; Knijnenburg, A. D.; Heitman, L. H.; Ijzerman, A. P.; Oosterom, J.; Timmers, C. M.; Overkleeft, H. S.; van der Marel, G. A., Synthesis and evaluation of homodimeric GnRHR antagonists having a rigid bis-propargylated benzene core. *Biorg. Med. Chem.* **2008,** *16* (7), 3744–3758.

48. Singh, V.; Wang, S.; Chan, K. M.; Clark, S. A.; Kool, E. T., Genetically encoded multispectral labeling of proteins with polyfluorophores on a DNA backbone. *J. Am. Chem. Soc.* **2013,** *135* (16), 6184–91.

49. Sato, R.; Kozuka, J.; Ueda, M.; Mishima, R.; Kumagai, Y.; Yoshimura, A.; Minoshima, M.; Mizukami, S.; Kikuchi, K., Intracellular Protein-Labeling Probes for Multicolor Single-Molecule Imaging of Immune Receptor-Adaptor Molecular Dynamics. *J. Am. Chem. Soc.* **2017,** *139* (48), 17397–17404.

50. Newton, A. S.; Deiana, L.; Puleo, D. E.; Cisneros, J. A.; Cutrona, K. J.; Schlessinger, J.; Jorgensen, W. L., JAK2 JH2 Fluorescence Polarization Assay and Crystal Structures for Complexes with Three Small Molecules. *ACS Med. Chem. Lett.* **2017,** *8* (6), 614–617.

51. Ando, T.; Tsukiji, S.; Tanaka, T.; Nagamune, T., Construction of a small-molecule-integrated semisynthetic split intein for in vivoprotein ligation. *Chem. Commun.* **2007,** (47), 4995–4997.

52. Takaoka, Y.; Nishikawa, Y.; Hashimoto, Y.; Sasaki, K.; Hamachi, I., Ligand-directed dibromophenyl benzoate chemistry for rapid and selective acylation of intracellular natural proteins. *Chem. Sci.* **2015,** *6* (5), 3217–3224.

53. Nikolovska-Coleska, Z.; Wang, R.; Fang, X.; Pan, H.; Tomita, Y.; Li, P.; Roller, P. P.; Krajewski, K.; Saito, N. G.; Stuckey, J. A.; Wang, S., Development and optimization of a binding assay for the XIAP BIR3 domain using fluorescence polarization. *Anal. Biochem.* **2004,** *332* (2), 261–273.

54. Mashita, T.; Kowada, T.; Takahashi, H.; Matsui, T.; Mizukami, S., Light-Wavelength-Based Quantitative Control of Dihydrofolate Reductase Activity by Using a Photochromic Isostere of an Inhibitor. *ChemBioChem* **2019,** *20* (11), 1382–1386.

55. Xu, D.; Farmer, A.; Collett, G.; Grishin, N. V.; Chook, Y. M., Sequence and structural analyses of nuclear export signals in the NESdb database. *Mol. Biol. Cell* **2012,** *23* (18), 3677–3693.

56. Kalderon, D.; Roberts, B. L.; Richardson, W. D.; Smith, A. E., A short amino acid sequence able to specify nuclear location. *Cell* **1984,** *39* (3), 499–509.

57. Choy, E.; Chiu, V. K.; Silletti, J.; Feoktistov, M.; Morimoto, T.; Michaelson, D.; Ivanov, I. E.; Philips,

M. R., Endomembrane Trafficking of Ras: The CAAX Motif Targets Proteins to the ER and Golgi. *Cell* **1999,** *98* (1), 69–80.

58. Komatsu, T.; Kukelyansky, I.; McCaffery, J. M.; Ueno, T.; Varela, L. C.; Inoue, T., Organelle-specific, rapid induction of molecular activities and membrane tethering. *Nat. Methods* **2010,** *7* (3), 206–208.

59. Kanaji, S.; Iwahashi, J.; Kida, Y.; Sakaguchi, M.; Mihara, K., Characterization of the Signal That Directs Tom20 to the Mitochondrial Outer Membrane. *J. Cell Biol.* **2000,** *151* (2), 277–288.

CHAPTER 4

Enhancement of the Difference in Affinity between *E* and *Z* Isomers by Engineering the Tag Protein

4-1. Introduction

The author has developed a photo-reversible ligand, azoMTX, which binds to eDHFR in a photo-reversible manner in chapter 2. Violet light irradiation, typically at 394 nm, isomerized azoMTX from *E* isomer to *Z* isomer, whereas green light, typically at 560 nm, induces the reverse isomerization from *Z* to *E*. Since (*Z*)-azoMTX had a higher affinity to eDHFR than *E* isomer, azoMTX was associated with and dissociated from eDHFR repeatedly by alternating irradiation with different wavelengths of light. Moreover, utilization of an azoMTX derivative as a photochromic ligand for eDHFR has allowed quick and repetitive regulation of intracellular protein dynamics upon light illumination, as demonstrated in chapter 3. This photochromic CID system has the potential to finely manipulate intracellular protein dynamics for research on diverse cellular processes.

On the other hand, the author found two problems that should be improved. One is the basal localization of the cytosolic protein to the organelles. When sufficient translocation of the target protein is desired, a sufficient amount of the photochromic dimerizer needs to be added. Under such conditions, the cytosolic eDHFR-fused target protein was partially localized to the HaloTag-expressing regions even before violet light illumination and after green light illumination. That could be due to the high affinity of the *E* isomer toward eDHFR. Although such basal localization was suppressed by reducing the concentration of the photochromic ligand, light-dependent translocation turned faint by the reduction. Since the bound fraction relies upon the ligand binding affinity after light irradiation (Figure 4-1),[1] this small dynamic range of the translocation is attributed to the small difference in the affinity of azoMTX before and after light irradiation. Hence, the author addressed the enhancement of fold difference in ligand binding affinity in this chapter.

To enhance the fold difference in binding affinity, the author tried to reduce the affinity of *E* isomer to eDHFR by mutation of the protein. The author performed a docking simulation to find promising candidates of amino acids to enhance the affinity difference between E and Z isomers. Next, recombinant eDHFR mutated on the amino acids was evaluated by the fluorescence depolarization assay, and a few mutants provided larger fold enhancement in the ligand-binding affinity after light irradiation than

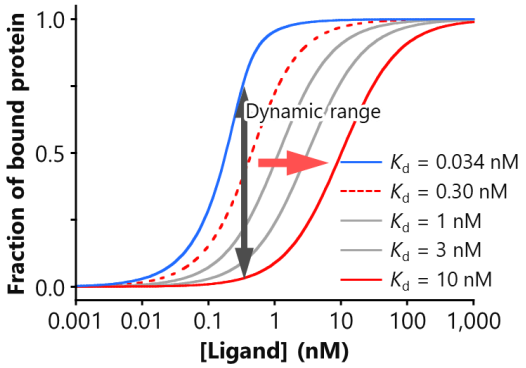

Figure 4-1. Simulation for the changes in fraction bound eDHFR as a function of ligand concentration due to different fold changes in ligand binding affinity before and after light.

wild type.

4-2. Design of mutant eDHR by docking simulation

The author first performed a docking simulation of azoMTX and eDHFR using AutoDock4. The results of docking simulations are shown in Figure 4-2. These results indicate that (*Z*)-azoMTX bind to eDHFR at a deep position in the binding pocket. On the other hand, (*E*)-azoMTX is likely to bind along with the edge of the pocket. The author accordingly predicted that mutation at the amino acids located along with the binding pocket, especially F31, S49, I50, may reduce the affinity of *E* isomer.

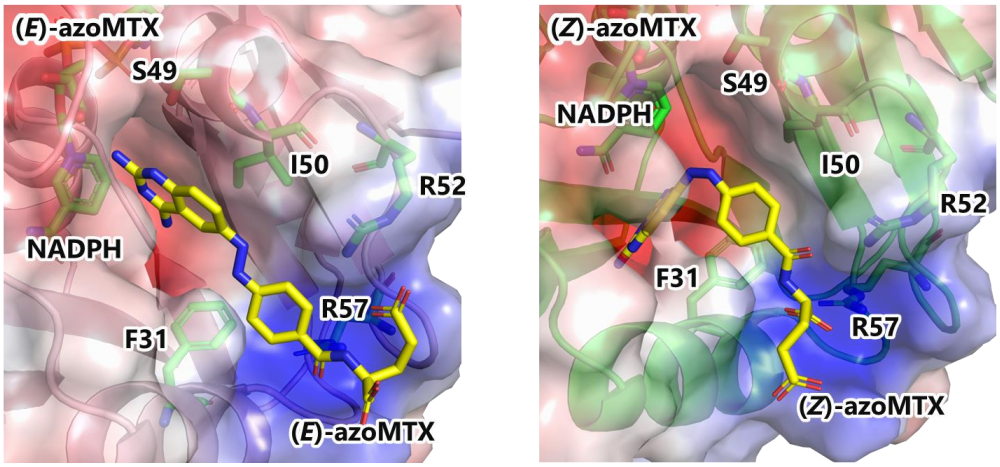

Figure 4-2. Docking simulation of *E* (left) and *Z* (right) isomers of azoMTX. Introduction of mutation to the residues surrounding azoMTX binding pocket may reduce the affinity between eDHFR and (*E*)-azoMTX. Docking simulation was performed by AutoDock4.

4-3. Binding assay between mutant eDHFR and azoMTX

The site-directed mutagenesis was performed by inverse-PCR with proper primers, and recombinant mutant protein was obtained and purified with polyhistidine-tag attached on the *N*-terminus of eDHFR. The ligand binding affinities were estimated by competitive fluorescence polarization assay with a fluorophore-conjugated TMP (TMP-Fl, scheme S3-2). Applying the obtained IC_{50} values to Nikolovska-Coleska[2] equation with the predetermined dissociation constant (K_d) of TMP-Fl to each eDHFR (summarized in Tables 4-1,2,3), the K_ds of both azoMTX isomers were estimated and summarized in Tables 4-1,2,3. In the wild type, the difference was about 7-fold. In the F31I mutant, however, the difference between the two isomers was 16-fold, and in I50T, the difference was 34-fold. These results suggest that mutation at the amino acids located along the binding pocket affects the affinity difference. Although the reason for the enhancement of affinity difference is unknown, the author expects that the I50T mutant enhances the dynamic range of photo-regulation of intracellular protein translocation. This enhancement of dynamic range will likely suppress basal translocation of cytosolic eDHFR and provide a clearer ON/OFF switch. Moreover, the author believes that further screening will enhance the affinity difference between two isomers.

Table 4-1. K_d values between azoMTX and mutant His_6-tev-eDHFR(F31X)

Mutation	WT	F31L	F31I	F31C	F31T	F31H	F31A	F31S
Dark (*E* isomer) /nM	11	5.0	59	26	49	150	105	424
PSS_{394} (*Z* isomer) /nM	1.6	N.D.	3.8	4.4	7.1	44	13	92
K_d ratio (*E* isomer/*Z* isomer)	6.9	–	15.5	5.8	6.9	3.3	8.0	4.6
K_d(TMP-Fl) /nM	4.0	7.2	59	13	26	11	25	40

N.D.: K_d value could not be calculated from IC_{50} value. All K_d values were determined at 37 °C.

Table 4-2. K_d values between azoMTX and mutant His_6-tev-eDHFR(I50X)

Mutation	WT	I50A	I50N	I50S	I50T	I50P	I50D
Dark (*E* isomer) /nM	11	13	65	48	26	208	83
PSS_{394} (*Z* isomer) /nM	1.6	N.D.	9.6	2.6	0.78	34	18
K_d ratio (*E* isomer/*Z* isomer)	6.9	—	6.8	18	34	6.1	4.6
K_d(TMP-Fl) /nM	4.0	19	46	44	19	90	11

N.D.: K_d value could not be calculated from IC_{50} value. All K_d values were determined at 37 °C.

Table 4-3. K_d values between azoMTX and mutant His_6-tev-eDHFR(S49X)

Mutation	WT	S49F	S49W	S49M
Dark (*E* isomer) /nM	11	3.5	1.8	2.5
PSS_{394} (*Z* isomer) /nM	1.6	0.54	N.D.	0.42
K_d ratio (*E* isomer/*Z* isomer)	6.9	6.5	—	5.9
K_d(TMP-Fl) /nM	4.0	1.0	2.4	2.5

N.D.: K_d value could not be calculated from IC_{50} value. All K_d values were determined at 37 °C.

4-4. Conclusion

In chapter 4, the author addressed the enhancement of fold difference in ligand binding affinity. To enhance the fold difference in binding affinity, the author tried to reduce the affinity of *E* isomer to eDHFR by mutation of the protein. Docking simulation indicated that (*Z*)-azoMTX bind to eDHFR at a deep position in the binding pocket, while (*E*)-azoMTX is likely to bind along with the edge of the pocket. According to this insight, mutation at the amino acids located along the binding pocket, especially F31, S49, I50, was performed. The binding assay showed that F31I had a 16-fold enhancement of affinity upon light irradiation, and I50T had a 34-fold enhancement. The author focused on the pocket where azoMTX binds and worked to expand the difference in affinity between trans and cis forms by creating mutants of eDHFR. Utilization of these mutant eDHFRs may enhance the dynamic range of photo-regulation of intracellular protein translocation. This enhancement of dynamic range will likely suppress basal translocation of cytosolic eDHFR and provide a clearer ON/OFF switch than wild type. Moreover, further screening, including double or triple mutation, will presumably enhance the affinity difference between the two isomers.

4-5. Experimental section (chapter 4)

Docking simulation

Docking simulation was performed using AutoDock4 according to the reported protocol.[3] The crystal structure of eDHFR (PDB: 1RX3) was used for the receptor coordinate files, and the ligand structure was optimized using Molecular mechanics.

Construction of expression vectors for mutant eDHFR

The plasmids for recombinant eDHFR expression were prepared according to a method described previously.[4] Site-directed mutagenesis was performed using KOD -Plus- Mutagenesis Kit (Takara) according to the manufacturer's protocols. All plasmids were verified by Sanger sequencing.

Preparation of mutant eDHFR

E. coli strain BL21(DE3) (Nippon Gene) was transformed with pET28tev-eDHFR and grown at 37 °C in LB medium (Becton, Dickinson) containing 20 μg mL^{-1} kanamycin. When OD_{600} reached 0.7, IPTG (final concentration: 0.1 mM) was added to induce eDHFR at 25 °C. After an overnight induction, the cells were harvested by centrifugation at 6,500 × *g* for 20 min. The cell pellet was lysed with 3 mL EzBactYeast Crusher (ATTO). After the lysate was centrifuged at 15,000 × *g* for 30 min, the supernatant was loaded on a HisTrap HP column (GE Healthcare), equilibrated with Buffer A (20 mM Tris-HCl, pH 7.4, 350 mM NaCl, and 10% glycerol) containing 10 mM imidazole. The His-tagged eDHFR was eluted using an imidazole gradient from 10 to 270 mM in Buffer B. The appropriate fractions were collected and repeatedly ultra-filtered (Amicon Ultra-4, cut off 10 kDa, Millipore) for buffer exchange to Buffer B (20 mM HEPES-NaOH, pH 7.4 and 10% glycerol). The concentrated protein was stored at −80 °C until use. The concentration of eDHFR was calculated from the absorbance at 280 nm (ε_{280} = 39.0 mM^{-1} cm^{-1}), which is determined by fluorescence titration with MTX.[5]

Binding assay

Competitive binding assays for azoMTX at dark state, and azoMTX at PSS_{394} toward eDHFR were carried out using eDHFR bound with TMP-Fl in 100 mM HEPES-NaOH buffer (pH 7.4) containing 100 mM NaCl at 25 °C. AzoMTX at PSS_{394} was irradiated with 394/10 nm light at 5.0 mW cm^{-2} for 5 min just before the assay. The IC_{50} values were determined from the plot using nonlinear least-squares analysis. The dissociation constant (K_d) was calculated from the determined IC_{50} value using Nikolovska-Coleska equation.[2]

4-6. References (chapter 4)

1. Niu, J.; Ben Johny, M.; Dick, Ivy E.; Inoue, T., Following Optogenetic Dimerizers and Quantitative Prospects. *Biophys. J.* **2016,** *111* (6), 1132–1140.

2. Nikolovska-Coleska, Z.; Wang, R.; Fang, X.; Pan, H.; Tomita, Y.; Li, P.; Roller, P. P.; Krajewski, K.; Saito, N. G.; Stuckey, J. A.; Wang, S., Development and optimization of a binding assay for the XIAP BIR3 domain using fluorescence polarization. *Anal. Biochem.* **2004,** *332* (2), 261–273.

3. Forli, S.; Huey, R.; Pique, M. E.; Sanner, M. F.; Goodsell, D. S.; Olson, A. J., Computational protein–ligand docking and virtual drug screening with the AutoDock suite. *Nat. Protoc.* **2016,** *11* (5), 905–919.

4. Mashita, T.; Kowada, T.; Takahashi, H.; Matsui, T.; Mizukami, S., Light-Wavelength-Based Quantitative Control of Dihydrofolate Reductase Activity by Using a Photochromic Isostere of an Inhibitor. *ChemBioChem* **2019,** *20* (11), 1382–1386.

5. Cameron, C. E.; Benkovic, S. J., Evidence for a Functional Role of the Dynamics of Glycine-121 of Escherichia coli Dihydrofolate Reductase Obtained from Kinetic Analysis of a Site-Directed Mutant. *Biochemistry* **1997,** *36* (50), 15792–15800.

CHAPTER 5

Photochromic Ligand with Excellent Photoisomerization Property Based on Five-membered Heterocycle

5-1. Introduction

Optical control of biomolecular functions has attracted attention as a powerful approach to reveal the mechanisms of biological processes.[1-3] One of the promising approaches is the use of caged compounds, which have allowed the optical controls of diverse biomolecules,[4] such as ATP[5] and glutamate.[6] Caged compounds are inactivated by the modification of a photolabile group that inhibits the critical interactions with the target biomolecules and recover their activities when the photolabile group is removed by light irradiation. Recently, the introduction of a photolabile group on protein labeling systems has been reported by several groups, and these systems have allowed the regulation of various cellular events in a light-dependent manner.[7-10] One of the most widely used photo-activatable protein labeling systems is exploiting a pair of *Escherichia coli* dihydrofolate reductase (eDHFR) and a caged derivative of its selective inhibitor trimethoprim (TMP).[11-14] Since the affinity of the caged TMP to eDHFR is much lower than that of TMP, this caged ligand does not bind to eDHFR until the uncaging by the light irradiation.[15] Using this system as a chemical-biology tool, the molecular mechanisms of various cellular events have been so far revealed in a subcellular region level,[16] yet it is difficult to apply the caged TMP for repetitive control of biomolecular functions because of its irreversibility.

Another approach to optically control biomolecular functions is the utilization of photochromic compounds, which reversibly isomerize or convert their conformation upon light.[16, 17] This approach, often called photopharmacology, has allowed the repetitive control of biomolecular functions in both activation and inactivation by light. In most cases, an azobenzene moiety was incorporated in or attached to the known bioactive molecules, and various enzyme activities and cellular responses were photo-reversibly controlled.[18-211] Feringa et al. have developed diaminopyrimidines bearing azobenzene photo-switches to achieve the *in situ* photo-control of antibacterial activity.[22] On the basis of the similar strategy, the author previously developed a photo-switchable eDHFR inhibitor, named azoMTX (Figure 5-1a), which is a photopharmacological analog of methotrexate (MTX), one of the established DHFR inhibitors. AzoMTX reversibly isomerized upon light irradiation and optically controlled the enzymatic activity of eDHFR in real time.[22] This suggested a future prospect that various biomolecular functions can be photo-reversibly controlled through the use of azoMTX for protein labeling instead of the caged TMP.

However, Gorostiza et al. reported phototrexate (PTX), which is coincidentally identical to azoMTX, for optical control of human DHFR (hDHFR) activity to aim targeted anticancer photochemotherapy.[23] This indicates that azoMTX (or PTX) binds to both eDHFR and hDHFR. Since

inhibition of hDHFR leads to cell death, this poor selectivity would hinder the application of azoMTX as a versatile optochemical biology tool, such as a photo-switchable protein labeling system in mammalian cells. Hence, in this chapter, the author aimed to develop photo-switchable inhibitors that selectively bind to eDHFR while improving the photo-physical property of azoMTX.

5-2. Design of new photochromic ligands for eDHFR

The crystal structures of both hDHFR and eDHFR complexes with MTX and NADPH (PDB code: 1RX3 for eDHFR and 1U72 for hDHFR, Figure 5-1 lower panel) indicate that the bent form of MTX appears to be critical for its specific binding to DHFRs.[22] The author also found that eDHFR has a wider substrate–binding pocket than hDHFR. The author assumed that the introduction of bulky groups at the ortho-positions from the azo group on the phenyl ring of azoMTX might produce selectivity of binding towards eDHFR. In addition, the author considered to use an arylazopyrazole skeleton because recently arylazopyraozles have attracted huge attention as a novel class of azo photo-switches that show nearly quantitative *Z*-to-*E* photoisomerism and high thermal stability of the *Z*-isomers.[24, 25] Keeping in mind that (i) the dynamics of protein binding pockets are crucial for their interaction specificity with ligands of interest,[26] and (ii) the superior photo-physical properties of arylazopyrazoles over conventional azobenzenes, the author designed a new series of photo-switchable arylazopyrazole-based MTX analogs with sterically repulsive alkyl groups on the pyrazole moiety to prevent possible binding to hDHFR (Figure 5-1, upper right). A methylene group between the pyrazole and carbonyl group was introduced as a spacer to compensate for the ring size reduction.

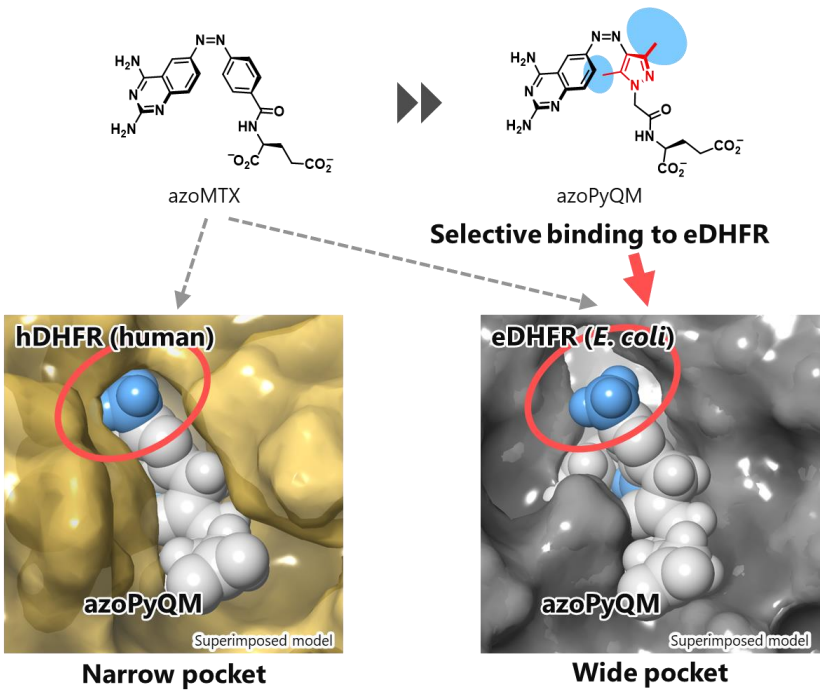

Figure 5-1. Upper panel: Structures of azoMTX and azoPyQs (*Z* isomers). The newly incorporated bulky alkyl groups on a pyrazole moiety have been highlighted. Lower panel: Surface cavity of hDHFR (left) and eDHFR (right) around the region of binding of MTX (PDB ID: 1U72 and 1RX3 for complexation of MTX with hDHFR and eDHFR, respectively).

5-3. Photo-isomerization property of arylazopyrazole-based ligand

Arylazopyrazole-based azoMTX derivatives (hereafter to be referred as azoPyQs) were synthesized in seven consecutive steps (Scheme 5-1), and the structures were verified by ^{1}H NMR, ^{13}C NMR, and ESI-MS analysis. Two kinds of derivatives containing two methyl or ethyl groups on the pyrazole moiety, and the two enantiomers for each by the chirality of the glutamate, totally four compounds were synthesized (Scheme 5-1). The azoPyQs were expected to show the reversible *E*/*Z* photoisomerization (Figure 5-2a). Photoisomerization properties of azoPyQs were monitored through the changes in their UV-vis absorption spectra (Figures 5-2b and 5-3). UV light irradiation at 394 nm induced *E*-to-*Z* isomerization, whereas irradiation at 560 nm induced *Z*-to-*E* isomerization. Furthermore, azoPyQs were repeatedly isomerized by the alternating light irradiations at 394 and 560 nm (Figure 5-4). From the UV-vis absorption spectra at various photostationary states (PSSs), it was also evident that the methyl derivatives have a clear isosbestic point at around 430 nm, whereas the ethyl derivatives do not have such; suggesting that the ethyl derivatives could form aggregates before irradiation (Figure 5-3).

Scheme 5-1. Synthetic route to azoPyQs

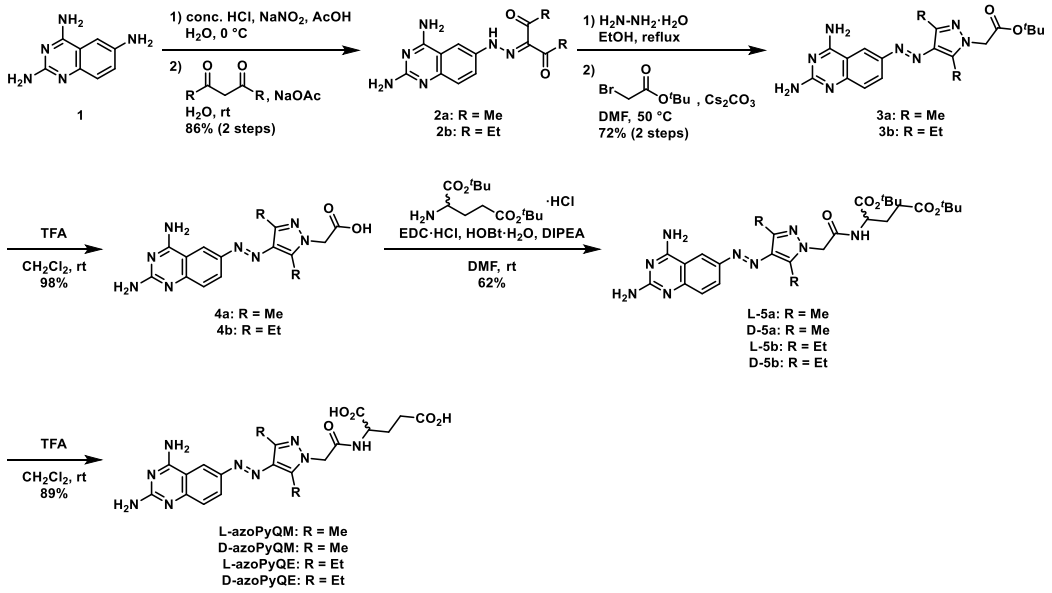

The *E*/*Z* molar ratio values of azoPyQs at different PSSs were determined by HPLC analyses (Table 1, Figures 5-2c, 5-5). Typically, the D- and L-azoPyQM at PSS_{394} contained nearly 90% *Z*-isomers, respectively. Although, in principle, the *Z*-percentage values of the enantiomer pairs such as D-azoPyQM and L-azoPyQM should be the same, the minor differences were observed at each PSSs probably due to the slight thermal or ambient light-induced isomerization during the analytical procedures. Half-lives of *Z*-to-*E* thermal relaxation $T_{1/2}$ were determined (Table S1) by UV-vis spectroscopy at three different high temperatures (50 °C, 60 °C, and 70 °C) by which the $T_{1/2}$ at 25 °C were estimated by an extrapolation of Arrhenius plot (Figure 5-6). D- and L-azoPyQM possesses a thermal half-life of nearly 5 days at 25 °C. Correspondingly, the D- and L-azoPyQE at PSS_{394} contained nearly 90% *Z*-isomer with a thermal half-life of more than several days at 25 °C (Table 1). Photoswitching properties of azoPyQs were superior to azoMTX in several aspects. The percentages

of the active *Z* isomers at PSS_{394} and the thermal half-lives of the *Z* isomers were much improved from those of azoMTX (75% *Z*-isomer at PSS_{394}, $T_{1/2}$ = 5.5 h).[22] In addition, all azoPyQs possessed around 99% *E* isomers at PSS_{560}, which means that they can be converted to the inactive isomers almost quantitatively by 560 nm light irradiation. These excellent properties of azoPyQs show in good agreement with the previous reports that arylazopyrazoles lead to nearly quantitative *Z*-to-*E* photo-conversion and the high thermal stabilities of the *Z* isomers.[24, 25] Thus, light irradiation at various wavelengths enabled the modulation of the molar fraction of *Z*-forms of azoPyQs from 0–2% at the dark state or PSS_{560} to around 90% at PSS_{394}, making these ligands greatly promising to be applied to precise control of biomolecular functions.

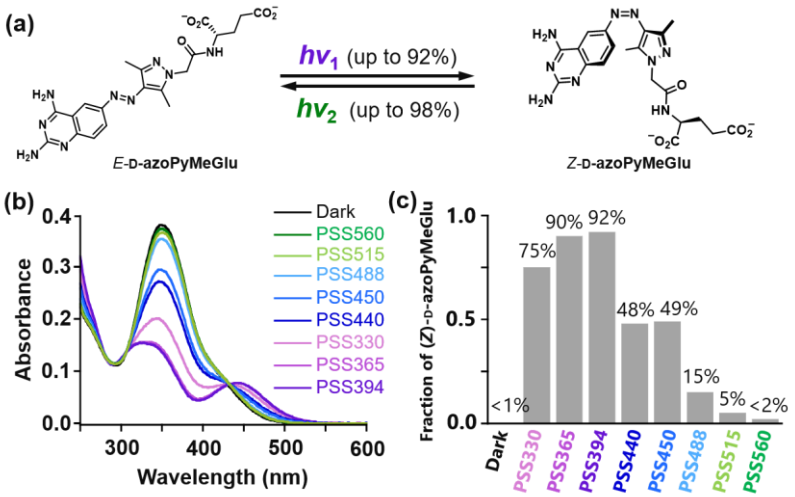

Figure 5-2. (a) Photoisomerization of D-azoPyQM. (b) UV-vis absorption spectra of D-azoPyQM (30 μM) in 100 mM HEPES/NaOH buffer (pH 7.4) containing 100 mM NaCl and 1% DMSO at 25 °C. Light intensity: 5.0 mW cm^{-2} for 10 min. (c) Fraction of (*Z*)-D-azoPyQM by HPLC analysis; light intensity: 5.0 mW cm^{-2} for 10 min, dark: 12 h incubation at 60 °C.

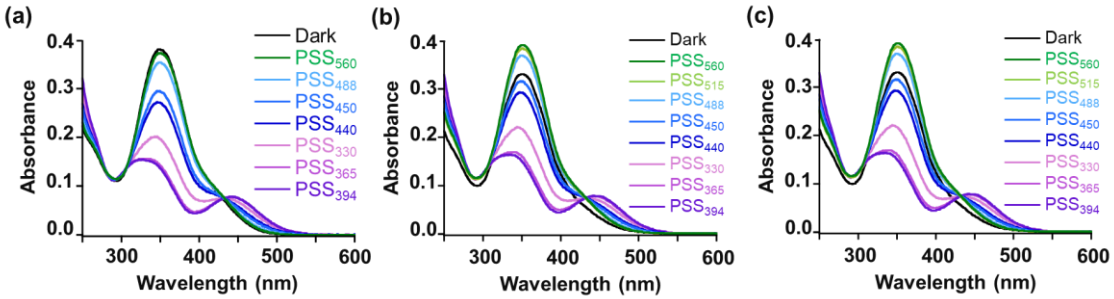

Figure 5-3. UV-vis absorption spectra of L-azoPyQM (a), D-azoPyQE (b), and L-azoPyQE (c) at various photostationary states (PSSs) at 25 °C. Ligand concentrations = 30 μM in 100 mM HEPES–NaOH buffer (pH 7.4), 100 mM NaCl and 1% DMSO.

Table 5-1. *Z* percentages of azoMTX at various photostationary states (PSSs) determined by HPLC (Figure 5-5)

Compound	Percentages of *Z* isomer (%)								$T_{1/2}$
	Dark	PSS_{330}	PSS_{365}	PSS_{394}	PSS_{440}	PSS_{450}	PSS_{488}	PSS_{515}	(*Z* to *E*)
D-azoPyQM	1	75	90	92	48	49	15	5	5 days
L-azoPyQM	2	64	83	85	34	26	9	4	3 days
D-azoPyQE	1	55	85	89	35	17	16	2	7 days
L-azoPyQE	1	67	86	89	24	14	3	1	4 days

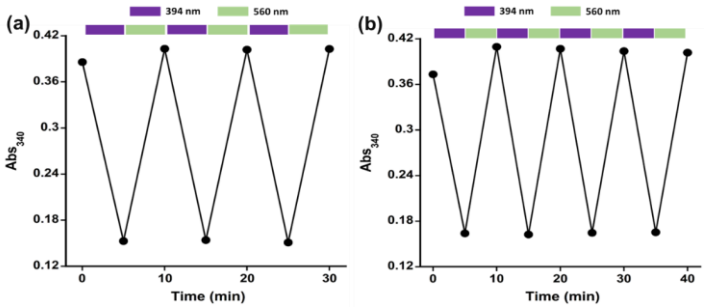

Figure 5-4. Photoisomerization cycle of D-azoPyQM (a) and D-azoPyQE (b) after alternate irradiation with 394 nm and 560 nm light at 25 °C. Ligand concentrations = 30 μM in 100 mM HEPES–NaOH buffer (pH 7.4), 100 mM NaCl and 1% DMSO. Light intensity: 5.0 mW cm^{-2}.

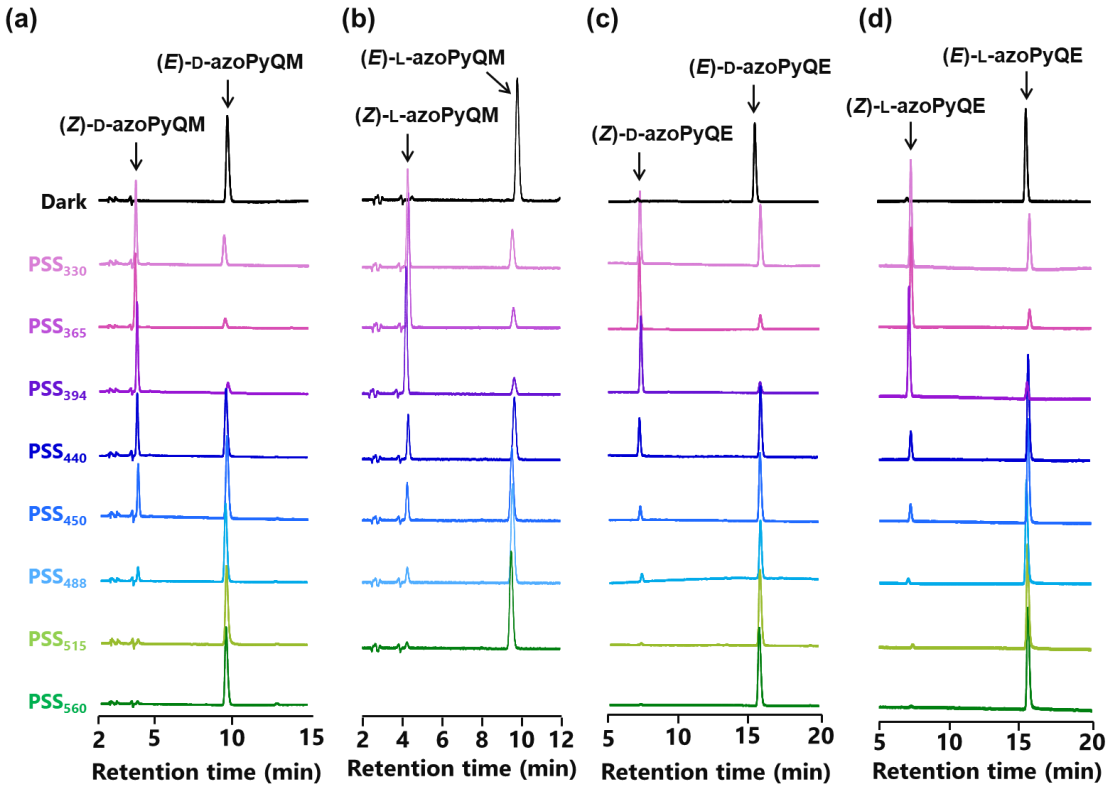

Figure 5-5. HPLC analysis of D-azoPyQM (a), L-azoPyQM (b), D-azoPyQE (c), and L-azoPyQE (d)at the thermal equilibrium (dark) state and various PSSs. AzoPyQs were dissolved at 100 μM in 100 mM HEPES-NaOH buffer (pH 7.4) containing 1% DMSO and irradiated at various light wavelengths just before the injection. Detection wavelength was set to 308 nm. Elution was performed with a 20-min linear gradient 15–25% MeCN/TEAA buffer.

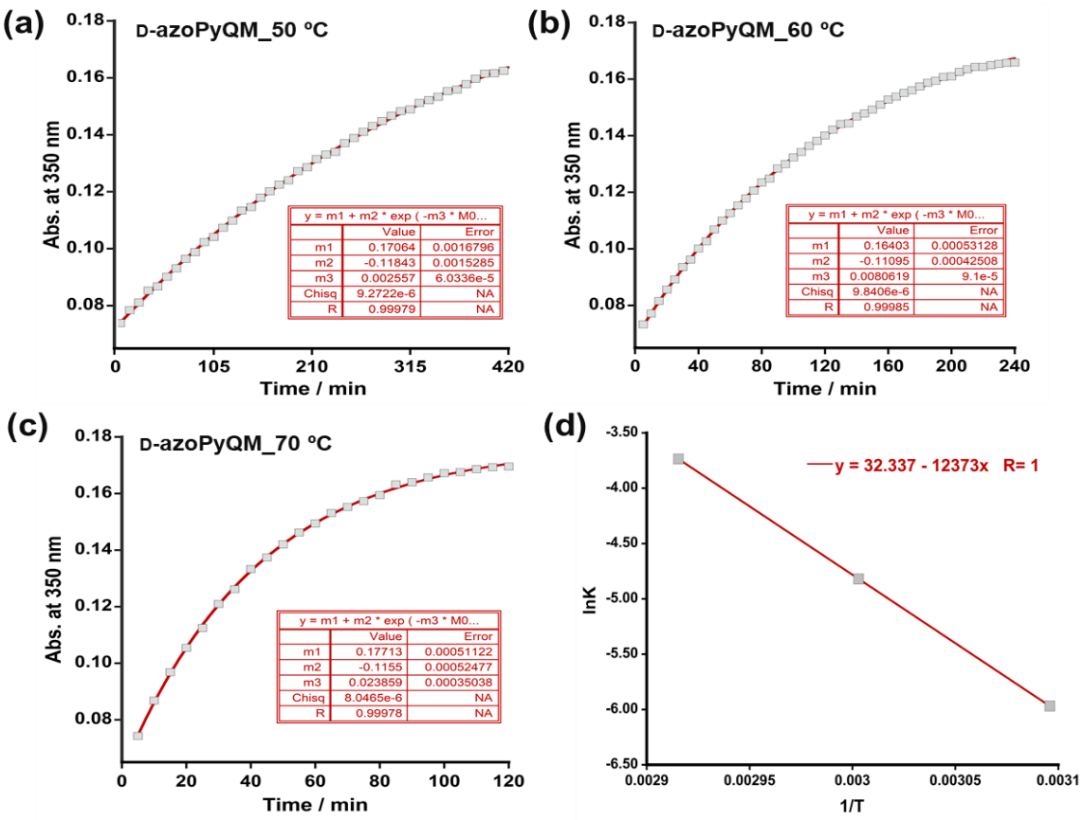

Figure 5-6. (a–c) Time course UV-vis spectral measurement of D-azoPyQM at 50 °C (a), 60 °C (b), and 70 °C (c). (d) ln *k* vs 1/T plot of D-azoPyQM at 50 °C, 60 °C, and 70 °C. [D-azoPyQM] = 10 μM in 100 mM HEPES–NaOH buffer (pH 7.4) containing 100 mM NaCl and 5% DMSO. Light intensity: 5.0 mW cm^{-2}.

5-4. Selective binding to eDHFR over hDHFR

Next, the author investigated the binding of azoPyQs to eDHFR by monitoring the enzyme reaction of eDHFR, which catalyzes the hydride transfer reaction from NADPH to the physiological substrate dihydrofolate (DHF). Thus, the decrease of the absorbance at 340 nm of NADPH represents the enzyme reaction progress.[27] AzoPyQs were converted to the thermo-equilibrium *E*-forms under dark conditions or to around 90% *Z*-forms under irradiation of 394 nm light, and mixed with NADPH and DHF. The enzyme reaction was initiated by adding eDHFR using a stopped-flow instrument. By comparing with the initial reaction rate in the absence of an inhibitor, the author estimated the inhibited fractions of the eDHFR (Figures 5-7c, 5-8). The *Z*-forms of azoPyQs inhibited over 60% of eDHFR activity, whereas the *E*-isomers showed almost no inhibition (< 2%). As expected from the molecular design, the same enzyme reaction experiments with hDHFR showed almost no inhibitions by both *E*- and *Z*-isomers of the azoPyQs (Figure 5-7d). These results indicate that the two alkyl substituents of azoPyQs expectedly increased the selectivity towards eDHFR over hDHFR.

Since real-time reversible control of protein functions is one of the promising applications of photopharmacology, photo-reversible binding and dissociation of azoPyQs to eDHFR was investigated (Figure 5-7a). In the presence of MTX or the absence of inhibitor, the reaction curve slope was not affected by the light irradiation. In the presence of 500 nM azoPyQs preincubated under dark

condition, the reaction curve slopes were initially very similar to that without inhibitor. However, the following394-nm light irradiation made the reaction slopes much gentle, indicating that the *Z*-form azoPyQs were bound to the large fraction of eDHFR within a few seconds. Then, 515-nm light irradiation quickly recovered the enzyme reaction progress, indicating the dissociation of azoPyQs from eDHFR. These inhibition and reactivation cycles upon the alternating light irradiations at 394 and 515 nm were repeated several times for all azoPyQs (Figures 5-7c, 5-9).

From the abovementioned photo-reversible enzyme activity inhibition assay, the author found that (*Z*)-D-azoPyQM showed the highest inhibitory effect towards eDHFR as well as the lowest affinity towards hDHFR among all the four azoPyQs. In view of that, the author further investigated the

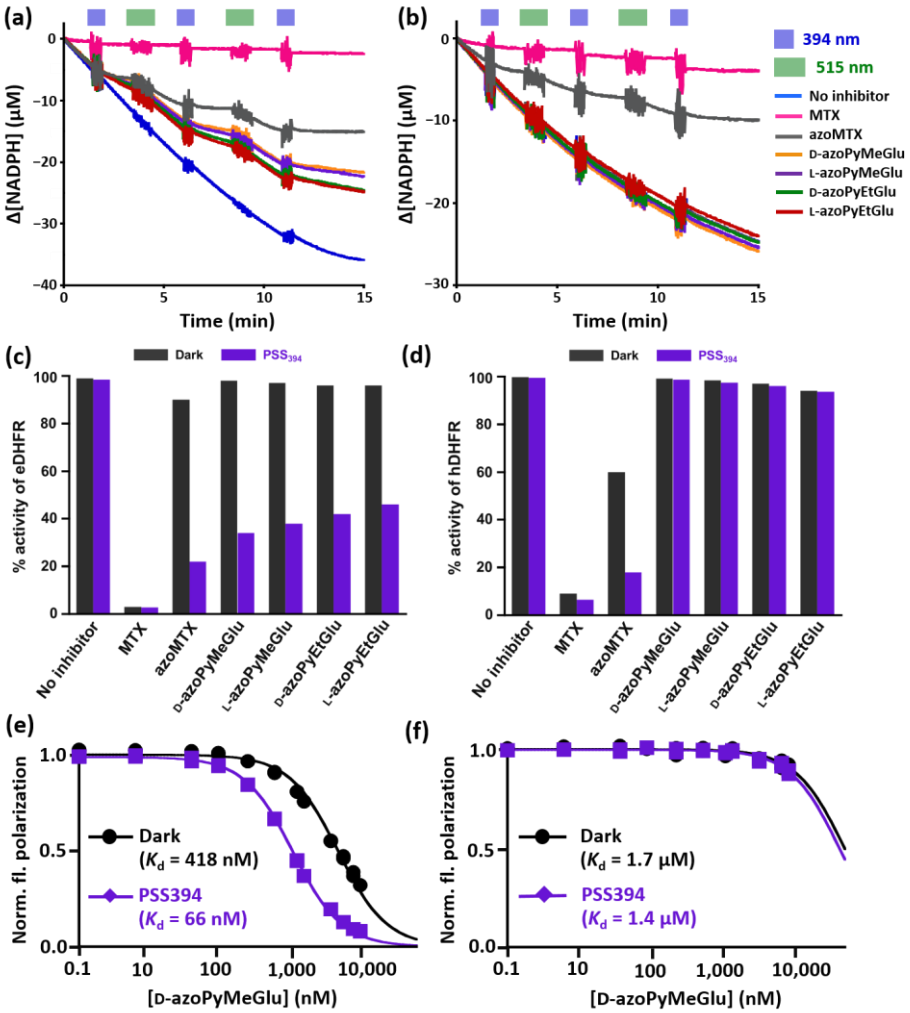

Figure 5-7. (a, b) Real-time photo-reversible inhibition of eDHFR (a) or hDHFR (b) activity with azoPyQs. [eDHFR] = [hDHFR] = 5 nM, [NADPH] = 60 μM, [dihydrofolate] = 50 μM, [azoMTX] = 100 nM (for eDHFR) and 300 nM (for hDHFR), [MTX] = 300 nM, [azoPyQs] = 500 nM in 100 mM HEPES buffer (pH 7.4), 100 mM NaCl at 25 °C. Light intensity: 11 mW cm^{-2} for 394 nm and 12.5 mW cm^{-2} for 515 nm. (c, d) Relative enzymatic activities of eDHFR (a) and hDHFR (b) in the presence of azoPyQs at dark state or PSS_{394}. (e, f) Competitive fluorescence polarization assay of eDHFR (e) or hDHFR (f) with D-azoPyQM. [TMP-Fl] = [MTX-Fl] = 3 nM, [eDHFR] = [hDHFR] = 6 nM, [NADPH] = 5 μM in 100 mM HEPES–NaOH buffer (pH 7.4) containing 100 mM NaCl at 37 °C. Fluorescence polarization measurement: λ_{ex} = 495 nm, λ_{em} = 520 nm; Dark: 12 h incubation at 60 °C, PSS394: irradiated with 394/10 nm light at 5.0 mW cm^{-2} for 10 min before the assay measurement.

dissociation constants (K_ds) of D-azoPyQM to both eDHFR and hDHFR by competitive fluorescence depolarization assay with fluorescein-modified TMP and MTX (TMP-Fl and MTX-Fl, respectively) (Figure 5-7e,f). The IC_{50} values of D-azoPyQM towards eDHFR and hDHFR were determined to be 4.0 μM/640 nM (dark/PSS_{394}) and 99 μM/80 μM (dark/PSS_{394}), respectively. Applying these IC_{50} values to Nikolovska-Coleska[28] equation with the predetermined K_d values for TMP-Fl to eDHFR and MTX-Fl to hDHFR (0.60 nM and 0.075 nM, respectively), the K_d values of D-azoPyQM to eDHFR and hDHFR were estimated to be 66 nM/420 nM (PSS_{394}/dark) and 1.4 μM/1.7 μM (PSS_{394}/dark), respectively. The binding assay results simply indicate that D-azoPyQM has about 6 times higher binding affinity towards eDHFR at the PSS_{394} than at the dark state. This difference in the binding affinity enables the optical regulation of eDHFR enzyme reactions depending on the irradiation wavelengths.

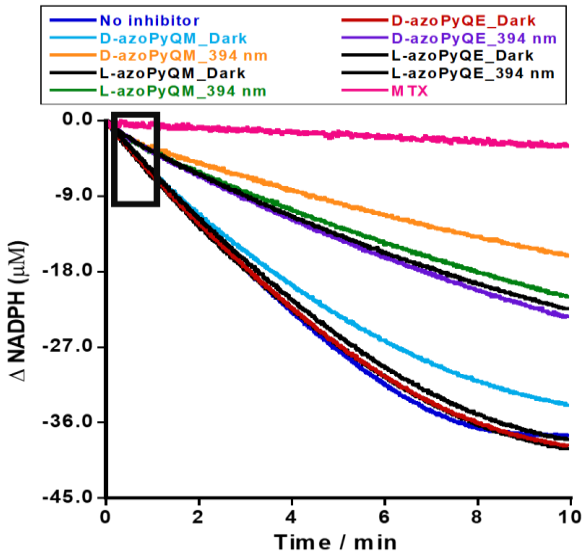

Figure 5-8. Rapid kinetics of enzyme inhibition by stopped flow method. [eDHFR] = 10 nM, [inhibitors] = 500 nM, [dihydrofolate] = 50 μM, [NADPH] = 60 μM in 100 mM (pH 7.4) and 100 mM NaCl at 25 °C. *The indicated rectangular area has been used for calculation of % inhibition.

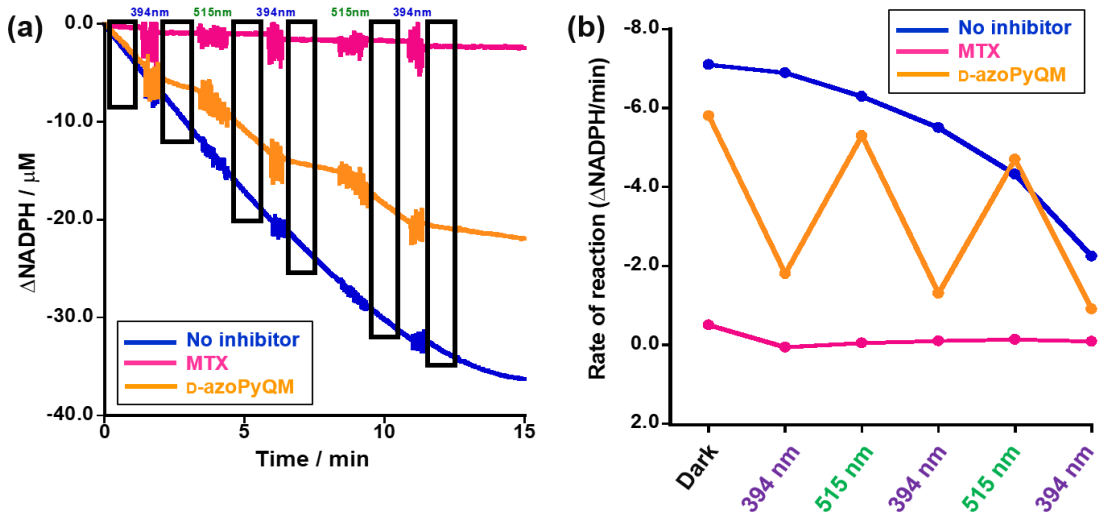

Figure 5-9. Reversible enzyme activity inhibition assay by UV-vis spectral measurement of D-azoPyQM at 25 °C. [eDHFR] = 5 nM, [NADPH] = 60 μM, [dihydrofolate] = 50 μM, [MTX] = 300 nM, [D-azoPyQM] = 500 nM in 100 mM HEPES buffer (pH 7.4), 100 mM NaCl. Light intensity: 11 mW cm^{-2} for 394 nm and 12.5 mW cm^{-2} for 515 nm.

5-5. Conclusion

In conclusion, the author has developed a new set of arylazopyrazole-based MTX analogs that bind selectively and photo-reversibly with eDHFR depending on the specific irradiation wavelength. In the molecular design, a pyrazole unit substituted with two alkyl groups was incorporated into the core structure of previously developed azoMTX. The arylazopyrazole skeleton enabled the nearly quantitative *Z*-to-*E* photoisomerization along with the high thermal stability of the active *Z* isomers. Incorporation of the two alkyl groups on the pyrazole moiety improved the selectivity towards eDHFR over hDHFR. Reversible photoisomerization properties also led to the real-time reversible control of eDHFR activity, which means reversible ligand binding and dissociation with eDHFR. One of the ligands, D-azoPyQM showed 6 times higher binding affinity towards eDHFR at PSS_{394} than under dark conditions.

Due to the low affinity with hDHFR, the azoPyQs have a great potential to be used as a photo-reversible system for the desired protein labeling without interference of functions of the mammalian DHFR enzymes. However, the author also needs to pursuit a larger K_d difference between the two isomers by modifying the structures of the ligand and the tag proteins. These multifaceted approaches will lead to practical photo-switchable labeling systems, which should bring a great breakthrough of optical biomolecular manipulation technology to compensate optogenetics and caged compounds. As another important application, the photopharmacological direction is also promising. Recently, researchers achieved control of antibacterial activity in the presence of bacteria using photopharmacological agents with a molecular photo-switch.[18, 22, 29] Since the bioactivity of the drug could be controlled by light and only be activated when needed, this achievement is a step towards the *in vivo* control of photo-switchable antibiotics.

5-6. Experimental section (chapter 5)

Materials and instruments

Unless otherwise specified, all reagents were purchased from the chemical suppliers Fujifilm Wako Pure Chemical Corporation (Osaka, Japan), Tokyo Chemical Industry Co. (Tokyo, Japan), Kanto Chemical Co. (Tokyo, Japan), Nacalai Tesque (Kyoto, Japan), Watanabe Chemical Industries (Hiroshima, Japan), and Sigma-Aldrich Japan K. K. (Tokyo, Japan). They were used without further purification.

Restriction enzymes were purchased from New England Biolabs Japan Inc. (Tokyo, Japan). Stock solutions of azoMTX derivatives (10 mM) were dissolved in DMSO (spectrochemical analysis grade, Wako) before spectroscopic measurements, to facilitate its solubilization in an aqueous solution. NMR spectra were recorded on a Bruker AVANCE III 400 instrument at 400 MHz for ^{1}H NMR and 101 MHz for ^{13}C NMR or a Bruker AVANCE III 500 instrument at 500 MHz for ^{1}H NMR and 126 MHz for ^{13}C NMR. Chemical shifts (δ) are quoted in ppm downfield from tetramethylsilane, referenced to residual solvent signals (^{1}H NMR: δ = 7.26 for $CDCl_3$, 2.50 for DMSO-d_6, and 3.31 for CD_3OD; ^{13}C NMR: δ = 39.5 for DMSO-d_6 and 49.1 for CD_3OD). The high-resolution mass spectrometry analyses were performed on a Bruker micrOTOF-Q II mass spectrometer. HPLC analyses and purification were performed with an Inertsil ODS-3 column (4.6 mm × 250 mm for analysis or 14.0 mm × 250 mm for purification, GL-Science Inc.), using an HPLC system that comprised a pump (PU- 2080, JASCO) and a detector (MD-2018, JASCO), and the absorbance was monitored at 215, 254, 280, and 308 nm unless otherwise specified. Solvent A was composed of 0.1% formic acid in water and/or 10mM TEAA. Solvent B was composed of 0.1% formic acid in acetonitrile and/or acetonitrile. For photoisomerization analysis, elution was performed with a 20-min linear gradient from 15% MeCN/triethylammonium acetate (TEAA) buffer (pH 6.7) to 25% MeCN/TEAA buffer. UV-vis absorption spectra and time-dependent absorption change were measured using a SHIMADZU UV-2450 spectrophotometer, with the slit width set to 1 nm. For photoisomerization analysis of azoMTX derivatives, light irradiation was performed by using a Xe light source (MAX-303; Asahi Spectra) equipped with band-pass filters (330, 365, 394, 440, 450, 488, 515, and 560 nm). Binding assay experiments have been carried out using Greiner 96-well microplates. Fluorescence polarization values were measured using JASCO FP-8500 spectrometer and PerkinElmer Nivo SF microplate reader. The slit widths were set to 10 nm for both excitation and emission. Excitation and emission wavelengths were set to 495 nm and 520 nm, respectively. Kinetics of enzyme reactions were measured by a stopped-flow method using RX.2000 rapid kinetics system of Applied Photophysics. The following abbreviations were used to describe spin multiplicities in ^{1}H NMR spectra: s = singlet, d = doublet, t = triplet, q: quartet, m = multiplet.

Synthesis of azoPyQs

Synthesis of 3-(2-(2,4-diaminoquinazolin-6-yl)hydrazineylidene)pentane-2,4-dione (**2a**)

The solution of sodium nitrite (400 mg, 2.28 mmol) in water (2.0 mL) was dropped into the solution of **1** (400 mg, 2.28 mmol) in acetic acid (4.8 mL), concentrated hydrochloric acid (0.54 mL), and water (6.0 mL) at 0 °C. After stirring at 0 °C for 1.5 h, the solution was transferred to the mixture of pentane-2,4-dione (283 µL, 275 mg, 2.74 mmol) and sodium acetate (673 mg, 8.20 mmol) in water (1.5 mL). After stirring at ambient temperature for 2 h, the mixture was filtered to collect precipitation. The precipitation was washed with water, 50% ethanol/water, and hexane to give **2a** (519 mg, 1.81 mmol, 79%) as an orange solid.

^{1}H NMR (600 MHz, DMSO-d_6) δ 14.48 (br s, 1H), 8.20 (br s, 2H), 8.16 (d, J = 2.3 Hz, 1H), 7.93 (dd, J = 9.0, 2.3 Hz, 1H), 7.41 (d, J = 9.0 Hz, 1H), 6.99 (br s, 2H), 2.49 (s, 3H), 2.46 (s 3H); ^{13}C NMR (151 MHz, DMSO-d_6) δ196.8, 196.3, 162.4, 157.4, 143.7, 136.2, 133.3, 122.9, 122.1, 111.1, 111.0, 31.2, 26.7; HRMS (ESI$^+$) m/z Calcd. for $C_{13}H_{15}N_6O_2^+$ $[M+H]^+$ 287.1251, found 287.1256.

Synthesis of 4-(2-(2,4-diaminoquinazolin-6-yl)hydrazineylidene)heptane-3,5-dione (**2b**)

The synthetic procedure is the same as above mentioned procedure for compound **2a**. Heptane-3,5-dione was used instead of pentan-2,4-dione. **2b** was obtained (622 mg, 1.98 mmol, 87%) as a yellow solid.

^{1}H NMR (600 MHz, DMSO-d_6): δ 14.35 (br s, 1H), 8.36 (br s, 2H), 8.17 (d, J = 2.3 Hz, 1H), 7.94 (dd, J = 9.0, 2.3 Hz, 1H), 7.44 (d, J= 6.0 Hz, 1H), 7.18 (br s, 2H), 2.98 (q, J = 7.3 Hz, 2H), 2.93 (q, J = 7.2 Hz, 2H), 1.05 (t, J = 7.3 Hz, 3H), 1.03 (t, J = 7.2 Hz, 3H); ^{13}C NMR (151 MHz, DMSO-d_6) δ 200.1, 199.0, 162.5, 156.7, 141.9, 136.9, 133.0, 123.1, 121.2, 110.9, 110.0, 35.5, 30.7, 8.4, 7.8; HRMS (ESI$^+$) m/z: Calcd. for $C_{15}H_{18}N_6O_2^+$ $[M+H]^+$ 315.1564, found 315.1566.

Synthesis of tert-butyl-(*E*)-2-(4-((2,4-diaminoquinazolin-6-yl)diazenyl)-3,5-dimethyl-1*H*-pyrazol-1-yl)acetate (**3a**)

The suspension of **2a** (120 mg, 419 µmol) and hydrazine monohydrate (20.4 µL, 21.0 mg, 420 µmol) in ethanol (15 mL) was stirred at reflux temperature under a nitrogen atmosphere for 16 h. After cooling, the volatile materials were removed in vacuo to give crude pyrazole (124 mg) as a yellow sold. The suspension of crude pyrazole (124 mg), *tert*-butyl bromoacetate (79.8 µL, 106 mg, 544 µmol), and cesium carbonate (205 mg, 629 µmol), in dry DMF (9.0 mL) was stirred at 50 °C for 15 h. After the reaction mixture cooled, the volatile materials were removed in vacuo. The crude material was purified by silica gel column chromatography (eluent: 8–12% methanol/dichloromethane) to give **3a** (127 mg, 320 µmol, 76%) as an orange solid.

^{1}H NMR (600 MHz, CD_3OD) δ 8.40 (d, J = 2.1 Hz, 1H), 8.08 (dd, J = 9.0, 2.1 Hz, 1H), 7.35 (d, J = 9.0 Hz, 1H), 4.86 (s, 2H), 2.57 (s, 3H), 2.47 (s, 3H), 1.50 (s, 9H); ^{13}C NMR (151 MHz, CD_3OD) δ 168.3, 165.3, 161.0, 150.9, 149.8, 143.7, 142.3, 136.1, 125.7, 123.8, 122.2, 111.3, 84.1, 52.0, 28.2, 14.2, 9.7; HRMS (ESI$^+$) m/z calcd. for $C_{19}H_{25}N_8O_2^+$ $[M+H]^+$ 397.2095, found 397.2107.

Synthesis of tert-butyl-(*E*)-2-(4-((2,4-diaminoquinazolin-6-yl)diazenyl)-3,5-diethyl-1*H*-pyrazol-1-yl)acetate (**3b**)

The synthetic procedure is the same as above mentioned procedure for compound **3a**. **3b** was obtained (154 mg, 363 μmol, 57%) as a yellow solid.

^{1}H NMR (600 MHz, DMSO-d_6) δ 8.46 (d, J = 2.1 Hz, 1H), 7.93 (dd, J = 9.0, 2.1 Hz, 1H), 7.67 (br s, 2H), 7.28 (d, J = 9.0 Hz, 1H), 6.40 (br s, 2H), 4.95 (s, 2H), 2.96 (q, J = 7.5 Hz, 2H), 2.86 (q, J = 7.5 Hz, 2H), 1.44 (s, 9H), 1.20 (t, J = 7.5 Hz, 6H); ^{13}C NMR (151 MHz, DMSO-d_6) δ 167.1, 163.0, 160.7, 152.6, 146.7, 146.4, 144.5, 133.4, 124.5, 122.34, 122.27, 109.9, 81.9, 51.0, 27.6, 21.0, 17.2, 13.4, 12.8; HRMS (ESI+) *m*/*z* calcd. for $C_{21}H_{29}N_8O_2^+$ $[M+H]^+$ 425.2408, found 425.2413.

Synthesis of (*E*)-2-{4-[(2,4-Diaminoquinazolin-6-yl)diazenyl]-3,5-dimethyl-1*H*-pyrazol-1-yl}acetic acid (**4a**)

The solution of **3a** (126 mg, 318 μmol) in dry dichloromethane (3.0 mL) and TFA (0.75 mL) was stirred at ambient temperature under a nitrogen atmosphere for 22 h. After removing the volatile materials in vacuo, the residue was washed with dichloromethane and acetonitrile to give trifluoroacetate salt of **4a** (126 mg, 277 μmol, 87%) as a yellow solid.

^{1}H NMR (600 MHz, DMSO-d_6) δ 13.06 (br s, 1H), 9.18 (br s, 1H), 8.90 (br s, 1H), 8.64 (d, J = 2.0 Hz, 1H), 8.17 (dd, J = 8.9, 2.0 Hz, 1H), 8.06 (br s, 2H), 7.54 (d, J = 8.9 Hz, 1H), 4.96 (s, 2H), 2.56 (s, 3H), 2.42 (s, 3H); ^{13}C NMR (151 MHz, DMSO-d_6) δ 169.1, 163.3, 154.7, 149.2, 141.5, 140.8, 140.1, 134.6, 126.3, 120.3, 117.9, 109.8, 50.6, 13.9, 9.4; HRMS (ESI^+) *m*/*z* Calcd. for $C_{15}H_{17}N_8O_2^+$ $[M+H]^+$ 341.1469, found 341.1468.

Synthesis of (*E*)-2-{4-[(2,4-Diaminoquinazolin-6-yl)diazenyl]-3,5-diethyl-1*H*-pyrazol-1-yl}acetic acid (**4b**)

The synthetic procedure is the same as above mentioned procedure for compound **4a**. The trifluoroacetate salt of **4b** was obtained (175 mg, 363 μmol, 85%) as a yellow solid.

^{1}H NMR (600 MHz, DMSO-d_6) δ 12.96 (br s, 1H), 9.21 (br s, 1H), 8.90 (br s, 1H), 8.64 (d, J = 2.0 Hz, 1H), 8.13 (dd, J = 8.9, 2.0 Hz, 1H), 8.02 (br s, 2H), 7.55 (d, J = 8.9 Hz, 1H), 4.98 (s, 2H), 3.00 (q, J = 7.5 Hz, 2H), 2.87 (q, J = 7.5 Hz, 2H), 1.22 (t, J = 7.5 Hz, 3H), 1.21 (t, J = 7.5 Hz, 3H); ^{13}C NMR (151 MHz, DMSO-d_6) δ 169.4, 163.2, 154.7, 149.3, 146.6, 145.8, 140.2, 133.7, 125.5, 121.0, 118.1, 109.8, 50.6, 21.1, 17.3, 13.4, 12.6; HRMS (ESI+) *m*/*z* calcd. for $C_{17}H_{21}N_8O_2^+$ $[M+H]^+$ 369.1782, found 369.1787.

Di-*tert*-butyl (*E*)-(2-{4-[(2,4-diaminoquinazolin-6-yl)diazenyl]-3,5-dimethyl-1*H*-pyrazol-1-yl}acetyl)-L-glutamate (L-**5a**)

The suspension of **4a** (15.0 mg, 44.1 μmol), di-*tert*-butyl L-glutamate monohydrochloride (15.5 mg, 52.4 μmol), EDC·HCl (10.0 mg, 52.2 μmol), HOBt·H_2O (7.51 mg, 49.0 μmol), and DIPEA (23 μL, 17 mg, 1.3×10^2 μmol) in dry DMF (2.0 mL) was stirred at ambient temperature under a nitrogen atmosphere for 14 h. After adding a saturated aqueous sodium bicarbonate solution (3 mL) at 0 °C, the organic materials were extracted with dichloromethane (4 × 5 mL). The organic layer was washed with brine (50 mL), dried over magnesium sulfate, and concentrated in vacuo. The crude material was purified by silica gel column chromatography (10% methanol/dichloromethane) to give *l*-**5a** (10.8 mg, 18.6 μmol, 42%) as an orange solid.

^{1}H NMR (400 MHz, CD_3OD) δ 8.43 (s, 1H), 8.10 (d, *J* = 8.9 Hz, 1H), 7.37 (d, *J* = 8.9 Hz, 1H), 4.89 (s, 2H), 4.38 (dd, *J* = 8.9 Hz, 5.1 Hz, 1H), 2.62 (s, 3H), 2.49 (s, 3H), 2.36 (t, *J* = 7.5 Hz, 2H), 2.18–1.06 (m, 1H), 1.98–1.85 (m, 1H), 1.48 (s, 9H), 1.44 (s, 9H).

(*E*)-(2-{4-[(2,4-diaminoquinazolin-6-yl)diazenyl]-3,5-dimethyl-1*H*-pyrazol-1-yl}acetyl)-L-glutamic acid (L-azoPyQM)

The solution of L-**5a** (10.8 mg, 18.6 μmol) in dry dichloromethane (2.0 mL) and TFA (0.50 mL) was stirred at ambient temperature under a nitrogen atmosphere for 13 h. After removing the volatile materials in vacuo, the residue was washed with dichloromethane and acetonitrile to give *l*-azoPyQM (7.1 mg, 15.1 μmol, 81%) as a yellow solid.

^{1}H NMR (DMSO-d_6, 400 MHz) δ 12.50 (br s, 1H), 12.23 (br s, 1H), 9.19 (br s, 1H), 8.92 (br s, 1H), 8.64 (d, *J* = 2.0 Hz, 1H), 8.63 (d, *J* = 8.3 Hz, 1H), 8.18 (dd, *J* = 8.9 Hz, 2.0 Hz, 1H), 7.97 (br s, 2H), 7.56 (d, *J* = 8.9 Hz, 1H), 4.90 (d, *J* = 16.7 Hz, 1H), 4.84 (d, *J* = 16.7 Hz, 1H), 4.30–4.22 (m, 1H), 2.56 (s, 3H), 2.41 (s, 3H), 2.32 (t, *J* = 7.9 Hz, 2H), 2.06–1.96 (m, 1H), 1.88–1.76 (m, 1H); MS (ESI^-) *m*/*z* Calcd. for $C_{20}H_{22}N_9O_5^-$ $[M-H]^-$ 468.17, found 468.17.

Construction of expression vectors

human dihydrofolate reductase (hDHFR)

A gene coding hDHFR was purchased from Eurofins Genomics. An *Nde*I/*Bam*HI fragment containing the hDHFR gene was inserted into a corresponding region of a modified pET-28a(+) plasmid, in which a sequence inserted for His-tag cleavage by a thrombin protease was replaced with a sequence encoding a TEV protease recognition sequence (ENLYFQG) and the following linker (GGGS). The resulting expression vector was termed pET28tev-hDHFR.

Preparation of proteins

hDHFR

E. coli strain BL21(DE3) (Nippon Gene) was transformed with pET28tev-hDHFR and grown at 37 °C in LB medium (Becton, Dickinson) containing 20 μg mL^{-1} kanamycin. When OD600 reached 0.6, IPTG (final concentration: 0.4 mM) was added to induce hDHFR at 25 °C. After a 16 h induction, the cells were harvested by centrifugation at 3,800 × g for 20 min. The cell pellet was re-suspended in 30 mL of Buffer A (100 mM potassium phosphate (pH 7.4), 1 mM phenylmethylsulfonyl fluoride, and 1 mM dithiothreitol (DTT)) and lysed by sonication. After the lysate was centrifuged at 15,000 × g for 30 min, the supernatant was loaded on a HisTrap HP column (GE Healthcare), equilibrated with Buffer B (100 mM potassium phosphate (pH 8.0) and 10% glycerol) containing 10 mM imidazole. The His-tagged hDHFR was eluted using an imidazole gradient from 10 to 270 mM in Buffer B. The appropriate fractions were collected and repeatedly ultra-filtered (Amicon Ultra-15, cut off 10 kDa, Millipore) for buffer exchange to Buffer C (100 mM potassium phosphate (pH 8.0), 100 mM NaCl, 1 mM DTT, 0.5 mM ethylenediaminetetraacetate, and 10% glycerol). The purified protein (151 μM) was incubated with His-tagged TEV protease[1] (4.5 μM) at 4 °C for 15 h for tag removal. The digestion solution was passed through a HisTrap HP column to remove any protein/peptide containing the His-tag. Untagged eDHFR was repeatedly ultra-filtered for buffer exchange to Buffer D (100 mM potassium phosphate (pH 8.0), 100 mM NaCl, and 10% glycerol). The concentrated protein was stored at −80 °C until use. The concentration of hDHFR was calculated from the absorbance at 280 nm (ε_{280} = 46.2 mM^{-1} cm^{-1}).

Photo- and thermal isomerization of azoPyQs

AzoMTX derivatives were dissolved in 100 mM HEPES-NaOH buffer (pH 7.4) containing 100 mM NaCl and 1% DMSO at the concentration of 30 μM for absorption measurements or in 100 mM HEPES-NaOH buffer (pH 7.4) containing 1% DMSO at 100 μM for the HPLC experiments. The samples were irradiated with various light wavelengths (5.0 mW cm^{-2}) at 25 °C before the experiment, excepting the time-dependent absorption measurement. The absorption spectrum of *Z* isomers was estimated by subtracting the absorbance of the remaining fraction of *E* isomers, which was determined by HPLC analyses (Figure 5-5 and Table 1), from those of the various PSSs. For the time-dependent absorption measurement, the sample solutions were irradiated from the top of the UV-vis spectrometer sample chamber, and the acquisition of absorbance at 340 nm was continued under light irradiation (5.0 mW cm^{-2}). For the thermal relaxation experiment, the sample absorbance at 350 nm was recorded at three different temperatures: 50 °C, 60 °C, and 70 °C in dark condition after illuminating with 394 nm light (10 min, 5.0 mW cm^{-2}).

Real-time photoreversible control of DHFRs activity with azoPyQs

Determination of enzymatic inhibition efficiency

The optical regulation of the DHFRs activity with azoMTX derivatives was evaluated by the initial rate of enzymatic reaction. The reaction rate under excessive amounts of dihydrofolate and NADPH was determined by monitoring the decrease in NADPH absorbance at 340 nm (ε_{340} = 13.2 mM^{-1} cm^{-1}) eDHFR (5 nM) was pre-incubated with 60 μM NADPH (and/or 500 nM inhibitors) at 25 °C in 100 mM HEPES-NaOH buffer (pH 7.4) containing 100 mM NaCl. The measurement was started 30 s after the reaction was initiated upon the addition of 50 μM dihydrofolate at 25 °C. AzoMTX derivatives at PSS_{394} states were obtained under irradiation with 394 nm light at 11 mW cm^{-2} for 10 min, PSS_{515} states were obtained under irradiation with 515 nm light at 12.5 mW cm^{-2} for 10 min, and the dark states were obtained under 12 h incubation at 60 °C. The initial rates of the enzyme reaction (v_0) were determined using the following equation,

$$v_0 = |A_{340,30s} - A_{340,0s}| / [(30/60) \times (13.2 \times 10^{-3})] \ (\mu M\ min^{-1})$$

, where $A_{340,30s}$ is the absorbance at 340 nm after 30 s from the measurement start, and $A_{340,0s}$ is the absorbance at 340 nm just after the start (i.e., initiation of enzyme reaction).

Rapid kinetics of enzyme inhibition was also carried out by the stopped flow rapid mixing method. The percentage changes in NADPH consumption in the enzymatic reaction have been evaluated to obtain the % inhibition of eDHFR/hDHFR activity by the inhibitors.

From the slope (rate of the enzymatic reaction) of each curve, the author has carried out the calculations using the below-mentioned formula,

$$\%\ \text{inhibition of eDHFR activity: } (v_{Non} - v_{Inhibitor}) / v_{Non} \times 100$$

, where $v_{0,Non}$ is the reaction rate without inhibitor and $v_{0,Inhibitor}$ is the reaction rate with inhibitor.

Real-time photo-reversible regulation of enzyme reaction

AzoMTX derivatives (500 nM) were mixed with 60 μM NADPH and 50 μM dihydrofolate in 100 mM HEPES-NaOH buffer (pH 7.4) containing 100 mM NaCl, and the reaction mixture was pre-incubated at 25 °C. The measurement was started 30 s after the enzyme reaction was initiated upon the addition of 5 nM eDHFR/hDHFR, and the reaction sample was repeatedly irradiated with 394/10 nm or 515/10 nm wavelength of light. Light intensity was set to 11 mW cm^{-2} for 394 nm and 12.5 mW cm^{-2} for 515 nm, respectively.

Binding assay

Competitive binding assays for azoMTX derivatives at dark state and PSS_{394} toward eDHFR/hDHFR were carried out using eDHFR (6 nM) bound with TMP-Fl (3 nM) and/or hDHFR (6 nM) bound with MTX-Fl (3 nM) in 100 mM HEPES-NaOH buffer (pH 7.4) containing 100 mM NaCl at 25 °C. AzoMTX derivatives at PSS_{394} were irradiated with 394/10 nm light at 5.0 mW cm^{-2} for 10 min just before the assay, whereas the dark states were obtained under 12 h incubation at 60 °C. Fluorescence polarization measurements were carried out using λ_{ex} = 495 nm and λ_{em} = 520 nm. The IC_{50} values were determined from the plot using nonlinear least-squares analysis.

^{1}H and ^{13}C NMR spectra

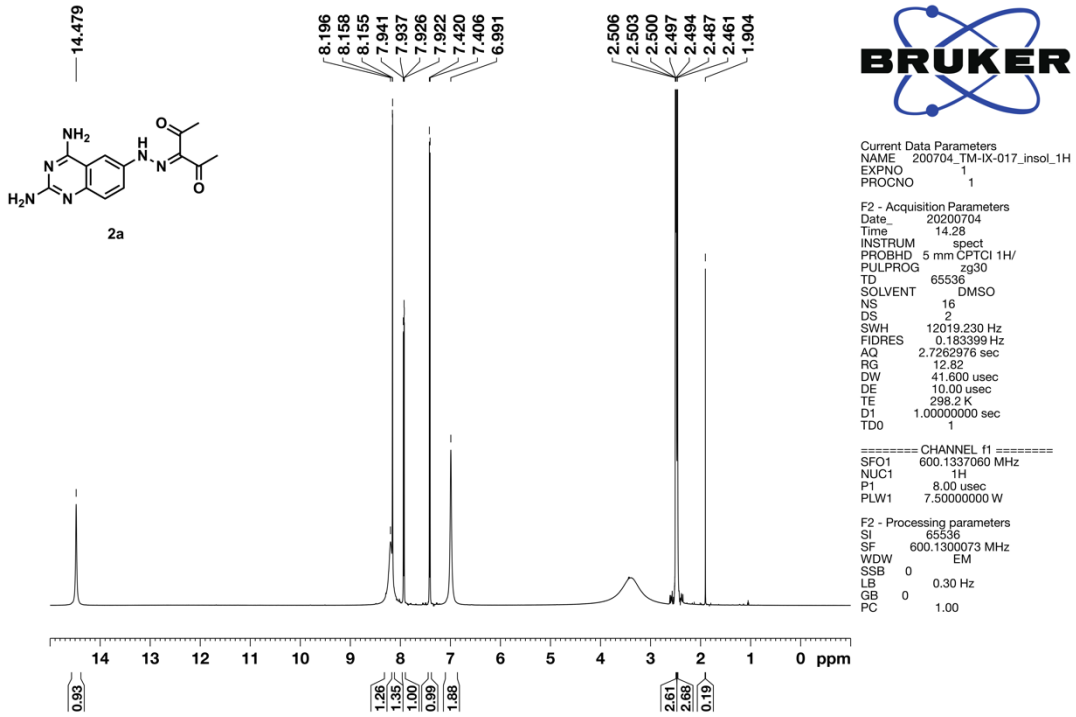

Figure S5-1. ^{1}H NMR spectrum of compound **2a** (600 MHz, DMSO-d_6).

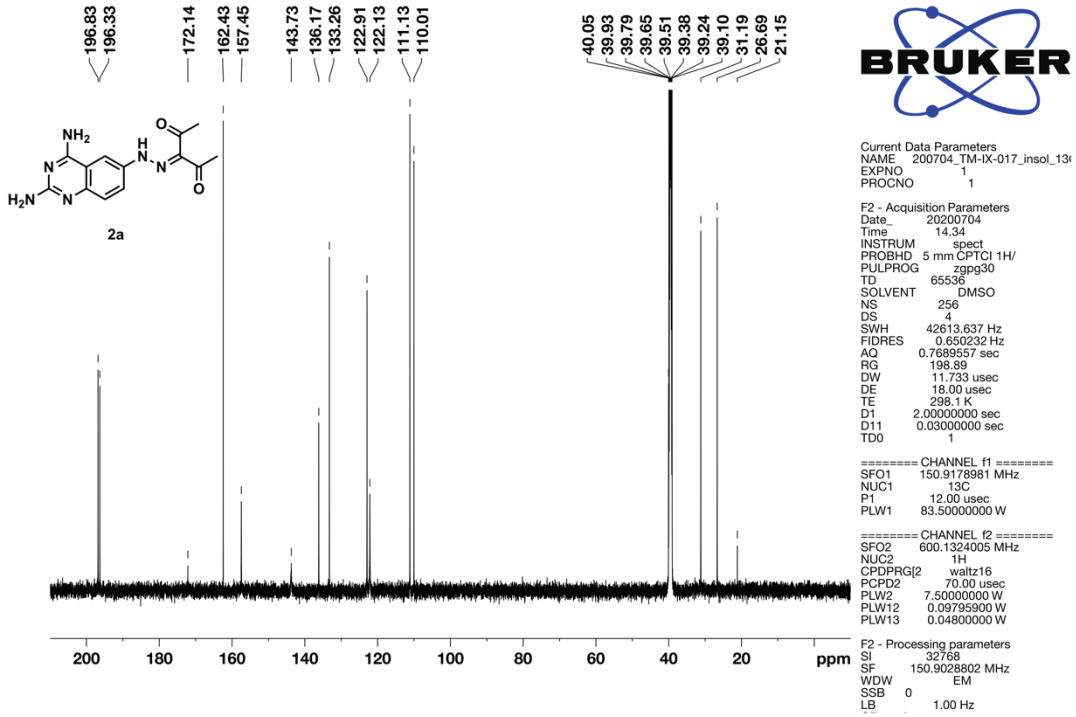

Figure S5-2. ^{13}C NMR spectrum of compound **2a** (151 MHz, DMSO-d_6).

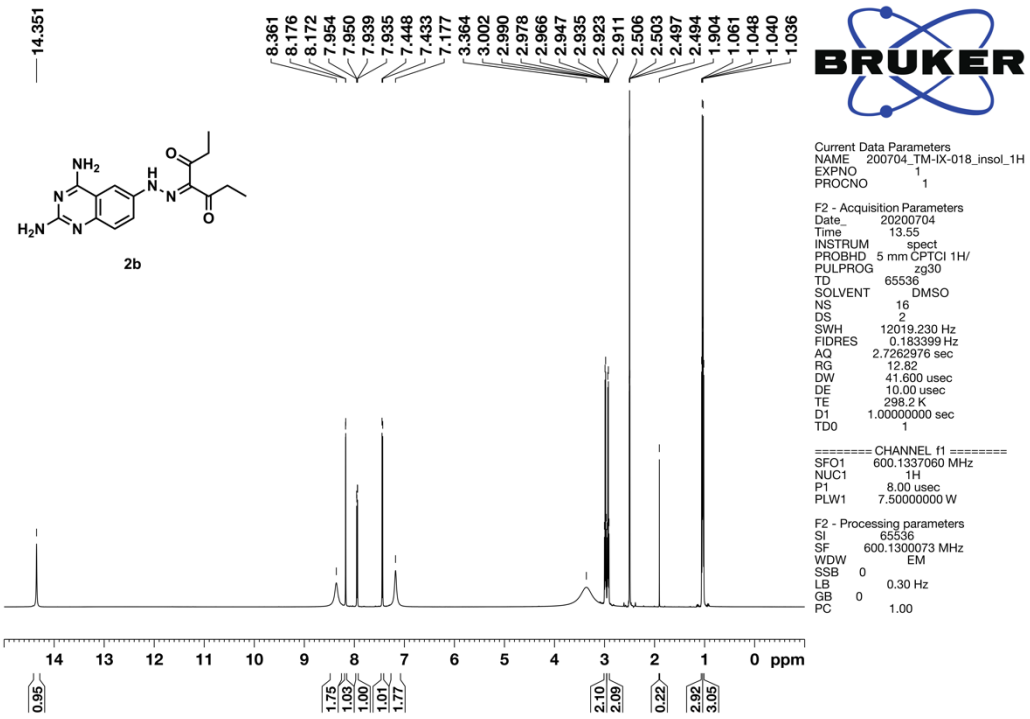

Figure S5-3. ^{1}H NMR spectrum of compound **2b** (600 MHz, DMSO-d_6).

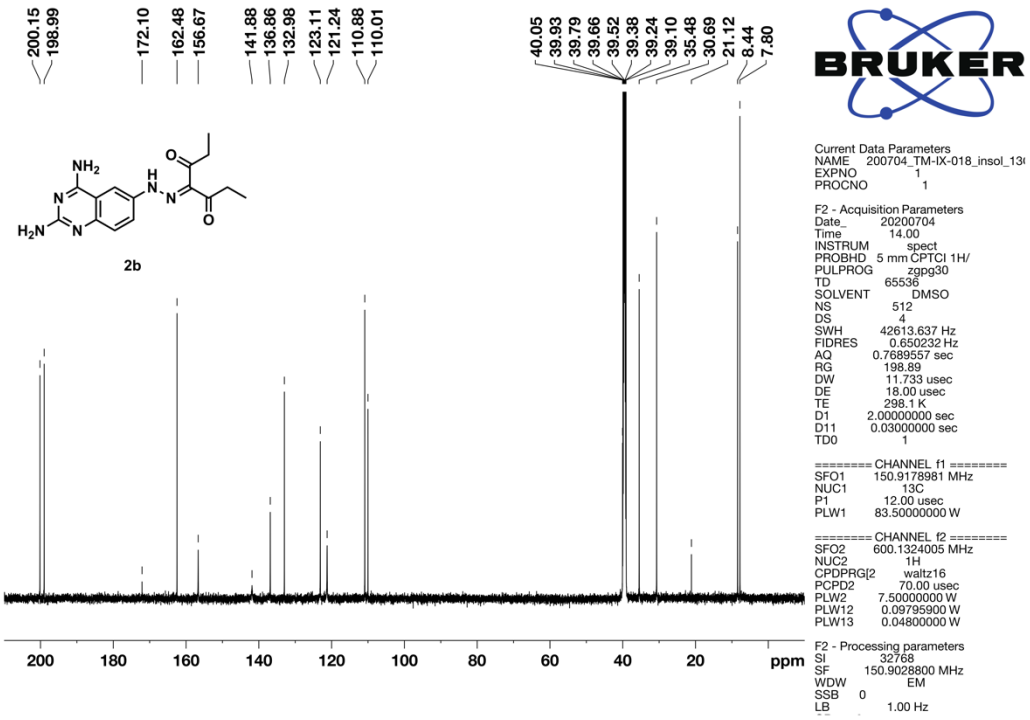

Figure S5-4. ^{13}C NMR spectrum of compound **2b** (151 MHz, DMSO-d_6).

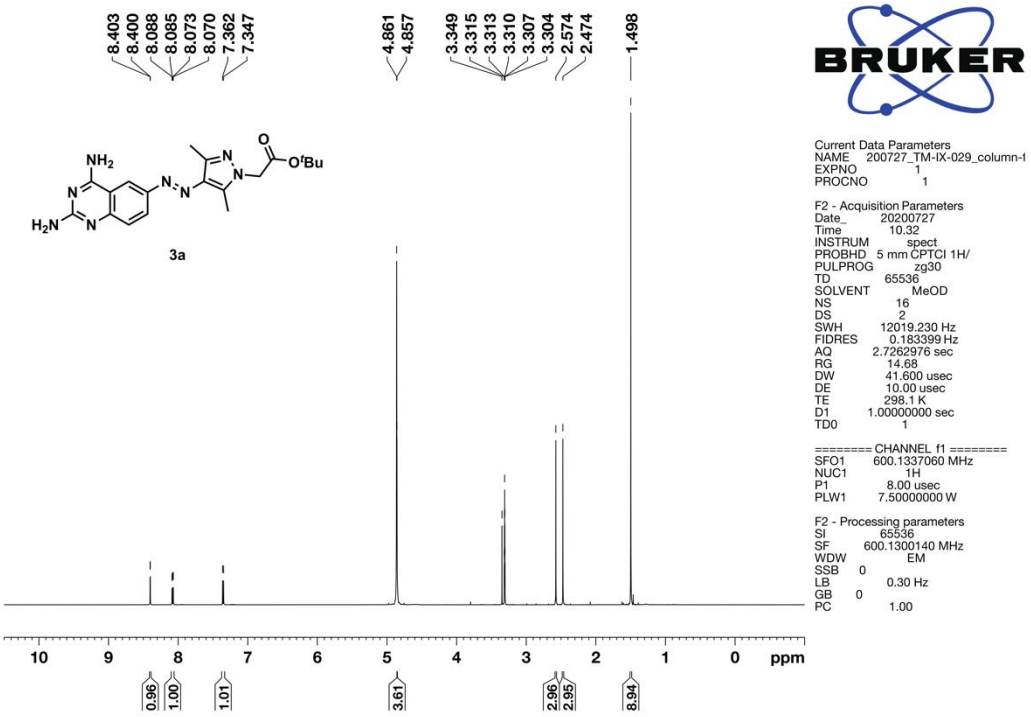

Figure S5-5. ^{1}H NMR spectrum of **3a** (600 MHz, CD_3OD).

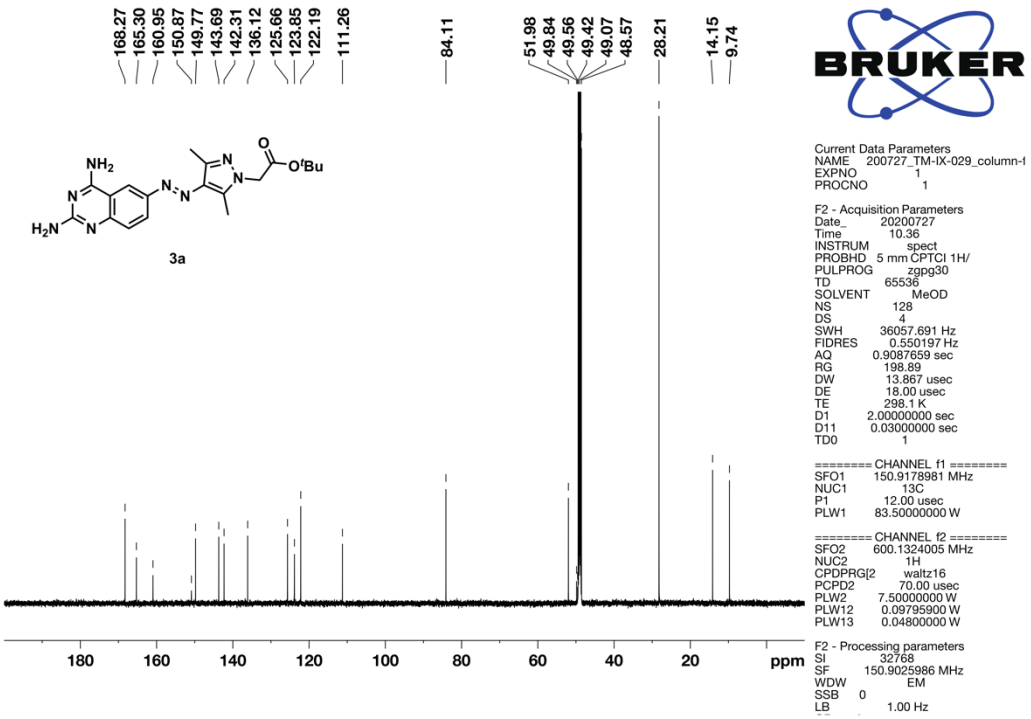

Figure S5-6. ^{13}C NMR spectrum of **3a** (151 MHz, CD_3OD).

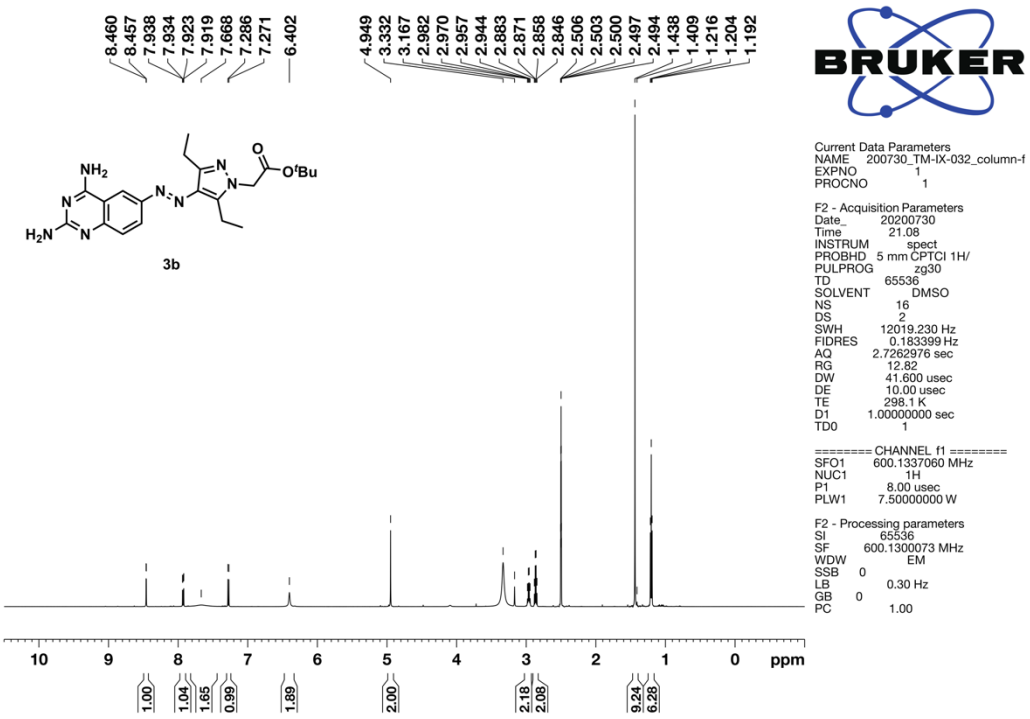

Figure S5-7. ^{1}H NMR spectrum of **3b** (600 MHz, DMSO-d_6).

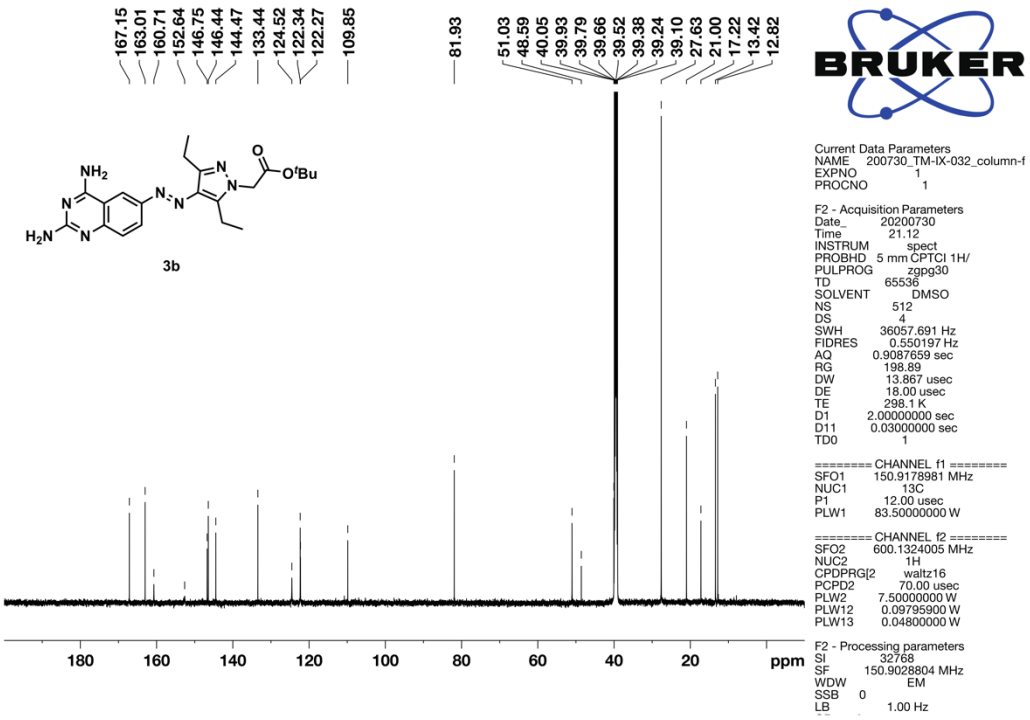

Figure S5-8. ^{13}C NMR spectrum of **3b** (151 MHz, DMSO-d_6).

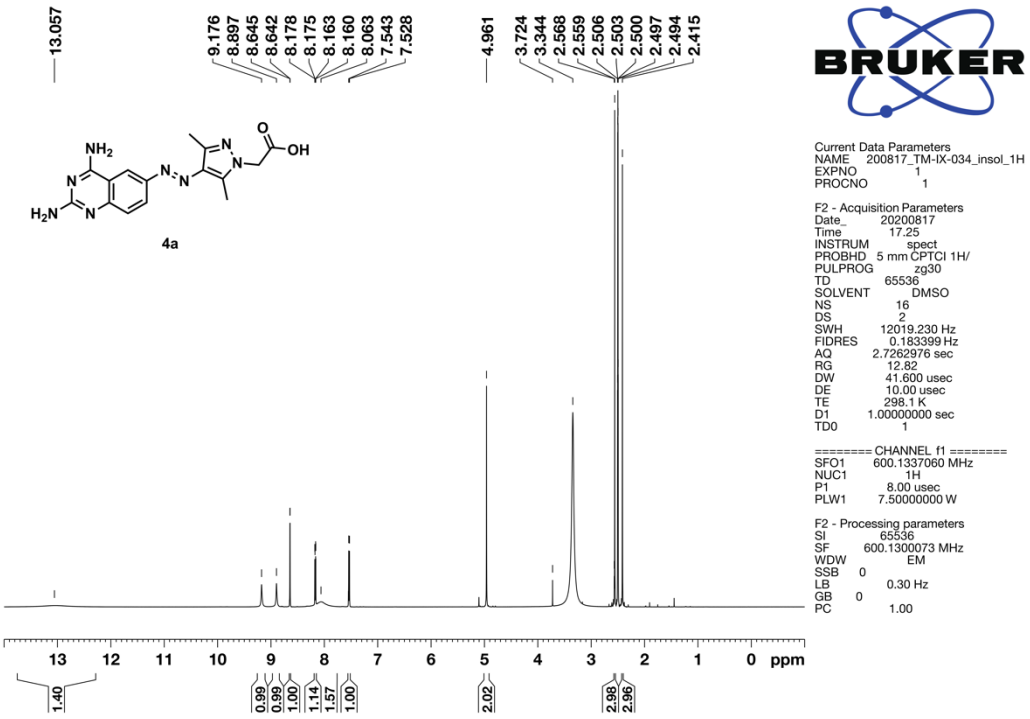

Figure S5-9. ^{1}H NMR spectrum of **4a** (600 MHz, DMSO-d_6).

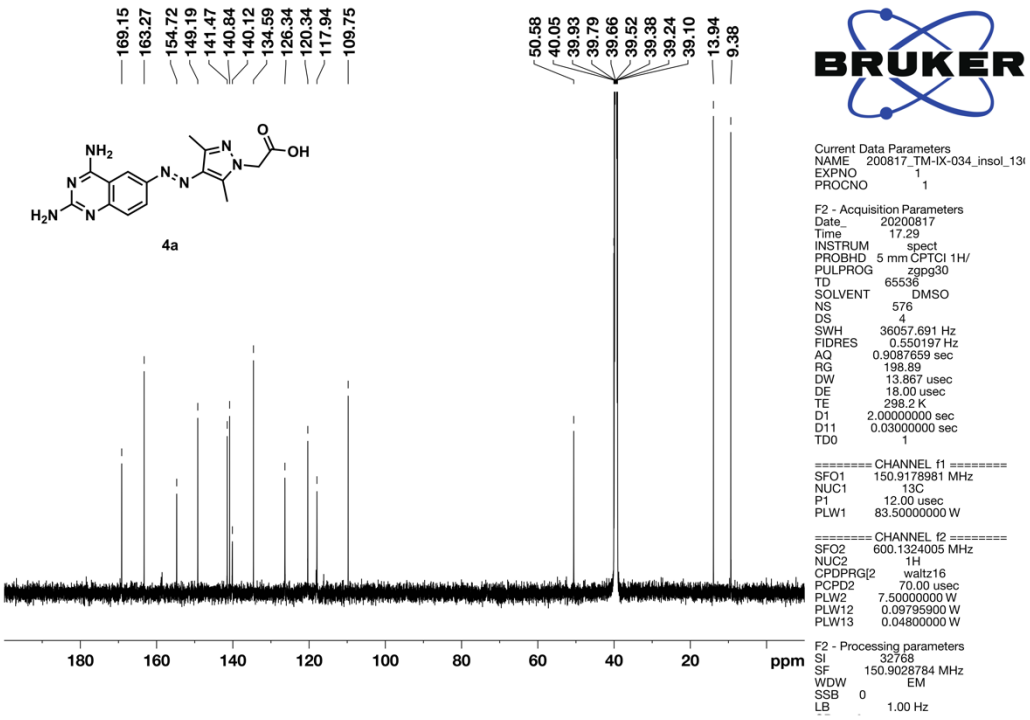

Figure S5-10. ^{13}C NMR spectrum of **4a** (151 MHz, DMSO-d_6).

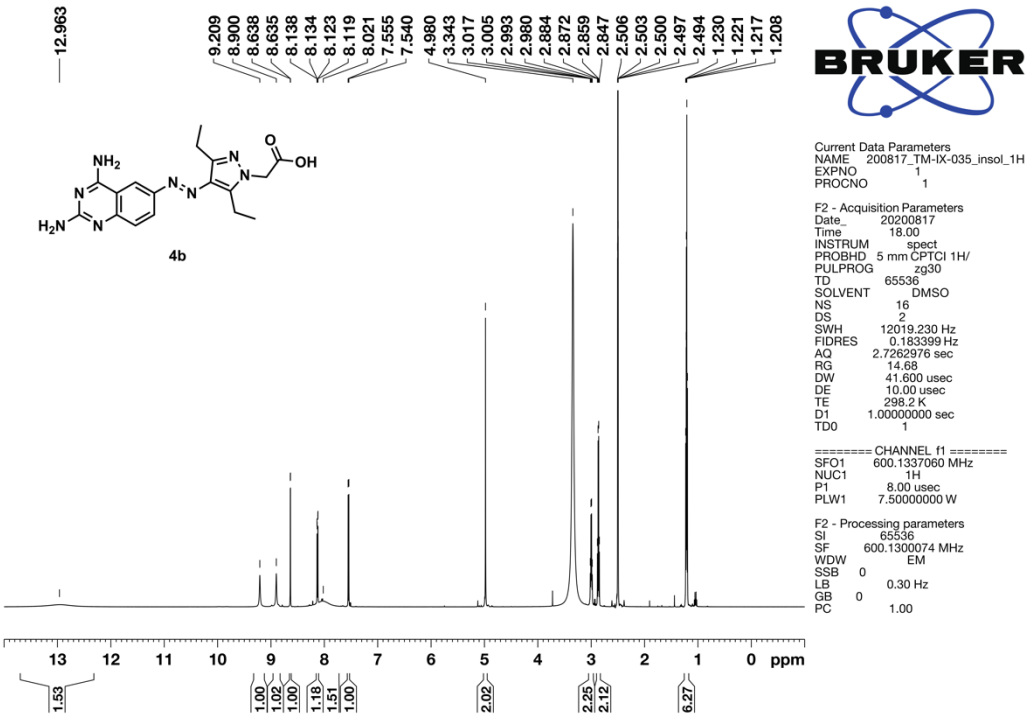

Figure S5-11. ^{1}H NMR spectrum of **4b** (600 MHz, DMSO-d_6).

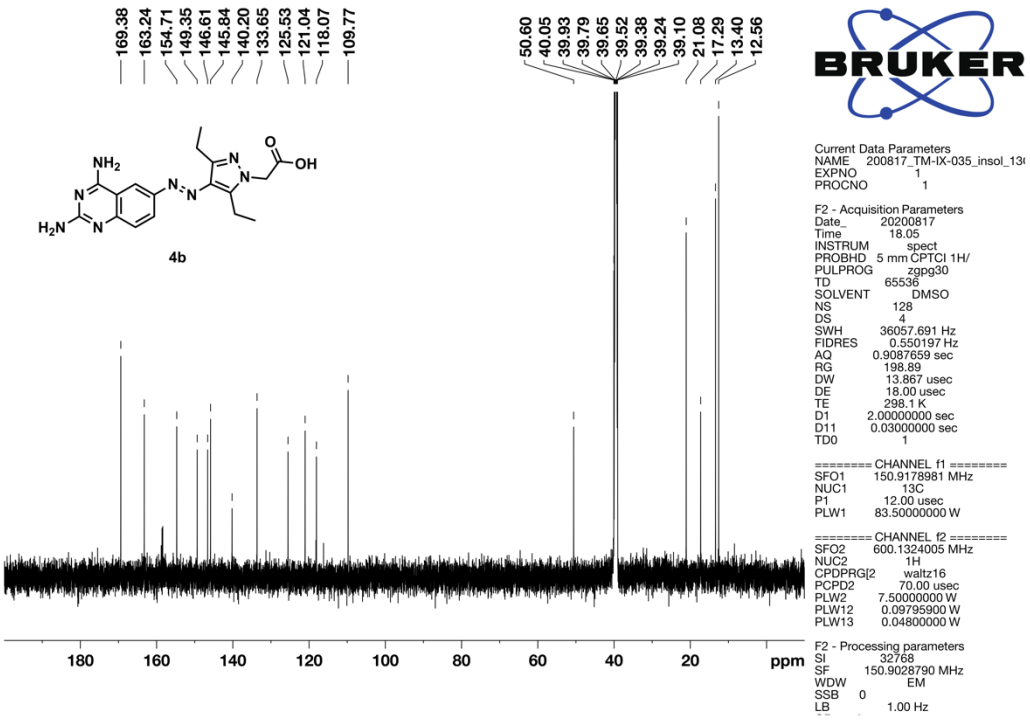

Figure S5-12. ^{13}C NMR spectrum of **4b** (151 MHz, DMSO-d_6).

5-7. References (chapter 5)

1. Mayer, G.; Heckel, A., Biologically Active Molecules with a “Light Switch”. *Angew. Chem. Int. Ed.* **2006,** *45* (30), 4900–4921.

2. Brieke, C.; Rohrbach, F.; Gottschalk, A.; Mayer, G.; Heckel, A., Light-Controlled Tools. *Angew. Chem. Int. Ed.* **2012,** *51* (34), 8446–8476.

3. Klewer, L.; Wu, Y. W., Light‐Induced Dimerization Approaches to Control Cellular Processes. *Chem. Eur. J.* **2019,** *25* (54), 12452−12463.

4. Pelliccioli, A. P.; Wirz, J., Photoremovable protecting groups: reaction mechanisms and applications. *Photochem. Photobiol. Sci.* **2002,** *1* (7), 441–458.

5. Kaplan, J. H.; Forbush, B., 3rd; Hoffman, J. F., Rapid photolytic release of adenosine 5'-triphosphate from a protected analogue: utilization by the Na:K pump of human red blood cell ghosts. *Biochemistry* **1978,** *17* (10), 1929–35.

6. Canepari, M.; Nelson, L.; Papageorgiou, G.; Corrie, J. E. T.; Ogden, D., Photochemical and pharmacological evaluation of 7-nitroindolinyl-and 4-methoxy-7-nitroindolinyl-amino acids as novel, fast caged neurotransmitters. *J. Neurosci. Methods* **2001,** *112* (1), 29–42.

7. Karginov, A. V.; Zou, Y.; Shirvanyants, D.; Kota, P.; Dokholyan, N. V.; Young, D. D.; Hahn, K. M.; Deiters, A., Light Regulation of Protein Dimerization and Kinase Activity in Living Cells Using Photocaged Rapamycin and Engineered FKBP. *J. Am. Chem. Soc.* **2011,** *133* (3), 420–423.

8. Zimmermann, M.; Cal, R.; Janett, E.; Hoffmann, V.; Bochet, C. G.; Constable, E.; Beaufils, F.; Wymann, M. P., Cell-Permeant and Photocleavable Chemical Inducer of Dimerization. *Angew. Chem. Int. Ed.* **2014,** *53* (18), 4717–4720.

9. Voß, S.; Klewer, L.; Wu, Y.-W., Chemically induced dimerization: reversible and spatiotemporal control of protein function in cells. *Curr. Opin. Chem. Biol.* **2015,** *28*, 194–201.

10. Kowada, T.; Arai, K.; Yoshimura, A.; Matsui, T.; Kikuchi, K.; Mizukami, S., Optical Manipulation of Subcellular Protein Translocation Using a Photoactivatable Covalent Labeling System. *Angew. Chem. Int. Ed.* **2021,** *60* (20), 11378–11383.

11. Ballister, E. R.; Aonbangkhen, C.; Mayo, A. M.; Lampson, M. A.; Chenoweth, D. M., Localized light-induced protein dimerization in living cells using a photocaged dimerizer. *Nat. Commun.* **2014,** *5* (1), 5475.

12. Zhang, H.; Aonbangkhen, C.; Tarasovetc, E. V.; Ballister, E. R.; Chenoweth, D. M.; Lampson, M. A., Optogenetic control of kinetochore function. *Nat. Chem. Biol.* **2017,** *13* (10), 1096–1101.

13. Aonbangkhen, C.; Zhang, H.; Wu, D. Z.; Lampson, M. A.; Chenoweth, D. M., Reversible Control of Protein Localization in Living Cells Using a Photocaged-Photocleavable Chemical Dimerizer. *J. Am. Chem. Soc.* **2018,** *140* (38), 11926–11930.

14. Chen, X.; Venkatachalapathy, M.; Dehmelt, L.; Wu, Y.-W., Multidirectional Activity Control of Cellular Processes by a Versatile Chemo-optogenetic Approach. *Angew. Chem. Int. Ed.* **2018,** *57* (37), 11993–11997.

15. Miller, L. W.; Cai, Y.; Sheetz, M. P.; Cornish, V. W., In vivo protein labeling with trimethoprim

conjugates: a flexible chemical tag. *Nat. Methods* **2005,** *2* (4), 255–257.

16. Beharry, A. A.; Woolley, G. A., Azobenzene photoswitches for biomolecules. *Chem. Soc. Rev.* **2011,** *40* (8), 4422–4437.

17. Szymański, W.; Beierle, J. M.; Kistemaker, H. A. V.; Velema, W. A.; Feringa, B. L., Reversible Photocontrol of Biological Systems by the Incorporation of Molecular Photoswitches. *Chem. Rev.* **2013,** *113* (8), 6114–6178.

18. Hüll, K.; Morstein, J.; Trauner, D., In Vivo Photopharmacology. *Chem. Rev.* **2018,** *118* (21), 10710–10747.

19. Broichhagen, J.; Frank, J. A.; Trauner, D., A Roadmap to Success in Photopharmacology. *Acc. Chem. Res.* **2015,** *48* (7), 1947–1960.

20. Borowiak, M.; Nahaboo, W.; Reynders, M.; Nekolla, K.; Jalinot, P.; Hasserodt, J.; Rehberg, M.; Delattre, M.; Zahler, S.; Vollmar, A.; Trauner, D.; Thorn-Seshold, O., Photoswitchable Inhibitors of Microtubule Dynamics Optically Control Mitosis and Cell Death. *Cell* **2015,** *162* (2), 403–411.

21. Wegener, M.; Hansen, M. J.; Driessen, A. J. M.; Szymanski, W.; Feringa, B. L., Photocontrol of Antibacterial Activity: Shifting from UV to Red Light Activation. *J. Am. Chem. Soc.* **2017,** *139* (49), 17979–17986.

22. Mashita, T.; Kowada, T.; Takahashi, H.; Matsui, T.; Mizukami, S., Light-Wavelength-Based Quantitative Control of Dihydrofolate Reductase Activity by Using a Photochromic Isostere of an Inhibitor. *ChemBioChem* **2019,** *20* (11), 1382–1386.

23. Matera, C.; Gomila, A. M. J.; Camarero, N.; Libergoli, M.; Soler, C.; Gorostiza, P., Photoswitchable Antimetabolite for Targeted Photoactivated Chemotherapy. *J. Am. Chem. Soc.* **2018,** *140* (46), 15764–15773.

24. Weston, C. E.; Richardson, R. D.; Haycock, P. R.; White, A. J. P.; Fuchter, M. J., Arylazopyrazoles: Azoheteroarene Photoswitches Offering Quantitative Isomerization and Long Thermal Half-Lives. *J. Am. Chem. Soc.* **2014,** *136* (34), 11878–11881.

25. Calbo, J.; Weston, C. E.; White, A. J. P.; Rzepa, H. S.; Contreras-García, J.; Fuchter, M. J., Tuning Azoheteroarene Photoswitch Performance through Heteroaryl Design. *J. Am. Chem. Soc.* **2017,** *139* (3), 1261–1274.

26. Stank, A.; Kokh, D. B.; Fuller, J. C.; Wade, R. C., Protein Binding Pocket Dynamics. *Acc. Chem. Res.* **2016,** *49* (5), 809–815.

27. Czekster, C. M.; Vandemeulebroucke, A.; Blanchard, J. S., Kinetic and chemical mechanism of the dihydrofolate reductase from Mycobacterium tuberculosis. *Biochemistry* **2011,** *50* (3), 367–75.

28. Nikolovska-Coleska, Z.; Wang, R.; Fang, X.; Pan, H.; Tomita, Y.; Li, P.; Roller, P. P.; Krajewski, K.; Saito, N. G.; Stuckey, J. A.; Wang, S., Development and optimization of a binding assay for the XIAP BIR3 domain using fluorescence polarization. *Anal. Biochem.* **2004,** *332* (2), 261–273.

29. Velema, W. A.; Van Der Berg, J. P.; Hansen, M. J.; Szymanski, W.; Driessen, A. J. M.; Feringa, B. L., Optical control of antibacterial activity. *Nat. Chem.* **2013,** *5* (11), 924–928.

CHAPTER 6

Conclusions and Perspective

In this doctoral dissertation, the author has achieved photo-repetitive regulation of CID system based on photochromism to overcome the limitation of optogenetic tools and photo-responsive CID systems. Focusing on photochromism, the author aimed to develop an ideal tool by using small organic molecules that can be rationally designed to adjust the wavelength of activation and inactivation, and by modifying proteins to improve the switching efficiency. Therefore, the author focused on protein labeling technology and aimed to develop a photo-reversible protein labeling technique.

In chapter 2, the author has developed a photo-switchable inhibitor—azoMTX—that can efficiently switch affinity towards eDHFR and the enzyme activity depending on light wavelength. The structure of azoMTX was rationally designed from the eDHFR–MTX complex structure, such that only the Z isomer could form a conformation almost identical to that of MTX bound to eDHFR. *E*-to-*Z* and *Z*-to-*E* photoisomerization of azoMTX was regulated by light irradiation at 394 and 560 nm, respectively. Under 394 nm light irradiation, azoMTX showed an increase of ≈ten-fold in its affinity towards eDHFR. This photochromic property also led to light-wavelength-based quantitative control and real-time reversible OFF/ON switching of the eDHFR activity.

In chapter 3, the author has succeeded in establishing a photochromic CID system. This system has allowed the reversible and repetitive regulation of a cellular process upon violet and green light. Furthermore, the recruitment of the cytosolic protein to the organelle was finely tuned by alternating the irradiation wavelength. The author also demonstrated the usability of the photochromic CID system as a potential tool that can finely manipulate intracellular protein dynamics for research on diverse cellular processes through the application to optical regulation of mitophagy initiated by PINK1 localization.

In chapters 4 and 5, the author has improved the photochromic CID system implemented in chapter 3. One room for improvement found in chapter 3 is the small dynamic range upon light illumination. This small dynamic range is attributed to the small difference in the affinity of azoMTX before and after light irradiation. Hence, the author has addressed mutation into the substrate-binding site of the eDHFR to establish a system with better *E*/*Z* selectivity. Some mutant enhanced the *E*/*Z* selectivity on the dissociation constant. These mutant eDHFRs may enhance the dynamic range of photo-regulation of intracellular protein translocation. Moreover, further screening will presumably enhance the affinity difference between the two isomers.

In chapter 5, the author has addressed the derivatization of azobenzene analog to resolve the absorption spectral overlap. Incorporation of a five-membered hetero ring into an azobenzene analog shifted absorption band for *Z*-to-*E* photoisomerization. Moreover, the derivatized ligand was also associated with and dissociated from eDHFR repetitively by alternating irradiation with two wavelengths of light.

Overall, the author has achieved photo-repetitive regulation of the CID system based on photochromism. The photo-reversible protein labeling system based on photochromism allowed a sophisticated spatiotemporal regulation of protein dynamics in live cells. In the future, the author envisions that a photochromism-based strategy for optical control may expand the toolkit for precise control of the dynamics of intracellular protein and contribute to the study of diverse cellular processes. Based on mutation in the protein and derivatization of the ligands, an ideal photo-regulation tool will be implemented.

Acknowledgments

本研究を進めるにあたり、多くの方々からご指導を賜りました。

博士前期課程と博士後期課程の 5 年間、本研究の遂行のために多大なご指導を賜りました東北大学多元物質科学研究所 細胞機能分子化学研究分野 水上 進 教授に心から感謝いたします。また、様々な実験を行うにあたり、細部にわたり丁寧なご指導を賜りました松井 敏高 准教授、小和田 俊行 助教に心から感謝いたします。

遺伝子工学実験を中心に実験の補助をしていただきました高橋 泰人 氏に深く感謝いたします。

マイトファジーの光制御に関して貴重なご助言や安定発現培養細胞を提供していただきました東京大学大学院医学系研究科 分子細胞生物学専攻 山本 林 講師に厚く感謝します。また、タンパク質—リガンド複合体の構造解析に関して多くのご指導・ご助言をいただきました東北大学多元物質科学研究所 稲葉 謙次 教授、渡部 聡 助教に厚く感謝します。

東北大学 マルチディメンジョン物質理工学リーダー養成プログラム（MD プログラム）による博士前期課程と博士後期課程の 5 年間にわたる経済支援を感謝いたします。

五年間共に研究室で過ごし、研究に励んだ水上研究室のみなさまに感謝いたします。

最後に、長い期間支えてくれた家族に心から感謝をいたします。

2022 年 3 月
東北大学 大学院理学研究科
化学専攻
細胞機能分子化学研究室
間下　貴斗